Sol-gel Synthesis of and Luminescent Properties of Pr^{3+} in Different Host Matrices

by

Mbule Pontsho Sylvia

(B.Sc Hons)

A dissertation submitted in fulfillment of the requirement for the degree

MAGISTER SCIENTIAE

in the

Faculty of Natural and agricultural Sciences

Department of Physics

at the

University of the Free State

Republic of South Africa

Study leader: Prof. O.M Ntwaeaborwa

Co-Study leader: Prof. H.C Swart

November 2009

**Dedicated to all the people
who had positive impact in my life and studies**

Acknowledgements

- First of all, I would like to thank God for giving me the courage and strength to finish this study.

- I would like to express my sincere appreciations and gratitude to my supervisor, *Prof. O.M Ntwaeaborwa* for his wisdom, patience, energy and support for the duration of the study.

- I am grateful to my co-supervisor, *Prof. H.C Swart* for his valuable knowledge and constant advice he gave throughout the study.

- I would like to extend my big thank you to *Dr. M.S Dhlamini*, a senior research scientist at Natural Centre for Nano-structured Materials of the Council for Scientific and Indulstrial Research (CSIR) for his productive discussions and advice

- I thank *Mr. P.D Nsimama* and the rest of the physics department members for their assistance and support.

- I thank *Ms G.Mhlongo*, a PhD student of the University of the Free State based at the CSIR.

- I thank the UFS physics department, Nelson Mandela Metropolitan University physics department and geology department for CL, PL and XRD measurements, respectively.

- I am extremely thankful to my grandmother, *Miriam Mbule*, my siblings *Alina, Lettie and Pascalina* and the rest of the family for their understanding and support in every decision I made regarding my studies. I owe my greatest thank you to *Mamaphesa and Pule Esemang* for the role they played and moral support.

- I am grateful for the financial support from the *South African National Research Foundation and the University of the Free State.*

Abstract

Luminescent $ZrO_2:Pr^{3+}$, $SiO_2:Pr^{3+}$, $ZnO:Pr^{3+}$ and $ZnS:Pr^{3+}$ nanophosphors were synthesized by a sol-gel method, dried, ground and annealed in air at 600^oC ($SiO_2:Pr^{3+}$, $ZrO_2:Pr^{3+}$, $ZnO:Pr^{3+}$ and $ZnS:Pr^{3+}$) or 280^oC ($ZrO_2:Pr^{3+}$). The chemical composition of the powder phosphors was analyzed by energy dispersive x-ray spectrometer (EDS). The structure and particle sizes were determined with x-ray diffraction (XRD) and particle morphology was analyzed using scanning electron microscopy (SEM) and transmission electron microscopy (TEM). $SiO_2:Pr^{3+}$ was amorphous even after annealing at 600^oC. $ZrO_2:Pr^{3+}$ annealed at 280^oC showed an amorphous structure but the material crystallized when the annealing temperature was increased to 600^oC. The particle sizes estimated from the XRD peaks were $\sim 2\pm 0.2$ nm (dried ZnS and ZnO) and $\sim 8\pm 0.1$ nm ($ZrO_2:Pr^{3+}$ annealed at 600^oC). Particle sizes increased to ~ 17-20 ± 0.2 nm in diameter for annealed $ZnS:Pr^{3+}$ and $ZnO:Pr^{3+}$.

The UV-Vis spectrophotometer was used to determine the absorption properties of the nanophosphors and their band absorption showed a blue shift compared to their bulk counterparts. Powder phosphors were also irradiated with 325 nm (He-Cd) laser to study photoluminescence (PL) properties. PL spectra were obtained for both undoped and Pr^{3+} - doped nanophosphors. A broad emission band was observed at 498 nm with a shoulder at 416 nm from $SiO_2:Pr^{3+}$ annealed at 600^oC. $ZrO_2:Pr^{3+}$ annealed at 280^oC showed two emission bands in the visible range at 459 nm and 554 nm. A broad green emission band at 567 nm and a shoulder at 607 nm were observed for dried $ZnO:Pr^{3+}$ nanophosphor and the shoulder at 607 nm was enhanced significantly when the Pr^{3+} concentration was increased. Annealed $ZnO:Pr^{3+}$ (280^oC) nanophosphor showed a green emission band centered around 533 nm and a shoulder at 624 nm. Dried $ZnS:Pr^{3+}$ nanophosphor showed a blue emission centered at 445 nm and the PL intensity increased with an increase of Pr^{3+} ions concentration. All these emissions were coming from the host matrices and not from the Pr^{3+} ion when the powders were excited by 325 nm (~ 3 eV) photons.

SiO_2 and $SiO_2:Pr^{3+}$ powder phosphors were subjected to prolonged 2 keV electron beam irradiation in an ultra high vacuum (UHV) chamber at a base pressure of $1x10^{-9}$ torr. The surface reactions and degradation of cathodoluminescence intensity were monitored using

Auger electron spectroscopy (AES) and cathodoluminescence (CL) spectroscopy respectively. CL emission of SiO_2 showed a maximum emission peak at 451 nm and a shoulder at 478 nm and $SiO_2:Pr^{3+}$ showed a multiple peak emissions located at 510 nm, 614 nm, 730 nm, 780 nm and 970 nm which are attributed to the transitions in the Pr^{3+} ions. The $SiO_2:Pr^{3+}$ CL intensity decreased with time as a result of continuous exposure to 2 keV electrons. The Auger peak-to-peak height as a function of energy spectrum showed that there were changes on the surface chemistry of the powders as a result of prolonged irradiation by 2 keV electrons. It is most likely that non-luminescent layers were formed on the surface and they contributed to the CL intensity degradation. A high concentration of volatile gas species, which might have contributed to the CL degradation, was detected with a residual gas analyzer (RGA). Cathodoluminescence was not measured for $ZnO:Pr^{3+}$, $ZnS:Pr^{3+}$ and $ZrO_2:Pr^{3+}$ due to charging of the powder phosphors and $ZrO_2:Pr^{3+}$ did not emit light under high energy electron exposure (2 keV).

Key Words

Sol-gel, Praseodymium, Luminescence, Photoluminescence, Cathodoluminescence Degradation

Acronyms

- PL- Photoluminescence
- CL- Cathodoluminescence
- APPHs- Auger peak-to-peak heights
- XRD- X-ray diffraction
- TEM- Transmission electron microscopy
- SEM- Scanning electron microscopy
- EDS- energy x-ray dispersive spectroscopy
- AES- Auger electron spectroscopy
- TEOS- Tetraethylorthosilicate
- EtOH- Ethanol

Table of Contents

Chapter1: Introduction

Chapter 2: Literature Review

Chapter 3: Theory of Research Techniques

Chapter 4: Synthesis of Powder Phosphors

Chapter 5: Properties of praseodymium (Pr^{3+}) doped Zirconium oxide (ZrO_2)

Chapter 6: Properties of praseodymium (Pr^{3+}) doped silicon dioxide (SiO_2)

Chapter 7: Cathodoluminescence degradation of SiO$_2$:Pr^{3+} powder phosphor

Chapter 8: Properties of praseodymium (Pr^{3+}) doped Zinc oxide (ZnO)

Chapter 9: Properties of praseodymium (Pr^{3+}) doped Zinc sulphide (ZnS)

Chapter 10: Summary and Conclusion

Chapter 1

Introduction

1.1 Background

A phosphor is a material that gives off light under some type of external stimulation, which can be an electron beam, light of a different wavelength, a voltage or electric field [1]. Phosphors are widely available in the form of micron (bulk phosphors) to nanometer (nanophosphors) powders. They can also be grown into thin luminescent films for a particular application in light emitting devices. Because of the realization that the optical properties of nanoparticle phosphors or nanophosphors can differ drastically from those of bulk phosphors there has been increased research interest in the synthesis and characterization of nanophosphors in the past two decades. In particular, researchers are driven by the prospect that better understanding of the basic physics of nanoparticles will enable their application in light emitting devices of all types. Examples include displays (e.g., screens on televisions, computers, and cell phones), light emitting diodes that have been proposed to replace conventional incandescent bulbs, and light sources used in telecommunications in optical fiber.

The size range that hold so much interest in nanomaterials is typically from 100 nm down to the atomic level (approximately 0.2 nm), because it is in this range that materials can have different or enhanced properties compared with the same materials at a larger size (bulk) [2]. The two main reasons for this change in behavior are an increased relative surface area, and dominance of quantum confinement effects of charge carriers (electrons and holes) in the restricted volume of nanoparticles [2,3]. An increase in surface area (per unit mass) result in a corresponding increase in chemical reactivity, making some nanomaterials useful as catalysts

to improve the efficiency of cells and batteries. It is reported that in order to meet the technological demands in the areas such as electronics, catalysis and structural components, the size of the materials should be reduced to the nanometer scale [3]. Phosphors can be classified as sulfides and oxides. Examples of sulfide phosphors are zinc sulfide co-doped with copper and aluminum (ZnS:Cu,Al), cadmium sulfide (CdS) doped with rare-earth elements such as europium (Eu^{3+}), terbium (Tb^{3+}), cerium (Ce^{3+}) or praseodymium (Pr^{3+}). Examples of oxide phosphors are zinc oxide (ZnO), yttrium oxide (Y_2O_3) or silicon dioxide (SiO_2) doped with rare-earth elements. In the study of sulfide phosphors for applications in high current densities low voltage field emission displays (FEDs) by various researchers [4,5,6] it has been shown that their cathodoluminescent intensity degrade drastically by developing non luminescent oxide (e.g. ZnO) surface layer and releasing volatile compounds such as SO_2 and H_2S which are detrimental to emitter tips of FED's. That is, sulfide phosphors are chemically unstable under high current densities required for FED technology. On the other hand, oxide phosphors have been reported to be more chemically and thermodynamically stable under high current densities and high temperatures. Unlike sulphide phosphors, oxide phosphors do not release volatile compounds during prolonged electron beam exposure. Oxide phosphors have therefore been considered to replace sulphide phosphors in different types of light emitting devices including low voltage FEDs [7]. Examples of oxide phosphors which have been extensively studied as possible replacements are Y_2O_3:Eu^{3+}, SiO_2: RE (RE = Eu^{3+}, Ce^{3+}, Tb^{3+}) [7] and ZnO. ZnO has attracted great attention due to its promising applications in ultraviolet light-emitting diodes, field emission, gas sensors, solar cells and laser diodes [8,9,10], as well as its stability under ultraviolet light and relative high electric conductivity when compared with the conventional sulphide phosphors [8].

There has been constant interest in trying to develop luminescent materials with higher radiative efficiency. This has led to increased research activities on the study of the synthesis and characterization of rare-earth doped materials where the host materials used have a high energy band gap, low phonon energy and chemical stability over photon and electron radiations [11]. In recent years, considerable research has been done on the synthesis and characterization of large bandgap oxide materials such as Y_2O_3 and SiO_2 doped with rare-earth elements using different chemical methods such as sol-gel precipitation and combustion. Sol gel has been found to have advantages over other methods as it allows the preparation of quality materials with high purity and homogeneity, as well as control of

particle size [12]. Controlling the size, shape and structure of materials at nanoscale is technologically important because of strong correlation between the parameters and optical, electrical, magnetic and catalytic properties [3].

This study is therefore devoted to the synthesis of large bandgap oxide inorganic materials doped with praseodymium ions (Pr^{3+}). Among all lanthanide (III) ions interest is especially focused on Pr^{3+} ions, which have very rich emission spectra extending from ultraviolet to near-infrared spectral range. Besides the intra-configuration f-f emission, praseodymium ions can exhibit an intense broad band emission due to the parity allowed electric dipole $4f^{N-1}$ $5d^1 \rightarrow 4f^N$ transitions [13]. Furthermore, rare-earth doped materials that can be used in the electrical and optical devices, particularly Pr^{3+} doped ZnO shows unique property because of its changeable characteristics, where the Pr ions could be located in the boundaries of ZnO grains [14]. Pr^{3+} doped materials are used in a large number of different applications, like in thermoluminescent (TL) lighting and FEDs. A promising phosphor for the latter application is $CaTiO_3$: Pr^{3+} [15]. Zhang *et al* reported a novel white long-lasting phosphor $SrSiO_4$:Pr^{3+}, which phosphorescence indirectly comes from the luminescence of Pr^{3+} ions [16]. They found that the emission spectrum of this phosphor has three groups of emissions located at 390 nm, 535 nm and 604 nm, which correspond to the transitions of 4f-5d (bluish purple), $^3P_0$ -$^3H_5$ (green), and $^1D_2$ -$^3H_4$ (red) respectively. Further investigations of Pr-doped SiO_2 and ZrO_2, ZnO and ZnS prepared by sol-gel method are reported in this study. The effects of concentration of Pr^{3+} in these hosts were investigated.

1.2 Problem Statement

Recently there has been some emphasis on the optical properties of glassy (amorphous) semiconductors doped with small amounts of rare-earth ions [17]. The development of new phosphors for vacuum ultraviolet (VUV) excitation is an important new challenge in the field of luminescence materials research. The phosphors excited in the VUV can be used in a new generation of lamps or in gas plasma discharge devices for flat color display panels. Praseodymium and cerium compounds seem to be promising for these purposes [18]. The parity allowed electric dipole transitions in trivalent Pr^{3+} ions make it even more attractive activating center in different crystalline hosts which exhibit intense broad emission useful for fast scintillators and ultraviolet tunable laser devices. This wide emission due to strong coupling between the 5d electron of the Pr^{3+} ion and lattice phonons of the host is observed if

the lowest 5d state is located below the $4f^2$ ($^1S_0$) state of the Pr^{3+} ion. If the 5d states are located at higher energies than the $^1S_0$ state, the photon cascade emission can be observed after excitation in the 5d bands with quantum yields of more than 100% [18]. This phenomenon could be an interesting subject of investigation of luminescence of Pr^{3+} ions in different host lattices.

The sol-gel method has been reported to have more advantages over other wet chemistry and conventional glass processing methods because it has the potential to produce materials with high purity and homogeneity at low temperatures. It extends the traditional glass melting processes by allowing incorporation of semiconductor nanocrystals and rare-earth activators at low temperatures and predetermined concentrations in different hosts in such a way that the size and shape of the particles can be controlled during the growth and nucleation processes [7]. Sol-gel was therefore chosen as the preferred method for the synthesis of Pr^{3+} phosphors investigated in this study.

1.3 Study Objectives

- To synthesize Pr-doped SiO_2, ZrO_2, ZnO and ZnS powder phosphors using the sol-gel method.
- To study the structure and luminescent (photoluminescence and cathodoluminescence) properties of Pr^{3+}-doped nanophosphors
- To investigate annealing temperature effects on the structure of the nanophosphors

1.4 Dissertation Layout

Chapter 2 presents the literature review on powder phosphors, classification, fundamentals of phosphors and luminescence processes.

Chapter 3 deals with the theory of the research techniques used in this study; this includes a brief description on how each of these techniques works.

Chapter 4 gives a brief discussion of the sol-gel method and synthesis of Pr-doped SiO_2, ZrO_2, ZnO and ZnS powder phosphors.

Chapter 5 deals with the luminescence properties of $ZrO_2:Pr^{3+}$ powder phosphor.

Chapter 6 deals with the luminescence properties of $SiO_2:Pr^{3+}$ powder phosphor.

Chapter 7 provides the cathodoluminescence degradation of $SiO_2:Pr^{3+}$ powder phosphor.

Chapter 8, luminescence properties of $ZnO:Pr^{3+}$ powder phosphor are presented

Chapter 9 deals with luminescence properties of $ZnS:Pr^{3+}$ powder phosphor.

Chapter 10 - summary of the results, conclusion and suggestion for possible future studies are discussed in this chapter.

References

[1] Mark R. Davidson, Paul Holloway,"phosphor technology", in accessscience@McGraw-Hill, http://www.accessscience.com, DOI 10.1036/1097-8542.YB041080 [6 October 2009]

[2] Nanoscience and technologies, available from www.nanotec.org.uk/report/chapter2.pdf [6 October 2009]

[3] M.S Dhlamini, PhD dissertation, University of the Free State, South Africa, 2008

[4] H.C Swart, A.P Greeff, P.H Holloway and G.L.P Berning, *Applied Surface Science* **140** (1999) 63-69

[5] K.T Hillie and H.C Swart, *Applied Surface Science* **193** (2002) 63-69

[6] S.H Chen, A.P Greeff and H.C Swart, J*ournal of Luminescence* **113** (2005) 191-198

[7] O.M. Ntwaeaborwa, PhD dissertation, University of the Free State, South Africa, 2006.

[8] Ying Yi Li, Yong Xiu Li, Yan Li Wu and Wei Li Sun, *Journal of Luminescence* **126** (2007) **177-181**

[9] Fei Li, Yin Jiang, Liang Hu, Luoyuan Liu, Zhen Li and Xintang Huang, *Journal of Alloys and Compounds* **474** (2009) 531-535

[10] Zhigang Jia, Linhai Yue, Yifan Zheng and Zhude Xu, M*aterials Chemistry and Physics* **107** (2008) 137-141

[11] F.Ramos-Brito, H Murrieta S, J Hernandez A, E Camarillo, M Garcia-Hipolito, R Martinez, O alvarez-Fragoso and C Falcony, Journal of *Physics D:Applied Physics* **39** (2006) 2079-2083

[12] D.H Aguilar, L.C Torres-Gonzalez and L.M Torres-Martinez, *Journal of Solid State Chemistry* **158**(2000) 349-357

[13] M. Karbowiak, J. Legendziewicz, J. Cybinska and G Meyer, *Journal of Alloys and Compounds* **451**(2008) 104-110

[14] Y. Inoue, M Okamoto, T. Kawahara and J. morimoto, *Journal of Alloys and Compounds* **408** (2006) 1234-1237

[15] P. Boutinaud, E. Pinel, M. Dubois, A.P. Vink and R. Mahiou, *Journal of Luminescence* **69-80** (2005)111

[16] Li Zhang, Xinmu Zhou, Huihui Zeng, huiqin Chen and Xueping Dong, *Materials Letters* **62** (2008) 2539-2541

[17] Y.K. Sharma, S.C Marthur, D.C. Dube and S.P Tandon, *Journal of Materials Science Letters* **14** (1995) 71-73

[18] J. Cybinska, J. Legendziewiez, G. Boulon, A. Bensalah and G. Meyer, *Optical Materials,* **28** (2006) 41-52

Chapter 2

Literature Review

2.1 Praseodymium: A rare-earth metal

Praseodymium is a soft malleable, silvery yellow metal. It is the member of the lanthanide group of the periodic table of elements. It reacts rapidly with water and slowly with oxygen when exposed to air to form a green oxide that does not protect it from further oxidation. It is more resistant to corrosion in air than other rare-earth metals and can be stored in a sealed plastic bag [1].

2.1.1 Applications

Praseodymium compounds have different uses. The oxide is used in carbon electrodes for arc lighting and it is known for its ability to give a glass a nice yellow color. This glass filters out the infrared radiation, so it is used in goggles which protect the eyes of the welders. The salts are used to color enamels and glass. Praseodymium can be used as the alloying agent with magnesium to create high strength metals that are used in aircraft engines. The use of praseodymium is still growing, due to the fact that it is suited to produce catalysts and to polish glass [1].

2.1.2 Praseodymium in the environment

It is one of the most abundant of the rare-earth metals, it is four times more abundant than tin (Sn). It is usually found only in two different kinds of ores. The major commercial ores in which praseodymium is found are the monazite and bastnasite. The main mining areas are China, USA, Brazil, India, Sri Lanka and Australia. Current production of praseodymium is about 2500 tonnes per year [1].

2.1.3 Environmental effects of praseodymium

It is dumped in the environment in many different places, mainly by petrol-producing industries. It can also enter the environment when the household equipment is thrown away. Praseodymium will gradually accumulate in soils and water soils and this will eventually lead to increase in concentrations in humans, animals and soil particles. In aquatic animals praseodymium causes damage to the cell membranes, which has several negative influences on reproduction and on the functions of the nervous system [1].

2.1.4 Health effects of Praseodymium

Like all rare-earth metals praseodymium is of low to moderate toxicity. Soluble praseodymium salts are mildly toxic if ingested, with insoluble salts are non-toxic, but can cause skin and eye irritation. Praseodymium is mostly dangerous in the working environment, due to the fact that vapors and gases can be inhaled with air. This can cause lung embolisms, especially during long exposure. It can be a threat to the liver when it accumulates in the human body [1].

2.2 Luminescent spectroscopy of Pr^{3+} and other rare-earth ions

Rare-earth ions are categorized by a group of 15 elements known as the lanthanides and are most stable in their triply ionized form [2,3]. The trivalent ($^{3+}$) ionization of these elements preferentially remove $6s$ and $5d$ electrons, leaving an electronic structure identical to xenon plus a certain number (1-14) of 4f electrons i.e. $1s^2, 2s^2, 2p^6, 3s^2, 3p^6, 3d^{10}, 4s^2, 4p^6, 4d^{10}, 4f^N, 5s^2, 5p^6$ and $6s^0$ where N = 1,……..14. The remaining $4f$ electrons are therefore shielded partially by the outer $5s$ and $5p$ shells [4]. This shielding results in $4f \rightarrow 4f$ optical transitions which are relatively sharp and for the most part are insensitive to the host material, unlike many of the optical transitions which take place in transition metals such as Cr^{3+} [2,3,5]. The Lanthanide elements in their triply ionized form are referred to as rare-earth ions. The rare-earth of particular interest is highlighted in the table 2.1

Table 2.1: Lanthanide series of the elements [2].

57	58	59	60	61	62	63	64	65	66	67	68	69	70	71
La	Ce	Pr	Nd	Pm	Sm	Eu	Gd	Tb	Dy	Ho	Er	Tm	Yb	Lu

The Pr^{3+} ion has the [Xe] $4f^2$ configuration. The energy level scheme up to about 25 000 cm^{-1} shown in Figure 2.1, consists of a large number of energy levels. Upon excitation with UV or visible light the emission spectrum can either be dominated by emission from the $^3P_0$ level (green-blue emission) or from the $^1D_2$ level (red emission) [6]. Pr^{3+} also has a rich spectrum transitions in the IR wavelength from $^1G_4$. Shaw *et al* [7], reported the strong mid-IR emission of Pr^{3+}-doped heavy metal selenide glasses and the spectral properties make these glass a strong candidate for lasers, amplifiers and high brightness sources in the mid-IR.
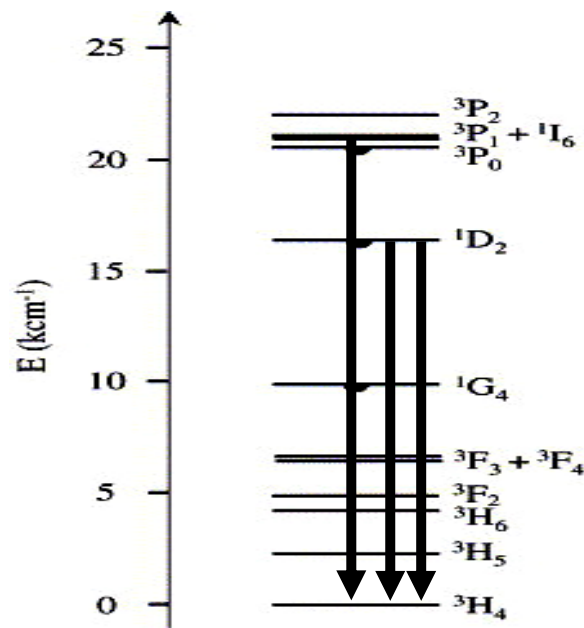

Figure 2.1: Energy level scheme of the Pr^{3+} ion up to about 25, 000 cm^{-1} [6].

2.3 Fundamentals of Phosphors: Energy Levels

Phosphors typically are either wide-band gap (energy difference between the valence band and conduction band) semiconductor or insulating host materials containing a dopant or an impurity. They are usually in the form of powders, but in some cases they may be in the form of thin films [15]. In the bulk of a crystalline material, translational symmetry leads to the formation of electronic energy bands. Defects and impurities break the periodicity of the lattice and perturb the band structure locally [9,16]. The perturbation usually can be characterized by a discrete energy level that lies within the bandgap. Depending on the defect or impurity, the state acts as a donor or acceptor of excess electrons in the crystal. Electrons and holes are attracted to the excess or deficiency of local charge due to the impurity nucleus or defect, and coulomb binding occurs. The situation can be modeled as a hydrogenic system where the binding energy is reduced by the dielectric constant of the material [9]. Because electrons and holes have different effective masses, donors and acceptors have different binding energies.

When the temperature is sufficiently low, carriers will be trapped at these states. If these carriers recombine radiatively, the energy of the emitted light can be analyzed to determine the energy of the defect or impurity level. Shallow levels, which lie near the conduction or valence band edge, are most likely to participate in radiative recombination, but the sample temperature must be small enough to discourage thermal activation of carriers out of the traps [9]. Deep levels tend to facilitate nonradiative recombination by providing a stop-over for the electrons making their way between the conduction and valence bands by emitting phonons. Several intrinsic and impurity transitions are illustrated in Figure 2.2.
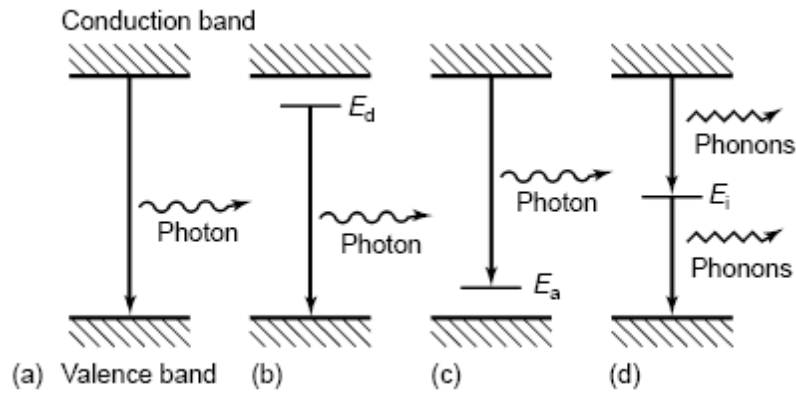
Figure 2.2: (a-c) Radiative recombination paths: (a) Band-to-band (b) Donor to valence band (c) conduction band to acceptor and (d) Nonradiative recombination via an intermediate state [9].

2.4 Luminescence

Luminescence is the phenomenon of emission of light from various phosphor materials. It can be divided into two kinds, namely phosphorescence and fluorescence. Phosphorescence is a slow process in which emission continues for a few seconds, minutes or even hours after removing the excitation, whereas fluorescence is fast process in which emission stops abruptly after turning off the excitation [8]. Phosphors can be broadly classified into groups based on the method of excitation and their applications.

2.4.1 Cathodoluminescence

Cathodoluminescence (CL) is defined as luminescence stimulated by a collision between an energetic beam of electrons (primary electrons) and a solid material (phosphor) resulting in an emission of visible light [10,11]. The most common example is the CL process taking place on the screen of a television set, cathode-ray tube (CRT) or field emission display (FED). Two types of collisions are possible, namely elastic and inelastic collisions. An elastic collision occurs between primary electrons and atoms of the target material. This collision type produces back-scattered electrons, which suffer virtually no loss of energy. Inelastic collisions involve electron-electron and electron-plasmon interactions. In these cases, a single primary electron undergoes a rapid inelastic collision within a phosphor. Each collision can produce secondary electrons. The secondary electrons whose energies exceed the work function of the phosphor will escape into vacuum; otherwise they will be trapped within the lattice. Because of the large

consumer base, a great deal of research and optimization has been done for cathode ray tube (CRT) phosphors and their technology is considered mature [9].

2.4.2 Photoluminescence

Photoluminescence (PL) refers to the luminescence stimulated by the excitation of solid material (phosphor) by light of another wavelength, typically ultraviolet (UV), visible or infrared light. PL analysis is nondestructive and the technique requires very little sample manipulation or environmental control. The fundamental limitation of PL analysis is its reliance on radiative events. The materials with poor radiative efficiencies, such as low quality indirect semiconductors, are difficult to study via ordinary PL. Similarly, the identification of impurity and defect states depends on their optical activity. Although PL is a very sensitive probe of radiative levels, one must rely on the secondary evidence to study states that couple weakly with light [9]. The most prevalent use of photoluminescent phosphors is in fluorescent lamps and it is divided into two major types, namely intrinsic photoluminescence and extrinsic photoluminescence [12]. Intrinsic photoluminescence is displayed by materials, which contain no impurity atoms. Extrinsic photoluminescence results from intentionally incorporated impurities, in most cases metallic impurities or intrinsic defects [12].

2.4.2.1. Intrinsic Photoluminescence

There are three kinds of intrinsic photoluminescence, namely band-to-band, excitons and cross-luminescence. Band-to-band results from the recombination of an electron in the conduction band with a hole in the valence band and can only be observed in a very pure crystals at relatively high temperatures [13]. An exciton is a composite particle resulting from the coupling of an electron and a hole; it then travels in a crystal and produces luminescence by releasing its energy at luminescent centers. Cross-luminescence is produced by the recombination of an electron in the valence band with a hole in the outermost core band. It can only take place when

the energy difference between the top of the valence band and that of the outermost core band is smaller than the band-gap energy, otherwise, an Auger process occurs [13].

2.4.2.2. Extrinsic Photoluminescence

Most of the observed types of luminescence that have practical applications belong to this category. Extrinsic luminescence is classified into two types, namely localized and delocalized luminescence. In a delocalized luminescence the excited electrons and holes of the host lattice participate in the luminescence process, while in a case of the localized luminescence the excitation and emission processes are confined in a localized luminescence center, the host lattice does not contribute to luminescence process [13].

2.5 Sensitized Photoluminescence

By definition, sensitized photoluminescence refers to a process whereby an impurity species (activator or acceptor) having no appreciable light absorption ability in a given spectral domain, is made to emit radiation upon excitation as a result of absorption by and transfer from another impurity species (sensitizer, or donor)[14]. This is shown in Figure 2.3.
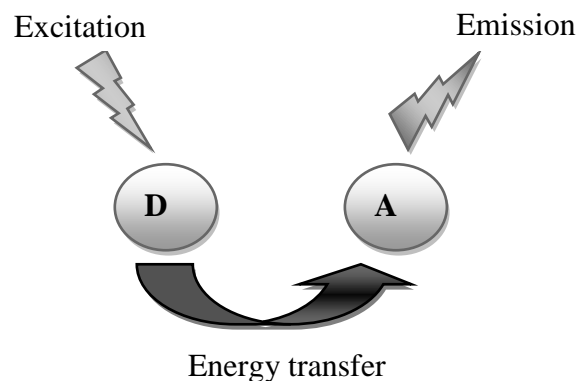
Figure 2.3: Principle of sensitized photoluminescence, the activator (**A**) is made to emit light after being excited via an energy transfer from the photoexcited donor (**D**)[14].

2.5.1. Sensitization mechanism

The general steps of a sensitization mechanism are usually described as shown in Figure 2.4. First of all, the donor is excited either by optical or electrical pumping action (1). Then, energy from the excited donor (D*) is transferred to the acceptor (A) via a non-radiative process (2) which can be modeled using Foster-Dexter theory [14]. Finally, the acceptor relaxes into a lower

energy state by emitting a photon (3). The same process can reinitiate upon excitation of the donor.

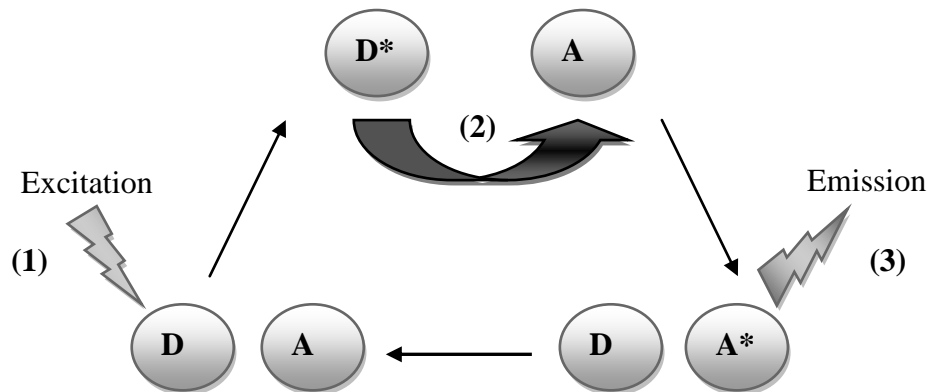**Figure 2.4:** Sensitization mechanism of the acceptor (**A**) by excitation of the donor (**D**).

(*) is used to represent an excitation state [14].

2.6 Quenching of luminescence

There are dominant effects that reduce the efficiency of the phosphor. For example, killers and concentration quenching, which are briefly discussed in this section.

2.6.1 Killers

Killers are defects caused by incidental impurities and inherent lattice defects that reduce the luminescence intensity of a phosphor [15]. The atoms and molecules adsorbed at the surface of the phosphor may reduce luminescence by producing a non-luminescent layer when they react with ambient vacuum species. Killers can affect the luminescence of phosphors in two different ways. They give rise to deep levels in the forbidden band which act as non-radiative recombination centers for free electrons in the conduction band and holes in the valence band, or the excitation energy absorbed by luminescent centers is transferred to killers without emitting radiation [15]. An iso-electronic trap is caused when an element belonging to the same column of the periodic table as that of the constituent atom of the semiconductor, is introduced and replaces the constituent atom. It can attract an electron or a hole because of the difference in electron affinity thereby becoming a killer [16].

2.6.2 Concentration quenching

An increase in the concentration of activators and co-activators to obtain brighter phosphors may result in a reduction of light output due to concentration quenching [15]. The primary cause of this quenching process is clustering of impurity ions in sol-gel glass pores at high doping levels. Non-radiative dipole-dipole interactions between ions, a process known as cross-relaxation, decrease the fluorescence intensity of certain susceptible transitions in ions. Moreover, this process has been found to be strongly concentration dependant. A lot of defects such as color center, OH⁻ and other kinds of defects may trap energy and form the quenching center.

2.7 Direct and Indirect Band gaps

In semiconductor physics, the band gap of a semiconductor is always one of two types, a direct band gap or an indirect band gap. The minimal-energy state in the conduction band and the maximal-energy state in the valence band are characterized by a certain k-vector in the Brillouin zone. If k-vectors are the same, it is called direct band gap. If they are different it is called an indirect band gap [17].

2.7.1 Direct Band gap

In direct band gap the electrons can shift from the lowest-energy state in the conduction band to the highest-energy state in the valence band without any change in crystal momentum as shown in Figure 2.5 [17].

2.7.2 Indirect Band gap

In indirect band gap the electron cannot shift from the lowest-energy state in the conduction band to the highest-energy state in the valence band without a change in the crystal momentum. Almost all of the energy comes from the photon (vertical arrow), while almost all of the momentum comes from a phonon (horizontal arrow) [17] as shown in Figure 2.5.
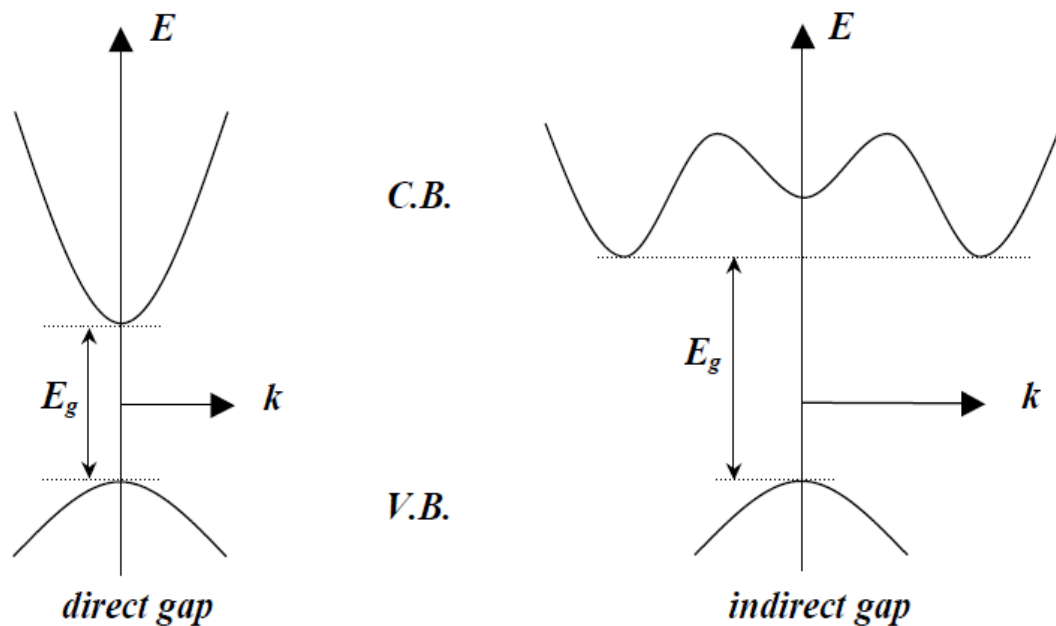
Figure 2.5: Energy vs crystal momentum for a semiconductor with direct and indirect band gap [17].

2.8 Light absorption

The exact reverse of radiative recombination is light absorption. Light with a photon energy close to the band gap can penetrate much farther before being absorbed in an indirect band gap material than a direct band gap one. This fact is very important for photovoltaics (solar cells). The absorption spectrum of an indirect band gap material usually depends more on temperature than that of a direct material, because at low temperatures there are fewer phonons, and therefore it is less likely that a photon and phonon can be simultaneously absorbed to create an indirect transition. For example, silicon starts to transmit red light at liquid helium temperatures, because red photons do not have sufficient energy for a direct process [17].

A common and simple method for determining whether a band gap is direct or indirect uses absorption spectroscopy. By plotting certain powers of the absorption coefficient against photon energy, one can normally tell both what value the band gap is, and whether or not it is direct. For a direct band gap, the absorption coefficient α is related to light frequency according to the following equation [17]:

16

$$\alpha = A^* \sqrt{h\nu - E_g} \quad \text{with} \quad A^* \approx \frac{q^2 \left(2 \frac{m_h^* m_e^*}{m_h^* + m_e^*}\right)^{3/2}}{n c h^2 m_e^*} \tag{2.1}$$

where α is the absorption coefficient, as a function of light frequency ν, h is Planck's constant ($h\nu$ is the energy of a photon with frequency ν), E_g is the band gap energy, A^* is a certain frequency-independent constant, m_e^* and m_h^* are the effective masses of the electron and hole, respectively, q is the elementary charge, n is the real index of refraction and c is the speed of light.

This formula is valid only for the light with photon energy larger, but not much larger than the band gap more specifically and assumes that bands are approximately parabolic. It ignores all other sources of absorption other than the band-to-band absorption in question, as well as the electrical attraction between the newly-created electron and hole pair. It is also valid in the case where the direct transition is forbidden, or in the case where many of the valence band states are empty or conduction band states are full [17]. On the other hand, for an indirect band gap, the equation is [17]:

$$\alpha \propto \frac{(h\nu - E_g + E_p)^2}{exp\left(\frac{E_p}{kT}\right) - 1} + \frac{(h\nu - E_g - E_p)^2}{1 - exp\left(-\frac{E_p}{kT}\right)} \tag{2.2}$$

where E_p is the energy of the phonon that assists in the transition, k is the Boltzmann's constant and T is the thermodynamic temperature. If a plot of $h\nu$ versus α^2 forms a straight line, it can normally be inferred that there is a direct band gap, measurable by extrapolating the straight line to $\alpha = 0$ axis. On the other hand, if a plot of $h\nu$ versus $\alpha^{1/2}$ forms a straight line, it can normally be inferred that there is an indirect band gap, measurable by extrapolating the straight line to the $\alpha = 0$ axis assuming that $E_p \approx 0$.

2.9 Solid State Structure

In solid materials, the way atoms or molecules arrange themselves contribute to the appearance and the properties of the materials. Atoms can be gathered together as an aggregate through a number of different processes, including condensation, pressurization, chemical reaction, electrodeposition and melting [18]. The process usually determines, at least initially, whether the collection of atoms will take a form of a gas, liquid or solid. The

state usually changes as its temperature or pressure is changed. Melting is the process most often used to form an aggregate of atoms. When the temperature of a melt is lowered to a certain point, the liquid will form either a crystalline solid or an amorphous solid [18,19].

2.9.1 Amorphous Solids

A solid substance with its atoms held apart at equilibrium spacing, but with no long-range periodicity in atom location in its structure is an amorphous solid [18]. Examples of amorphous solids are glass and some types of plastic. They are sometimes described as super cooled liquids because their molecules are arranged in a random manner somewhat as in the liquid state. For example, glass is commonly made from silicon dioxide or quartz sand which has a crystalline structure. When the sand is melted and the liquid is cooled rapidly enough to avoid crystallization, an amorphous solid called glass is formed. Amorphous solids do not show a sharp phase change from solid to liquid at a definite melting point, but rather soften gradually when they are heated. An illustration of a crystalline and amorphous SiO_2 is shown in Figure 2.7. Glassy SiO_2 and ZrO_2 investigated in this study were amorphous and ZnS and ZnO were crystalline.
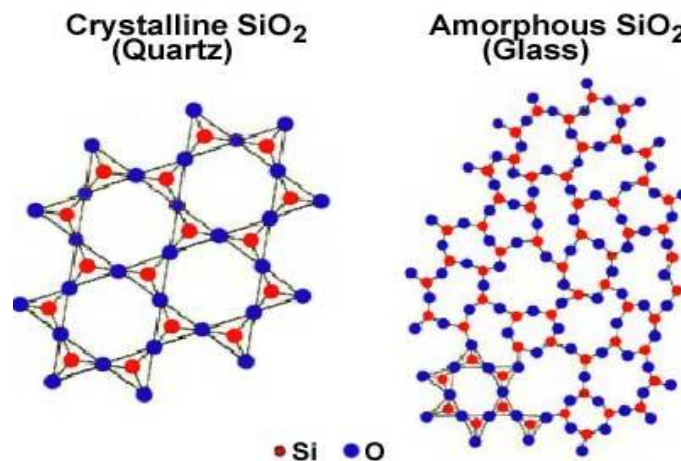

Figure 2.7: Structure of Crystalline and Amorphous SiO_2 [18]

2.9.2 Crystalline solids

A crystal is a regular, repeating arrangement of atoms or molecules [18]. The majority of solids, including all metals, adopt a crystalline arrangement because the amount of stabilization achieved by anchoring interactions between neighboring particles is at its greatest when the particles adopt regular (rather than random) arrangements. In the crystalline arrangement, the particles pack efficiently together to minimize the total intermolecular energy. The regular repeating pattern that the atoms arrange in is called the crystalline lattice, and scanning tunneling microscope (STM) makes it possible to image the electron cloud associated with individual atoms at the surface of a material [18]. An example of a crystalline SiO_2 is shown in Figure 2.7.

2.10 Defects in solid materials

Crystalline solids have a very regular atomic structure, that is, the local positions of atoms with respect to each other are repeated at the atomic scale. These arrangements are called crystal structures, and their study is called crystallography. However, most crystalline materials are not perfect; the regular pattern of atomic arrangements is interrupted by crystal defects [17]. Defects are considered in this study because they can behave as traps for radiative recombination in as much as they can be killer canters (non-radiative centers). The various types of defects are discussed in the following sections.

2.10.1 Point Defects

Point defects are localized disruptions in perfect atomic or ionic arrangements in a crystal structure. The disruption affects a region involving several atoms or ions. These imperfections may be introduced by movement of the atoms or ions when they gain energy by heating during the processing of the material by introduction of impurities or doping [20]. Also amorphous solids may contain defects, these are naturally somewhat hard to define but sometimes their nature can be quite easily understood. For instance, in ideally bonded amorphous silica all Si atoms have 4 bonds to O atoms with only one Si bond (a dangling bond) that can be considered a defect in silica [21]. There are three types of point defects, namely, vacancies, interstitial defects and substitutional defects.

2.10.1.1 Vacancies

Vacancies are sites which are usually occupied by an atom, but which are unoccupied. If a neighboring atom moves to occupy the vacant site, the vacancy moves in the opposite direction to the site which used to be occupied by the moving atom. A vacancy in a crystal structure is shown in Figure 2.8.
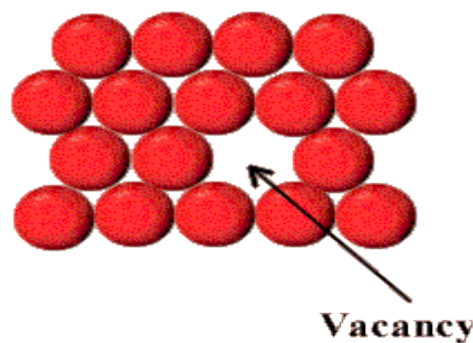

Figure 2.8: A vacancy in a crystal structure [21].

The stability of the surrounding crystal structure guarantees that the neighboring atoms will not simply collapse around the vacancy. In some materials, neighboring atoms actually move away from a vacancy, because they can form better bonds with atoms in the other directions. Vacancies play an important role in determining the rate at which atoms or ions can move around or diffuse in a solid material, especially in pure metals. A vacancy (or pair of vacancies in an ionic solid) is sometimes called a Schottky defect [21].

2.10.1.2 Interstitial defects

An interstitial defect is formed when an extra atom is inserted into the crystal structure at normally unoccupied positions. They are generally high energy configurations. Small atoms in some crystals can occupy interstices without high energy [21]. Interstitial atoms, although much smaller than the atoms located at the lattice points, are still larger than the interstitial sites they occupy. Consequently, the surrounding crystal region is compressed and distorted. An interstitial atom in a crystal structure is shown in Figure 2.9.
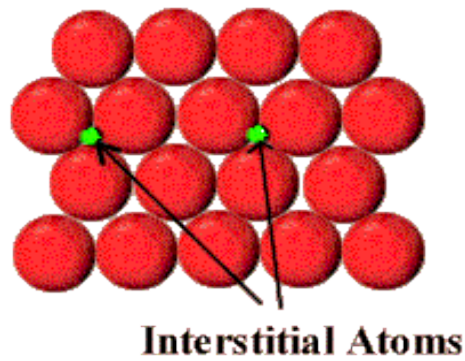
Figure 2.9: Interstitial atoms in a crystal structure [21].

2.10 .1.2 Substitutional defects

A substitutional defect is introduced when one atom is replaced by a different type of an atom. The substitutional atoms occupy the normal lattice site. These atoms may either be larger than the normal atoms in the crystal structure, in which case the surrounding interatomic spacing is reduced or smaller causing the surrounding atoms to have larger interatomic spacing. This means there are strains imposed on the lattice. A substitutional atom in a crystal lattice is shown in Figure 2.10
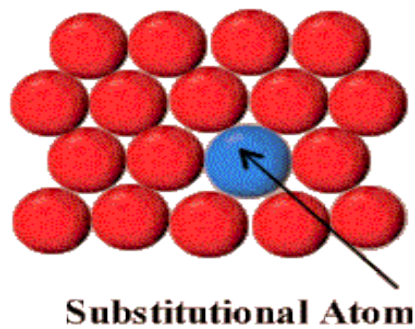

Figure 2.10: Substitutional atom in a crystal structure [21].

2.10.2 Linear defects

Linear defects occur when a crystal structure contains misaligned planes of atoms. They are referred to as dislocation since atoms are dislocated from their positions in the lattice. There are two basic types of dislocations, the edge dislocation and the screw dislocation. Edge dislocations are caused by the termination of a plane of atoms in the middle of a crystal. In such a case, the adjacent planes are not straight, but instead bend around the edge of the terminating plane so that the crystal structure is perfectly ordered on either side. The analogy with a stack of paper, if a half a piece of a paper is inserted in a stack of paper, the defect in the stack is only noticeable at the edge of the half sheet. An edge dislocation is shown in Figure 2.11.
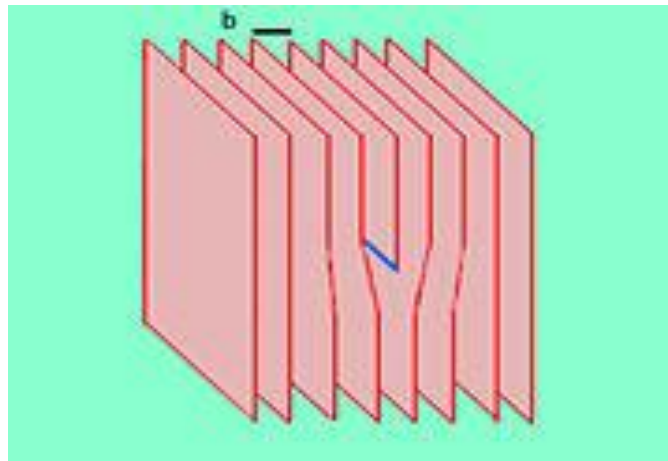

Figure 2.11: An edge dislocation, the dislocation line is represented by blue angled line, the burgers vector **b** in black [21].

The screw dislocation is more difficult to visualize, but basically comprises a structure in which a helical path is traced around the linear defect (dislocation line) by the atomic planes of atoms in the crystal lattice. The presence of a dislocation results in the lattice strain (distortion). The direction and magnitude of such distortion is expressed in terms of a burgers vector (b). For the edge type, b is perpendicular to the distortion line, whereas in the case of the screw type it is parallel. In metallic materials, b is aligned with close-packed crystallographic directions and its magnitude is equivalent to one interatomic spacing [21].

Dislocations can move if the atoms from one of the surrounding planes break their bonds and rebinds with the atoms at the terminating edge. It is the presence of dislocations and their ability to readily move (and interact) under the influence of stresses induced by external loads that leads to the characteristic malleability of metallic materials. Dislocations can be observed using transmission electron microscopy, field ion microscopy and atom probe techniques in semiconductors, mainly silicon [21].

2.11 Applications of phosphors

The applications of phosphors can be classified as (i) Light sources represented by light emitting diodes (LEDs), (ii) display devices represented by cathode-ray-tubes and (iii) other simple applications that involve persistent glow.

2.11.1 Light Sources

Phosphors can be used in as light sources in LEDs, Figure 2.12, which can in turn be used to replace incandescent lamps, especially where a colored light source is needed. LEDs are often used as display lights, warning lights and indicating lights. This colored light source application arises from an LED emitting radiation that produces an inherently colored light. The colored light from an LED is dependent on the type of semiconductor material relied upon and its physical characteristics. The LED has not been acceptable for lighting uses where a bright white light is needed, due to the inherent color [22].

Figure 2.12: Light Emitting Diode [22].

2.11.2 Displaying devices

A monitor or display is a piece of electrical equipment which displays images generated by devices such as computers, without producing a permanent record [23]. The monitor comprises the display device, circuitry and a vacuum enclosure. The display device in modern monitors is typically a thin film transistor liquid crystal display (TFT-LCD), while older monitors use cathode ray tubes (CRT). A schematic diagram of the CRT is shown in figure 2.13. It consists of an electron gun (cathode) located at the rear and a phosphor coated screen (anode) in front. The phosphor coatings are in a group of three, namely red, green and blue and this referred to as RGB system. The color image is formed by rastering when a beam of electron from the gun hits the screen [23].
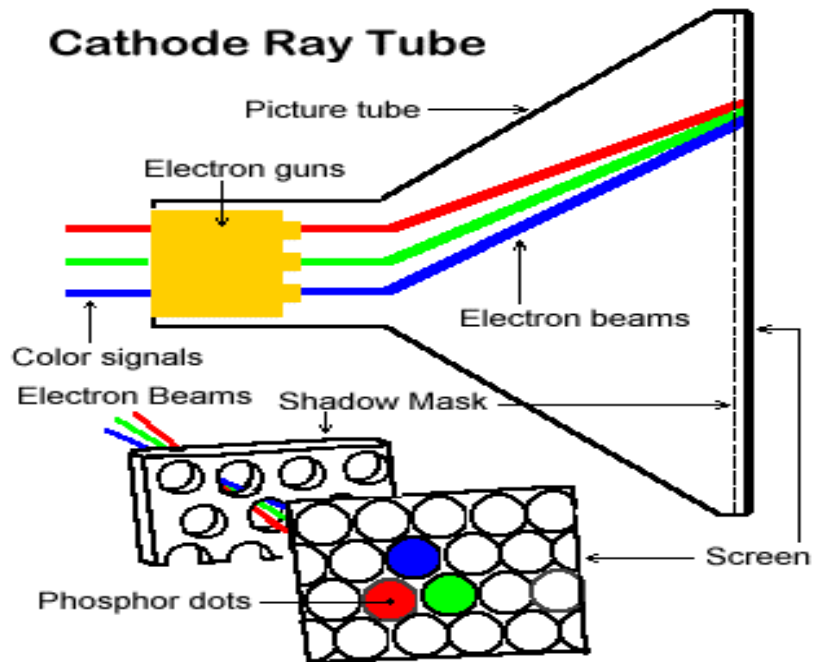
Figure 2.13: Cathode ray tube [23].

2.11.3 Phosphors with a long persistent glow

The wrist watch or a clock that continues to glow overnight is due to the phenomenon called phosphorescence. In simple terms, phosphorescence is a process in which energy absorbed by a substance is released relatively slowly in the form of light after cutting off the primary excitation. This is in some cases the mechanism used for glow-in-the-dark materials which are charged by exposure to light. Unlike the relatively swift reactions in a common fluorescent tube, phosphorescent materials used for these materials absorb the energy and store it for a longer time as the processes required to re-emit the light occur less often [24]. Figure 2.14 shows the glow in the dark materials.

Figure 2.14: Glow in the dark Materials [24].

Phosphors with long persistent glow have unique applications such as indicators in the dark for safety purposes or power-saving. Fabrics mixed with these phosphors can be made and glowing shirt or shoes can be designed, as shown in figure 2.14.

References

[1] http://www.lenntech.com/periodic/elements/pr.htm [10 October 2009]

[2] D.A Simpson, B.Sc Hons dissertation, Victoria University, Australia

[3] Michel J.F Digonnet.handbook of rare-earth doped fiber lasers and amplifiers, 2nd edition,New York, 2001

[4] Y.C Li, Y.H Chang, Y.F Lin, Y.S Chang and Y.J Lin, *Journal of Physics and Chemistry of Solids* **68**(2007) 1940-1945

[5] Brian Ray, *Electronic Materials from Silicon to Organics*, edited by L.S miller and J.B Mullin

[6] P. Boutinaud, E. Pinel, M. Dubois, A.P. Vink and R. Mahiou, *Journal of Luminescence* **69-80** (2005)111

[7] L.B Shaw, B.B Harbison, B.Cole, J.S Sanghera and I.D Aggarwal, *"Spectroscopy of the IR transitions in Pr^{3+} doped heavy metal selenide glasses"* **1**(1997)

[8] O.M. Ntwaeaborwa, PhD dissertation, University of the Free State, South Africa, 2006.

[9] T.H Gfroerer.,*Encyclopedia of Analytical Chemistry* (2000) 9209-9231

[10] Mark R. Davidson, Paul Holloway, "phosphor technology", in accessscience@McGraw-Hill, http://www.accessscience.com, DOI 10.1036/1097-8542.YB041080 [6 October 2009]

[11] http//legacy.mse.ufl.edu/~phol/research1.htm [10 October 2009]

[12] Inventors,feb 2005,pp1-3

http://inventors.about.com/library/inventors/blphotoluminesvence.htm [10 October 2009]

[13] D.R Vij, *Luminescence of Solids, Plenum Press, New York* (1998) 95.

[14] Sensitized photoluminescence and forster-dexter theory (chapter3) [10 October 2009]

[15] M.S Dhlamini, PhD dissertation, University of the Free State, South Africa, 2008.

[16] K.T Hillie, PhD dissertation, University of the Free State, South Africa, 2001

[17] http://en.wikipedia.org/wiki/direct_and_indirect-band_gaps [10 October 2009]

[18]http://www.ndt-ed.org/EducationResources/CommunityCollege/Materials/Structure [10 October 2009]

[19] http://www.absoluteastronomy.com/topics/Amorphous_solid

[20] E.Coetsee, M.Sc dissertation, University of the Free State, South Africa, 2006

[21] http://en.wikipedia.org/wiki/Crystallographic_defect [10 October 2009]

[22] http://www.patentstorm.us/patents/6278135/description.html [10 October 2009]

[23] http://en.wikipedia.org/wiki/Computer_monitor [10 October 2009]

[24] http://en.wikipedia.org/wiki/Phosphorescence [10 October 2009]

Chapter 3

Theory of Research Techniques

3.1 Introduction

In this chapter, a brief description of different research techniques used to characterize the powder phosphors is given. The techniques include x-ray diffraction (XRD), transmission electron microscopy (TEM), scanning electron microscopy (SEM) and Auger electron spectroscopy (AES). The elemental composition on the surfaces of the powder phosphors during electron or x-ray bombardment were monitored with energy x-ray dispersive spectroscopy (EDS). The TEM and SEM were used to determine the morphology of the powders. The XRD and TEM were used to identify the crystalline phases and crystallite size. UV-1700 PharmaSpec Uv-Vis spectrophotometer, fiber optics PC2000 Spectrometer and 325 nm helium cadmium (He-Cd) laser were used to measure absorption, cathodoluminescence (CL) and Photoluminescence (PL) of the powder phosphors respectively.

3.2. X-ray Diffraction

X-ray diffraction (XRD) is a versatile, non-destructive technique used to determine the crystallographic structure of natural and manufactured materials [1]. It is also used in applications such as phase identification, grain size determination, composition of solid solution, lattice constants, and degree of crystallinity in a mixture of amorphous and crystalline substances [2]. A diffraction pattern is produced when a material is irradiated with a collimated beam of x-rays. The x-ray spectra generated by this technique provide a structural fingerprint of the material. The relative peak height is generally proportional to the number of grains in a preferred orientation and the peak positions should be reproducible [2].

Figure 3.1 shows the schematic diagram of the x-ray diffractometer, with x-ray tube, the flat specimen holder and the goniometer circle (labeled measuring circle in the diagram) which remains constant through the analysis and is defined by the position of the target. The x-ray tube, specimen and receiving slit also lie on the arc of the focusing lens. The incident angle , a filter which is used to remove all but the desired Kα radiation and a slit on the incident beam side used to narrow the beam so that it is confined within the area of the specimen are shown on the figure.
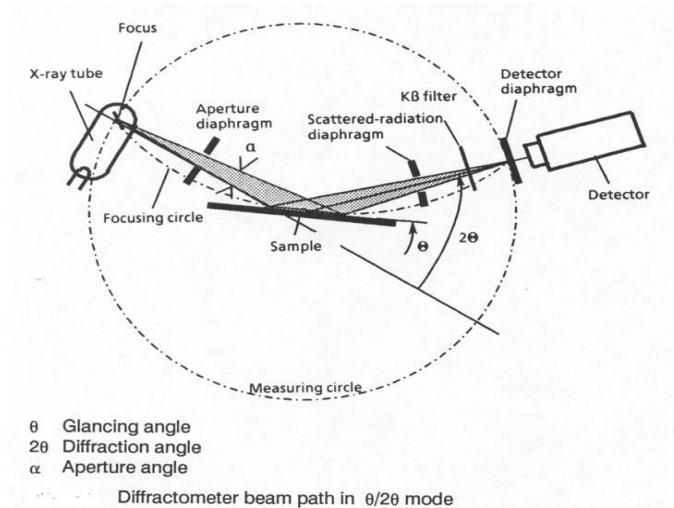

Figure 3.1: Schematic diagram of diffractometer system [3].

The x-ray diffractometer used in this study was a Siemens Diffractometer D500 equipped with Cu Kα source shown in Figure 3.2.

Figure 3.2: Siemens D500 model x-ray diffractometer

3.3 Transmission Electron Microscopy

Transmission electron microscopy (TEM) is an imaging technique in which a beam of electrons is transmitted through a specimen, and then an image is formed. The image is then magnified and directed to appear either on a fluorescent screen or layer of photographic film, or to be detected by a sensor such as a CCD camera [3]. The system can study small details in the cell or different materials down to near atomic levels [4,5]. It can investigate the size, shape and arrangement of the particles which make up the specimen as well as their relationship to each other on the scale of atomic diameters. Materials to be analyzed with this technique need to have dimensions small enough to be electron transparent and that can be produced by the deposition of a dilute suspension containing the specimen onto support grids. The suspension is normally a volatile solvent such as ethanol that can evaporate to allow the specimen to settle on the grids.

Figure 3.3 shows the schematic diagram of the transmission electron microscopy, with an electron gun which provides the source of illumination, electromagnetic lenses which focus the electron beam and then magnify the image. It also consists of apertures, which limit the angular spread of the beam and are crucial in controlling contract. An image is formed by accelerating a beam of electrons that pass through the specimen. These electrons are scattered at different angles depending on the density of the atom it encounters. An electron can either be (a) undeflected, (b) deflected but loses no energy (elastically deflected), or (c) loses a significant amount of energy and is probably deflected (inelastically). The different scattered angles produce a contrasting image because all angles scattered more than 0.5 degrees are stopped by an objective aperture situated below the specimen. The image is projected on a fluorescent screen where phases, fractures and other properties that are 2 to 3Å across can be seen [4]. FEI Tecnai F20 microscope at an accelerating voltage of 200 kV was used in this study.
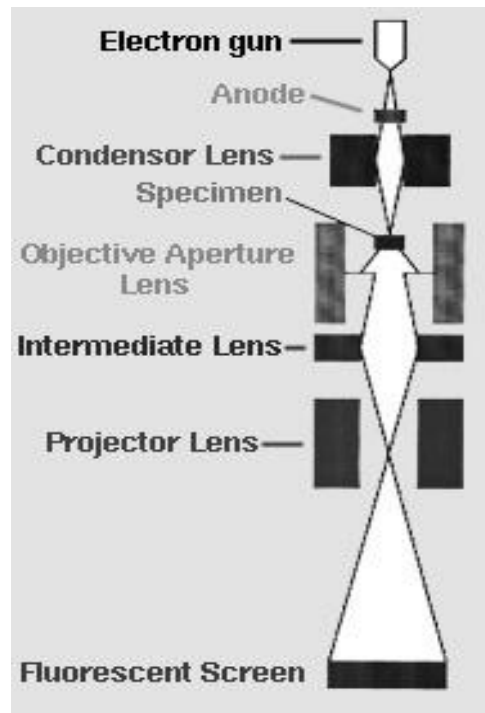
Figure 3.3: The schematic diagram of TEM [15].

3.4 Scanning Electron Microscopy

Scanning electron microscopy (SEM) is a technique in which a beam of energetically well-defined and highly focused electrons is scanned across a material (sample). The technique can provide material's information about topography and morphology [6]. If the system is equipped with energy dispersive x-ray spectrometer (EDS), it can also provide information about chemical composition of the material [7]. The basic principle of the system is that, the electron beam impinges the surface and generates a splash of electrons with kinetic energies much lower than the primary incident electrons called secondary electrons.

An image of the sample surface is constructed by measuring secondary electron intensity as a function of the primary beam position. The SEM has many advantages over traditional light microscopes. It has large depth of field, which allows more of a specimen to be in focus at one time. The SEM also has much higher resolution, such that closely spaced specimens can be magnified at much higher levels. Because the SEM uses electromagnets rather than lenses, the user has much more control in the degree of magnification. All of these advantages, as

well as the actual strikingly clear images, make the scanning electron microscope one of the most useful instruments in research today [8].

A simplified layout of a SEM is shown in Figure 3.4, consisting of an electron gun, magnetic lens used to form the beam and limit the amount of current in the beam, and detectors. Electrons are produced via a thermionic emission from an electron gun and focused down to a spot on the specimen by a system of ion optics (i.e. electromagnetic coils). A set of scan coils are used to scan the spot over the surface of the sample and reflected electrons are collected, amplified and converted into a video signal. Thus, a micrograph of the specimen is obtained in the form of a 2-D plot of the reflected spot.
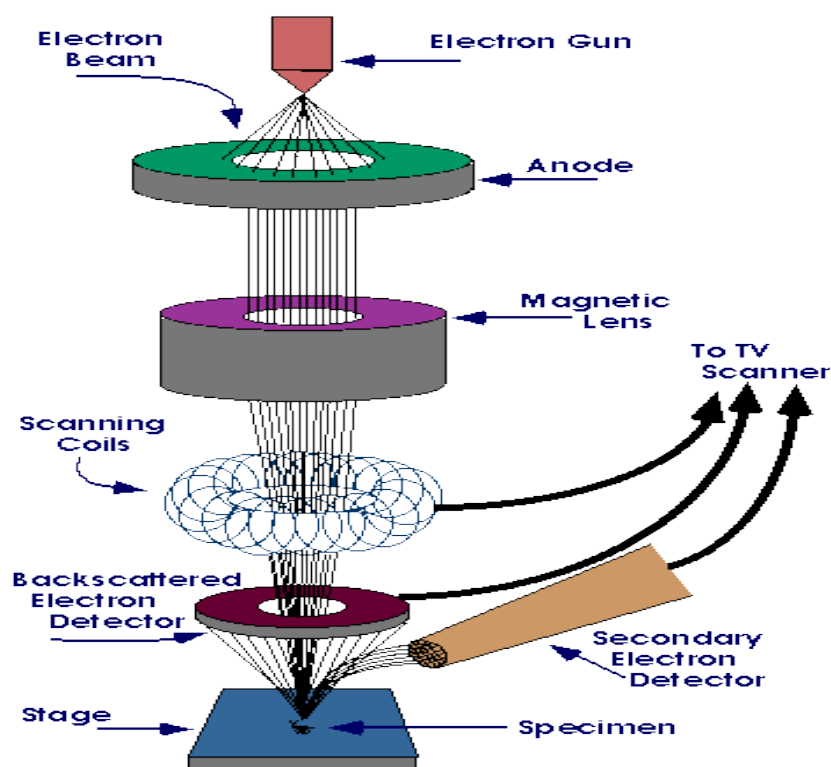

Figure 3.4: A simplified layout of a SEM [8].

The SEM images of powder phosphors in this study were obtained using Shimadzu super scan Scanning Electron Microscope model SSX550 shown in Figure 3.5.
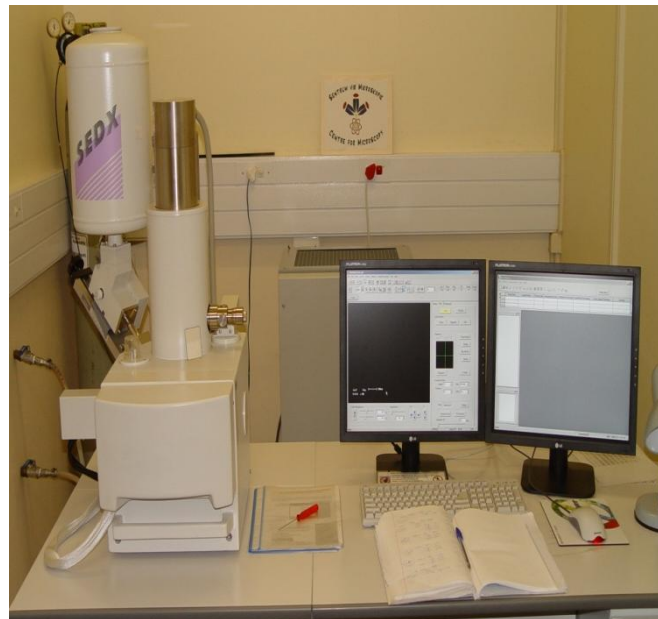
Figure 3.5: Shimadzu Super Scan SSX550 model Scanning Electron Microscope.

3.5 Auger Electron Spectroscopy

Auger electron spectroscopy is a common analytical technique used specifically to study the surfaces and more generally in the area of material science [9]. It was developed in the late 1960's, and it derives its name from the effect first observed by Pierre Auger [10], a French Physicist, in the mid-1920's. It is based on the measurement of the kinetic energies of the emitted auger electrons. Auger spectroscopy can be considered as involving three basic steps:

1. Atomic ionization (by removal of a core electron)
2. Electron emission (the Auger process)
3. Analysis of the emitted Auger electrons

In Auger process, a high-energy (2-10keV) primary electron irradiates and liberates a core level (K-level) electron thereupon ionizing the atom, as shown in Figure 3.6
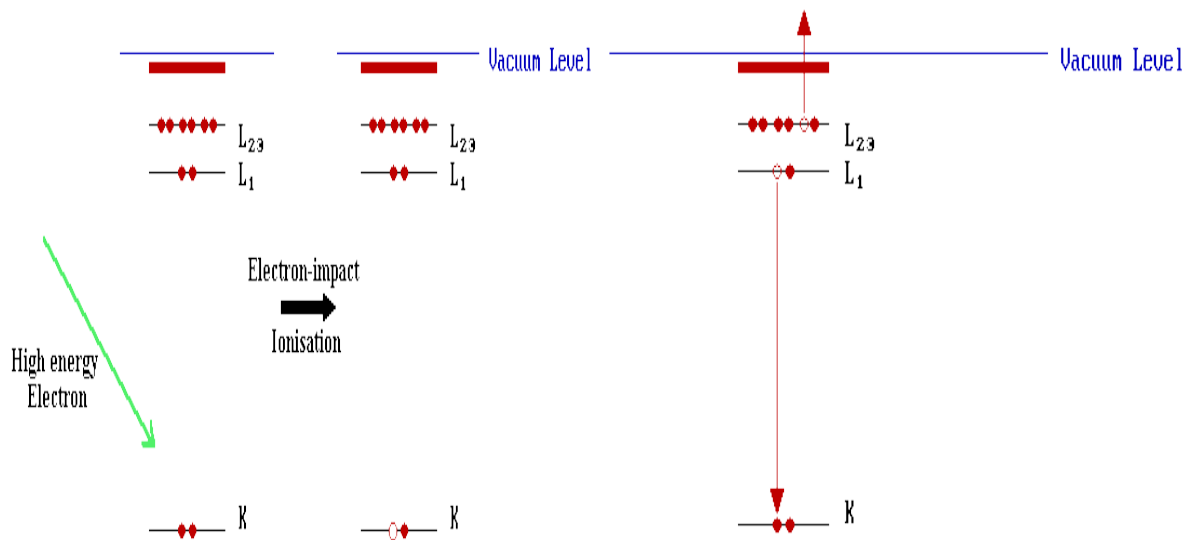
Figure 3.6: Illustration of Auger process [11].

The ionized atom that remains after the removal of the core hole electron is in a highly excited state and will rapidly relax back to a lower energy state. For this atom to reorganize itself to a lower energy state, an electron from the higher level (L_1 level) will drop to the lower level to fill the void caused by the liberated electron. The energy released in the transition is either emitted as a photon or given to another electron in the higher level ($L_{2,3}$ level). If the energy is sufficient, this electron can be ejected from the surface and detected as an auger secondary electron. The emitted electron is known as a KLL electron. The system can detect and analyze all elements with the exception of hydrogen (H) and helium (He) because they do not have electrons occupying the L level (have less than three electrons). In the Auger process the final state is a doubly ionized atom with core holes in the L_1 and $L_{2,3}$ shells and rough estimate of the kinetic energy of the Auger electron from the binding energies of the various levels involved can be made:

$$KE = (E_k - E_{L1} - E_{L2,3}) \tag{3.1}$$

Auger spectroscopy can also be used for depth profiling with the use of an ion gun as part of the vacuum system. As the ion gun etches away the material, the electron probe focused on the same spot can give information about the composition of the surface layers with sputter depth. The PHI model 549 Auger spectrometer used in this study is shown in Figure 3.7.

Figure 3.7: The PHI model 549 Auger spectrometer.

3.6 Cathodoluminescence Spectroscopy

Cathodoluminescence spectroscopy was used to study the CL efficiency of the SiO_2:Pr^{3+} powder phosphor. Cathodoluminescence is an optical and electrical phenomenon where a beam of electrons generated by an electron gun impacts on a phosphor causing it to emit visible light. In the case of the semiconductor, the CL energy is equivalent to the energy gap between the conduction band and the valence band. In this study an Ocean Optics S2000 Spectroscopy (optical fiber) was coupled with an AES system in order to collect CL data, see Figure 3.8.
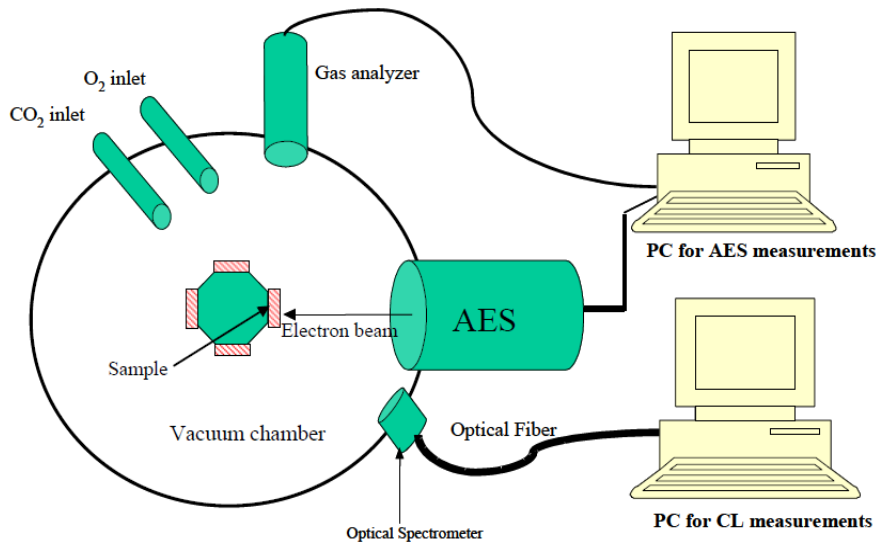
Figure 3.8: Schematic illustration of AES coupled with optical Spectrometer and gas analyzer.

3.7. UV- Visible Spectrophotometer

An instrument used in the ultraviolet-visible spectroscopy is called UV/Vis spectrophotometer [12]. It measures the intensity (I) of the light passing through a sample, and compares it to the intensity (I_o) of the light before it passes through the sample. The ratio I/I_o is called the transmittance, and is usually expressed as the percentage (%T). The absorbance (A) is based on the transmittance:

$$A = -\log\left(\frac{\%T}{100}\right) \tag{3.2}$$

The basic parts of the spectrophotometer are a light source, a holder of a sample, a diffraction grating or monochromator to separate the different wavelengths of light, and a detector. The radiation source is often a Tungsten filament (300-2500 nm) and a deuterium arc lamp which is continuous over the ultraviolet region (190-400 nm). The detector is typically a photodiode or a charge coupled device (CCD). Photodiodes are used with monochromators, which filter the light so the only light of a single wavelength reaches the detector. Diffraction gratings are used with CCDs, which collects light from the different wavelengths on different pixels [12]. A spectrophotometer can either have a single beam or double beam configuration. The single beam configuration (see Figure 3.9) allows only one beam to pass through the sample

compartment. First, the transmittance is set to 100% or the absorbance to 0 using the cell filled with a solvent and then the cell with the sample in it is measured.
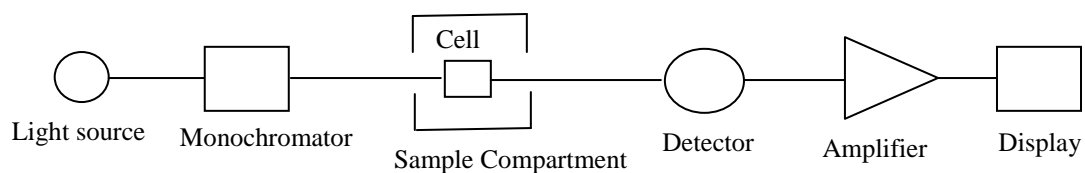
Figure 3.9: Single beam configuration.

In the double beam configuration (see Figure 3.10), the monochromatic light is divided into two beams using mirrors such as a rotating mirror and a semi-transparent mirror so as to make two beams, the sample beam and the reference beam. When the sample cell with sample in it is placed for the sample beam and the reference cell with solvent in it is placed for the reference beam in the sample compartment, each transmitted and absorbance can be measured once from the sample sign *I* and the reference sign *Io* at one time. UV-Visible spectrophotometer used in this study is shown in Figure 3.11.

Figure 3.10: Double beam configuration.

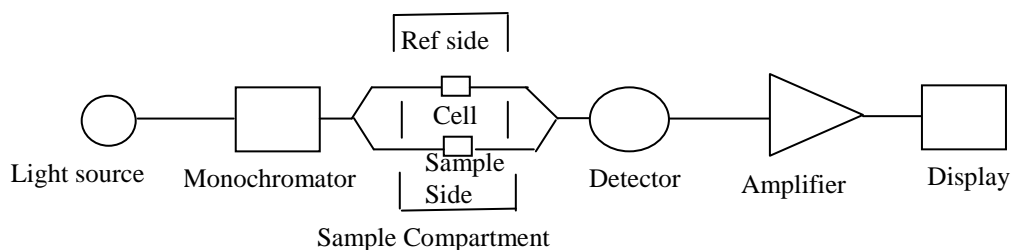**Figure 3.11:** UV-1700 PharmaSpec UV-Vis spectrophotometer.

3.8 Photoluminescence Spectroscopy (He-Cd Laser)

The Helium-Cadmium (He-Cd) laser is one of a class of gas lasers using helium in conjunction with a metal which vaporizes at a relatively low temperature. A typical construction for the He-Cd laser is in the form of a tube, terminated by two Brewster's angle windows, with the two laser mirrors mounted separated from the tube. The tube filled with helium, also has a reservoir containing the Cd and a heater to vaporize the metal [13]. The reservoir is raised to a high enough temperature ($\sim 250^{o}$C) to produce the desired vapour of Cd atoms in the tube. He-Cd laser can give output powers of 50-100 mW and it can produce a high quality beam at 442 nm (violet-blue) or 325 nm (UV) depending on the optics [13].

Photoluminescence (PL) is simple, versatile and non-destructive. The instrumentation that is used for ordinary PL work is modest, an optical source and an optical power meter or spectrophotometer. A typical PL setup is shown in Figure 3.12. Because the measurement does not rely on electrical excitation or detection, sample preparation is minimal. This feature makes PL particularly attractive for material systems having poor conductivity or undeveloped contact or junction technology. The 325 nm He-Cd Laser used in this study is shown in Figure 3.13.
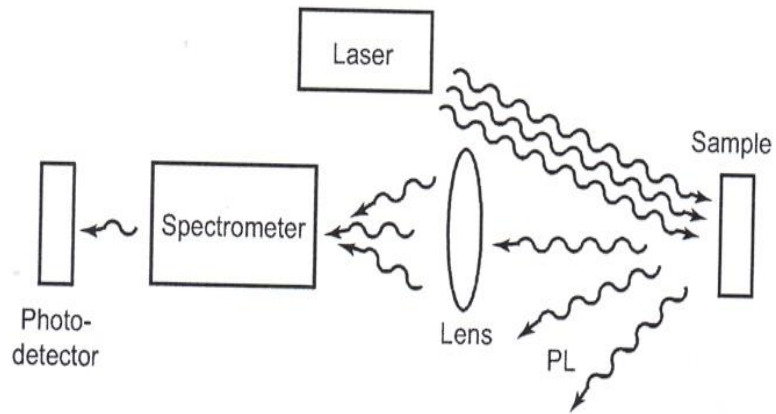
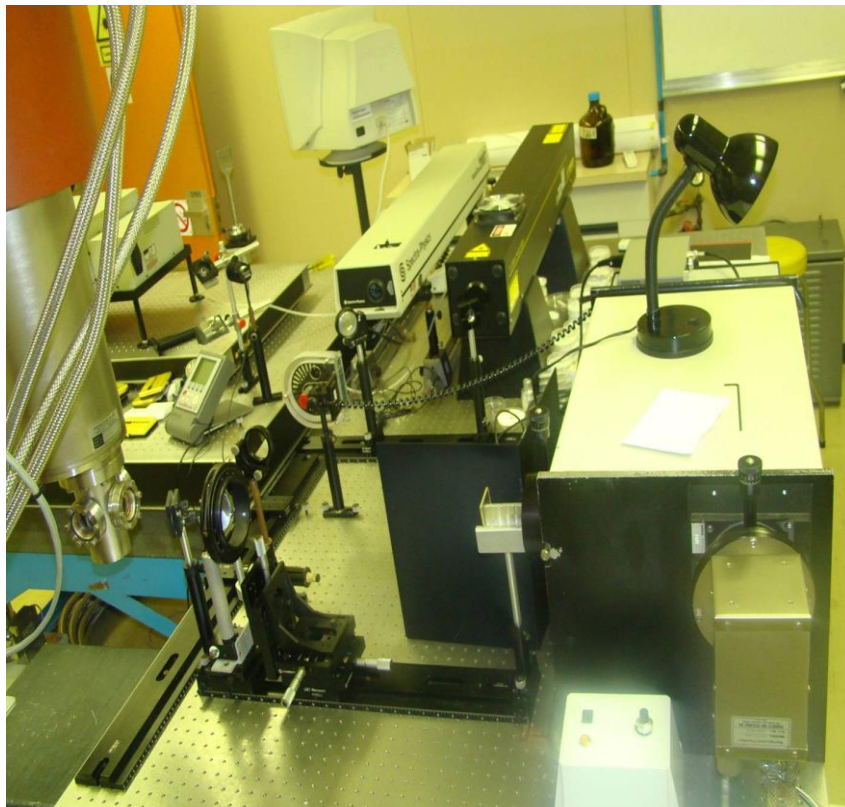**Figure 3.12:** A typical experimental set-up for PL measurements [14].

Figure 3.13: He-Cd (325nm) laser used for photoluminescence.

References

[1] http://www.panalytical.com/index.cfm?pid=135 [16 October 2009]

[2] G.Cao, Nanostructures and Nanomaterials :Synthesis, Properties & applications. 6th edition, London, 2004.

[3] J.R. Connolly, Introduction to x-ray powder diffraction, 2007

[4] http://en.wikipedia.org/wiki/Transmission_electron_microscopy [16 October 2009]

[5] Z.L Wang, Y. Liu, Z.Zhang, Handbook of nanophase and nanostructured materials, 4th edition, New York, 2003

[6] University of Nebrasaka-Lncon:http//www.unl.edu/CMRAcfem/semoptic.htm. [16 October 2009]

[7] Binghamton University: Nanotechnology for undergraduate education: http//nue.clt.binghamton.edu/semtem.html [16 October 2009]

[8] J.Schweitzer, Radiological and Environmental Management (REM) : http//www.purdue.edu/REM/rs/sem.htm 2008 [16 October 2009]

[9] http://en.wikipedia.org/wiki/Auger_electron_spectroscopy [16 October 2009]

[10] D. Briggs, and J.T. Grant, Surface Analysis by AES and XPS, IM publications chichesteter, England, (1998).

[11] http://www.chem.qmul.ac.uk/surfaces/scc/scat5_2.htm [16 October 2009]

[12] http://en.wikipedia.org/wiki/Ultraviolet-visible_spectroscopy [16 October 2009]

[13] O.Svelto, Principles of lasers, 4th edition, Springer, New York, 1998. [16 October 2009]

[14] T.H Gfroerer.,*Encyclopedia of Analytical Chemistry* (2000) 9209-9231

[15] http://www.gitam.edu/eresource/nano/NANOTECHNOLOGY/tem.htm [16 October 2009]

Chapter 4

Synthesis of Powder Phosphors

4.1 Introduction

A number of methods can be used to synthesize semiconductor light emitting materials. These include hydrothermal, precipitation, chemical bath, solid state reactions, spray pyrolysis, combustion and sol-gel [1]. Among these methods, sol-gel processing has been found to offer many advantages which include low processing temperature, high purity, molecular level homogeneity and more flexibility in the components of the glass [2,3,4]. Because of these advantages, the sol-gel process was used in this study to prepare Pr^{3+} doped SiO_2, ZrO_2, ZnO and ZnS phosphors. The basic concepts of the sol-gel process are discussed in the following section.

4.2 Sol-gel Process

The sol-gel process is a wet chemical route for the synthesis of colloidal dispersions (sols) of inorganic and organic hybrid materials, particularly oxides and oxides-based hybrid at relatively low temperatures.   Sols are dispersions of colloidal particles in a liquid [5] and colloids are solid particles with diameters of 1-100 nm.   The sols are converted into viscous gels (sol-gel transition) [6] by vigorous stirring at low temperatures. At the transition, the solution or sol becomes a rigid, porous mass through destabilization, precipitation or supersaturation. The sol becomes a gel when it can support stress elastically. A gel is an interconnected, rigid network with pores of submicrometer dimensions and polymeric chains whose average length is greater than a micrometer [7]. The gels can be dried at room temperature to form glass or they can be ground to make fine powders.   In the sol-gel process, the grain growth occurs at the same time as agglomeration such that it becomes difficult to differentiate between primary particles which consist of small grains or crystallites, and secondary particles which are agglomerates of primary particles [8].

Figure 4.2 shows the primary particles of about 2 nm in diameter that agglomerates in secondary particles of about 6 nm.
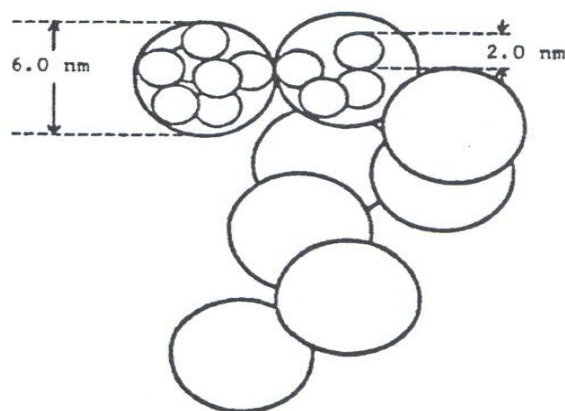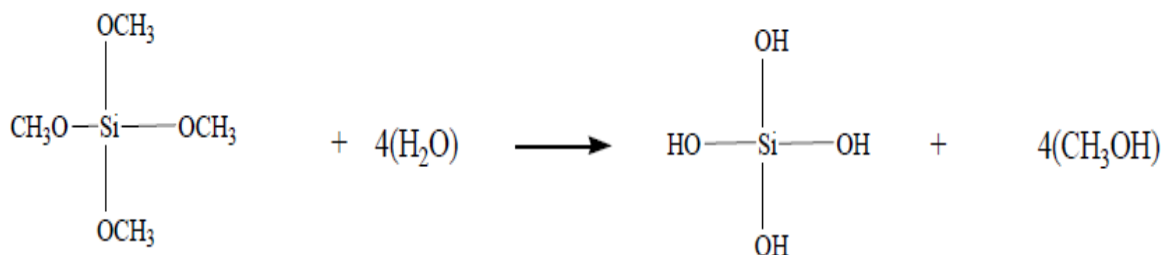

Figure 4.2.: Schematic representation of primary and secondary particles in alkoxide gel [5]

The crystal growth technique in gels has become very important because it is straight forward and can be used at room temperature, in similar conditions to those under which crystals grow naturally [7]. Thus, it enables the incorporation of the organic elements into inorganic materials without deterioration of their functionality. The sol-gel processing is particularly useful in making complex metal oxide, temperature sensitive organic-inorganic hybrid materials, and thermodynamically unfavorable or metastable materials [2]. The use of the sol-gel method has attracted great scientific interest in the recent years for making advanced materials and for designing devices with very specific properties [9].

Typical sol-gel processing consists of hydrolysis of precursors. The versatile precursors for the sol-gel synthesis of oxide are metal alkoxides, but organic and inorganic salts are also often used [9,10]. The alkoxide used most often to synthesize SiO_2 is tetraethylorthosilicate (TEOS), which is the product of the reaction of $SiCl_4$ and ethanol [6,11]. Precursors may be dissolved in organic or aqueous solvents and catalysts are often added to accelerate hydrolysis and condensation reactions. A silica gel may be formed by the network growth from an array of discrete colloidal particles or by formation of an interconnected 3-D network by the simultaneous hydrolysis and polycondensation of an organometallic precursor. A liquid alkoxide precursor such as $Si(OR)_4$, where R may be CH_3, C_2H_5, or C_3H_7 is hydrolyzed by mixing with water to form hydrated silica and alcohol as shown below.

Hydrolysis

$$CH_3O-\underset{\underset{OCH_3}{|}}{\overset{\overset{OCH_3}{|}}{Si}}-OCH_3 \quad + \quad 4(H_2O) \quad \longrightarrow \quad HO-\underset{\underset{OH}{|}}{\overset{\overset{OH}{|}}{Si}}-OH \quad + \quad 4(CH_3OH)$$

The hydrated silica tetrahedral interacts in a condensation reaction forming $\equiv$Si-O-Si$\equiv$ bonds and water. The intermediate that exist as a result of partial hydrolysis include SiOH groups, which are called an ethoxy group. A condensation can occur between a silanol and an ethoxy group to form a bridging oxygen or siloxane group Si-O-Si [6]. Condensation results in the formation of nano-scale clusters of metal oxides or hydroxides, often with organic groups embedded or attached to them. These organic groups may be due to incomplete hydrolysis or introduced as non-hydrolysable organic ligands. The nano-scale clusters size, along with the morphology and microstructure of the final product can be tailored by controlling the hydrolysis and condensation reactions. The condensation reaction is given by the following equation.

Condensation

$$HO-\underset{\underset{OH}{|}}{\overset{\overset{OH}{|}}{Si}}-OH \quad + \quad HO-\underset{\underset{OH}{|}}{\overset{\overset{OH}{|}}{Si}}-OH \quad \longrightarrow \quad HO-\underset{\underset{OH}{|}}{\overset{\overset{OH}{|}}{Si}}-O-\underset{\underset{OH}{|}}{\overset{\overset{OH}{|}}{Si}}-OH \quad + \quad H_2O$$
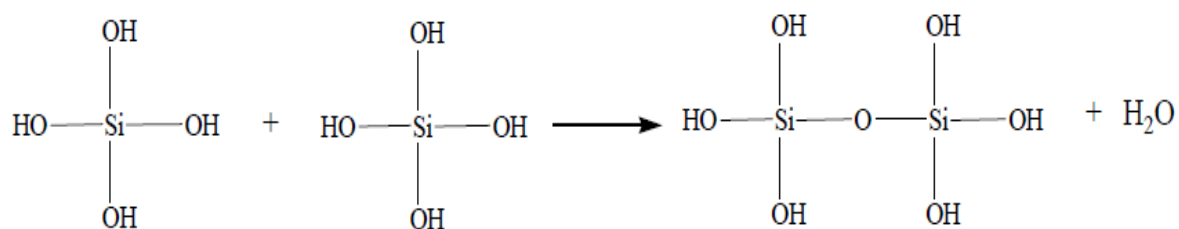
Linkage of additional $\equiv$Si-OH tetrahedral occurs as a polycondensation reaction and eventually results in a SiO_2 network. The H_2O (in condensation) and alcohol (in hydrolysis) expelled from the reaction remains in the pores of the network as shown in the following equation:

Polycondensation

OH   OH
| |
HO—Si—O—Si—OH   +   6Si(OH)₄   ⟶
| |
OH   OH

$$\text{HO—Si—O—Si—OH} \quad + \quad 6\text{Si(OH)}_4 \quad \longrightarrow$$
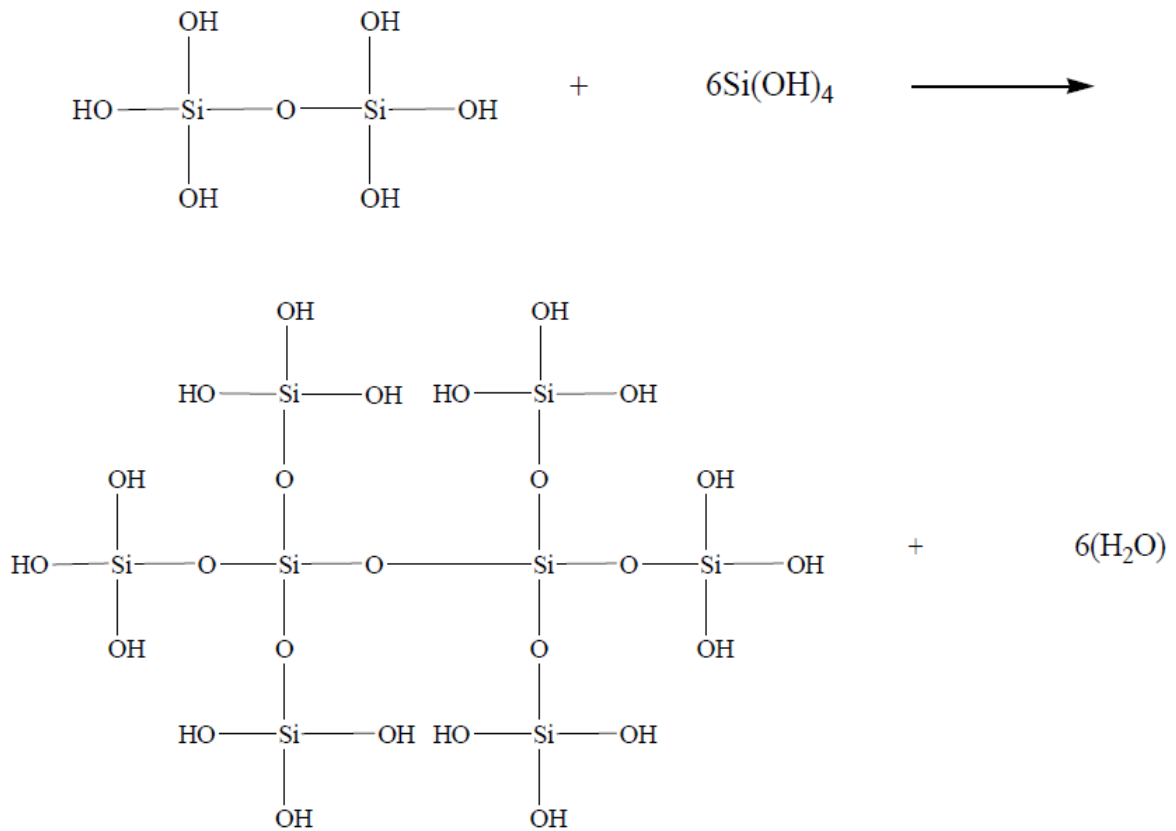
The overall equation for the formation of SiO₂ as a result of condensation reactions is given by:

$$\text{Si(OC}_2\text{H}_5)_4 \; + \; 2\text{H}_2\text{O} \; \rightarrow \; \text{SiO}_2 \; + \; 4\text{C}_2\text{H}_5\text{OH} \tag{4.1}$$

The kinetics of the reaction is impracticably slow at room temperature, often requiring several days to reach completion. For this reason, acid or base catalysts are added to the solution. Acid catalysts can be any protic acid such as HCl, HNO₃ etc. Basic catalysis usually uses ammonia or ammonium fluoride. Aerogels prepared with acid catalysts often show more shrinkage during drying and may be less transparent than base catalyzed aerogels. Under acidic conditions, the structures are mostly linear with a low degree of cross-linking while for basic conditions, characteristic of branched polymers with high degree of cross-linking have been observed. This is shown in Figure 4.3.

- **Acid-catalyzed**
  - yield primarily linear or randomly branched polymer

- **Base-catalyzed**
  - yield highly branched clusters

Figure 4.3: Summary of acid/base sol-gel conditions [12]

Despite the chemical equation shown, the mole ratio of water to TEOS is a particularly useful number for predicting the behavior of solution. When the mole ratio (R) is increased while maintaining a constant solvent, the silicate concentration is reduced. This in turn reduces the hydrolysis and condensation rates, and results in longer gel times. This behavior is shown in Figure 4.4. The most concentrated solution with ethanol: TEOS = 1, has the shortest gel time, while the most dilute solution with ethanol: TEOS = 3 takes the longest time to gel. The ratio of ethanol to TEOS is equally useful, and when omitted makes the estimation of oxide content in the solution difficult. Klein [6] reported the linear increase in gel time from the concentrated to dilute solutions. By careful control of sol preparation, monodispersed nanoparticles of various oxides, including complex oxides, organic inorganic hybrids, and biomaterials can be synthesized. The key issue here is to promote temporal nucleation followed with diffusion controlled subsequent growth.
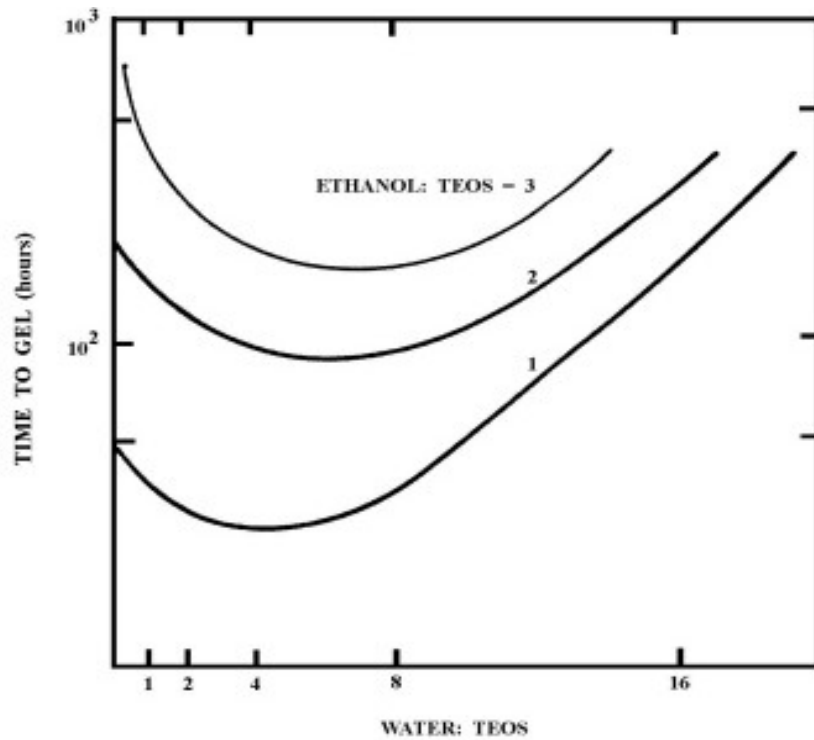
Figure 4.4: Gel times as a function of water: TEOS ratio, R [6,12]

The particle size can be varied by changing the concentration and aging time. When a gel is maintained in its pore liquid, its structure and properties continue to change long after the gel point and the process is called aging. The process is illustrated in Figure 4.5. During aging, polycondensation continues along with localized solution and reprecipitation of the network. The strength of the gel is reported to increase with aging. The liquid is removed from the interconnected pore network during drying. Large capillary stresses can develop during drying when pores are small (<20 nm) and these stresses will cause the gels to crack catastrophically unless the drying process is controlled [5]. Wet-aging increases coalescence and cause little shrinkage on drying. Structural evolution during sol to gel and gel to solid transitions needs to be fully understood to achieve real mastery of the sol-gel process [9]. The properties of a gel and its response to heat treatment are very sensitive to the structure already formed during the sol stage [9].
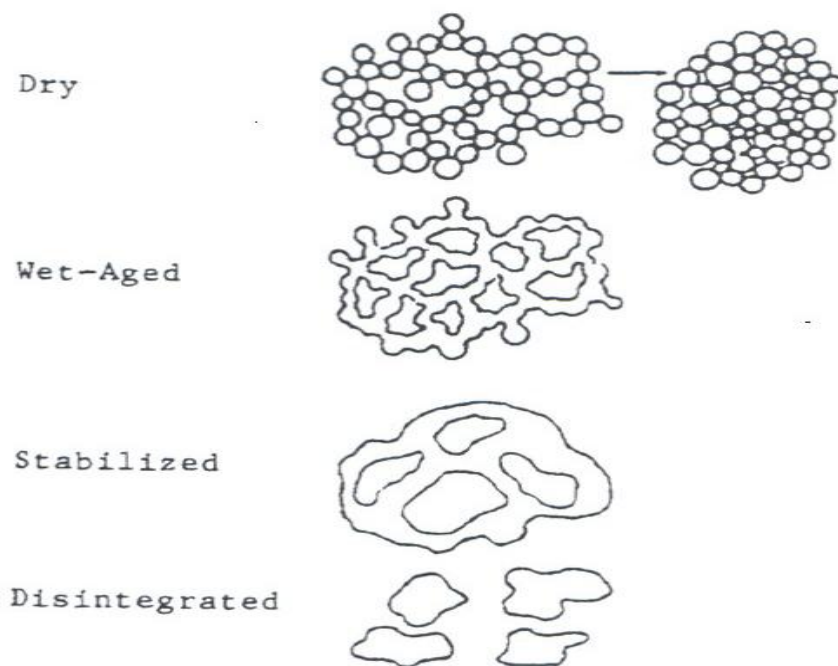
Figure 4.5: Illustration of the stages in aging process of gel [5]

4.3 Preparation of SiO$_2$:Pr^{3+} phosphor

SiO$_2$:Pr^{3+} phosphor was prepared by mixing 10 g of tetraethylorthosilicate (TEOS) solution, 5 g of ethanol (EtOH), 10 g of distilled water and 5 g of 0.15 M nitric acid (HNO$_3$). The mixture was stirred at room temperature for 1 hour. The resulting transparent solution was mixed with the desired amount of Pr (NO$_3$)$_3$.6H$_2$O dissolved in 5 g of ethanol. Different molar concentrations of Pr^{3+} were used for doping. After stirring for 1 hour the gels were allowed to dry at room temperature for ~ 10 days, were then ground to make powders and annealed in air at 600°C for 2 hours. The flow chart diagram for the preparation is given in Figure 4.6.
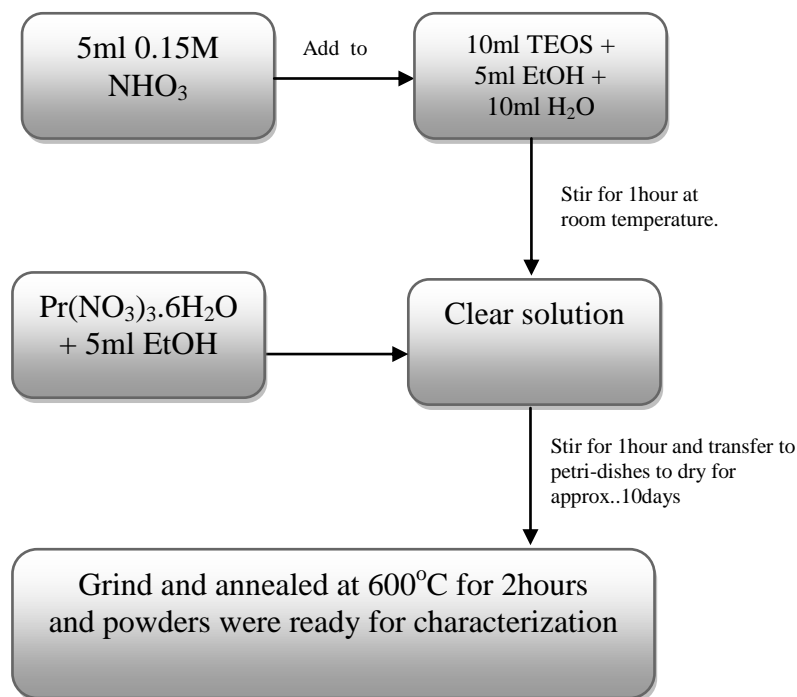
Figure 4.6: Flow chart diagram of $SiO_2:Pr^{3+}$ powder phosphor Synthesis.

4.4 Preparation of $ZrO_2:Pr^{3+}$ phosphor

$ZrO_2:Pr^{3+}$ phosphor was prepared by dissolving 10 ml of Zirconium(IV)propoxide (Zr $(OC_3H_7)_4$) in 37.7 ml of EtOH with vigorous stirring at room temperature and 5 ml of 0.15M HNO_3 was added to catalyze the reaction. 2 ml of acetyl acetate (AcAc) was added to prevent precipitation and 5 ml of deionized water was added dropwise to facilitate gelation. The resulting solution, which was pale yellow, was mixed with desired amount of $Pr(NO_3)_3.6H_2O$ dissolved in 5 ml of EtOH. Different molar concentrations of Pr^{3+} were used. After stirring for 1 hour the gels were allowed to dry at room temperature for ~ 3-4 days, then crushed into powders and annealed in air at 600^oC for 2 hours and 280^oC for an hour. The flow chart diagram for the preparation is given in Figure 4.7and the equations for the reaction are also given by Equation 4.2.
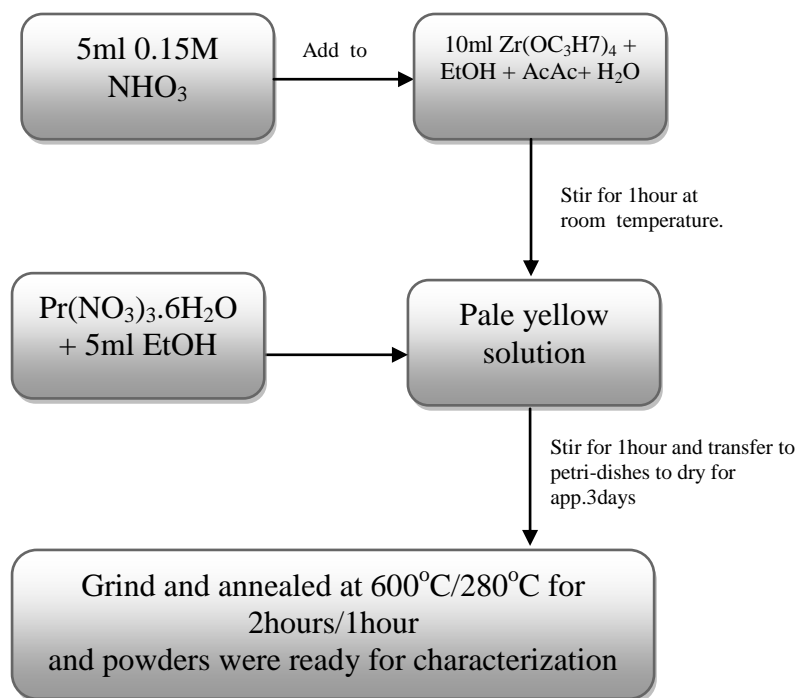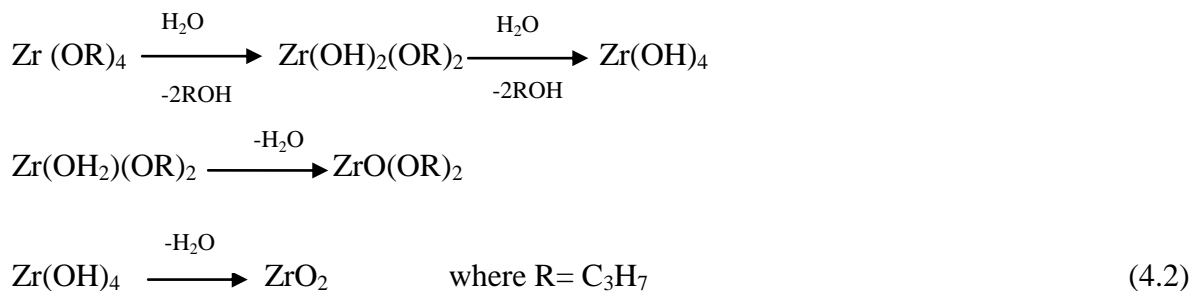
$$Zr\,(OR)_4 \xrightarrow[\text{-2ROH}]{H_2O} Zr(OH)_2(OR)_2 \xrightarrow[\text{-2ROH}]{H_2O} Zr(OH)_4$$

$$Zr(OH_2)(OR)_2 \xrightarrow{-H_2O} ZrO(OR)_2$$

$$Zr(OH)_4 \xrightarrow{-H_2O} ZrO_2 \qquad \text{where } R= C_3H_7 \qquad\qquad (4.2)$$

```
┌─────────────────┐   Add to   ┌──────────────────────┐
│  5ml 0.15M      │ ────────►  │ 10ml Zr(OC3H7)4 +    │
│  NHO3           │            │ EtOH + AcAc+ H2O     │
└─────────────────┘            └──────────────────────┘
                                          │
                          Stir for 1hour at
                          room  temperature.
                                          ▼
┌─────────────────┐            ┌──────────────────────┐
│ Pr(NO3)3.6H2O   │ ────────►  │   Pale yellow        │
│ + 5ml EtOH      │            │   solution           │
└─────────────────┘            └──────────────────────┘
                                          │
                          Stir for 1hour and transfer to
                          petri-dishes to dry for
                          app.3days
                                          ▼
              ┌────────────────────────────────────────┐
              │ Grind and annealed at 600°C/280°C for  │
              │ 2hours/1hour                            │
              │ and powders were ready for characterization │
              └────────────────────────────────────────┘
```

Figure 4.7: Flow chart diagram of ZrO_2:Pr3^{+} powder phosphor synthesis.

4.5 Preparation of ZnS:Pr^{3+} nanoparticle phosphor

ZnS:Pr^{3+} phosphor was prepared by dissolving 2 g of zinc acetate (Zn $(CH_3COO)_2.2H_2O$) in EtOH solution at $80^{\circ}C$. A 1:1 ethanol to deionized water solution was used to dissolve sodium sulphide (Na_2S) using ultrasonic bath which was then added to the zinc acetate solution dropwise with vigorous stirring at $75\text{-}80^{\circ}C$. The resulting white precipitate was centrifuged and washed using a mixture of heptane and ethanol in the 2:1 volume ratio to remove unwanted $CH3COO^-$ and Na^+ ions. The precipitate was dispersed in ethanol and the desired amount of $Pr(NO_3)_3.6H_2O$ was added. Different molar concentrations of Pr^{3+} were

49

used. The white precipitates obtained by centrifuging were dried at 90°C for 2 hours and was then annealed in air at 600°C for 2 hours. Figure 4.8 shows the flow chart diagram for the preparation and an equation for the formation of ZnS is shown in Equation 4.3:
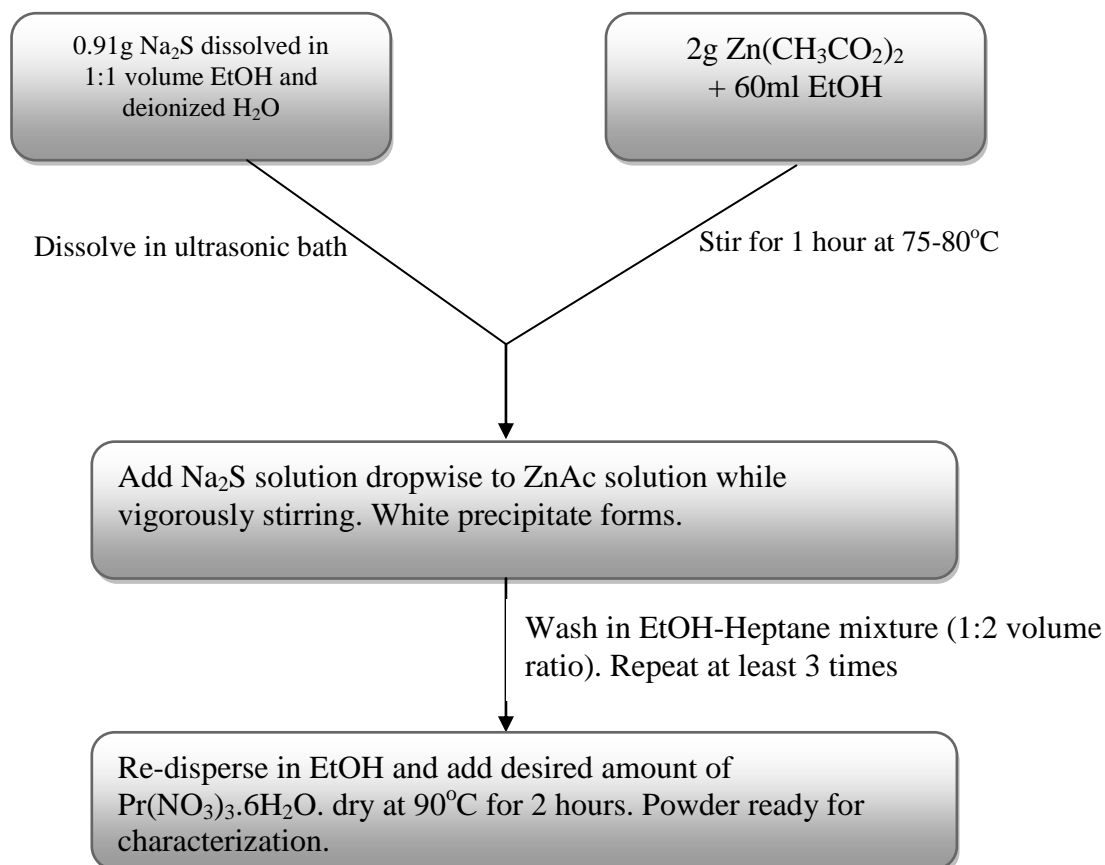
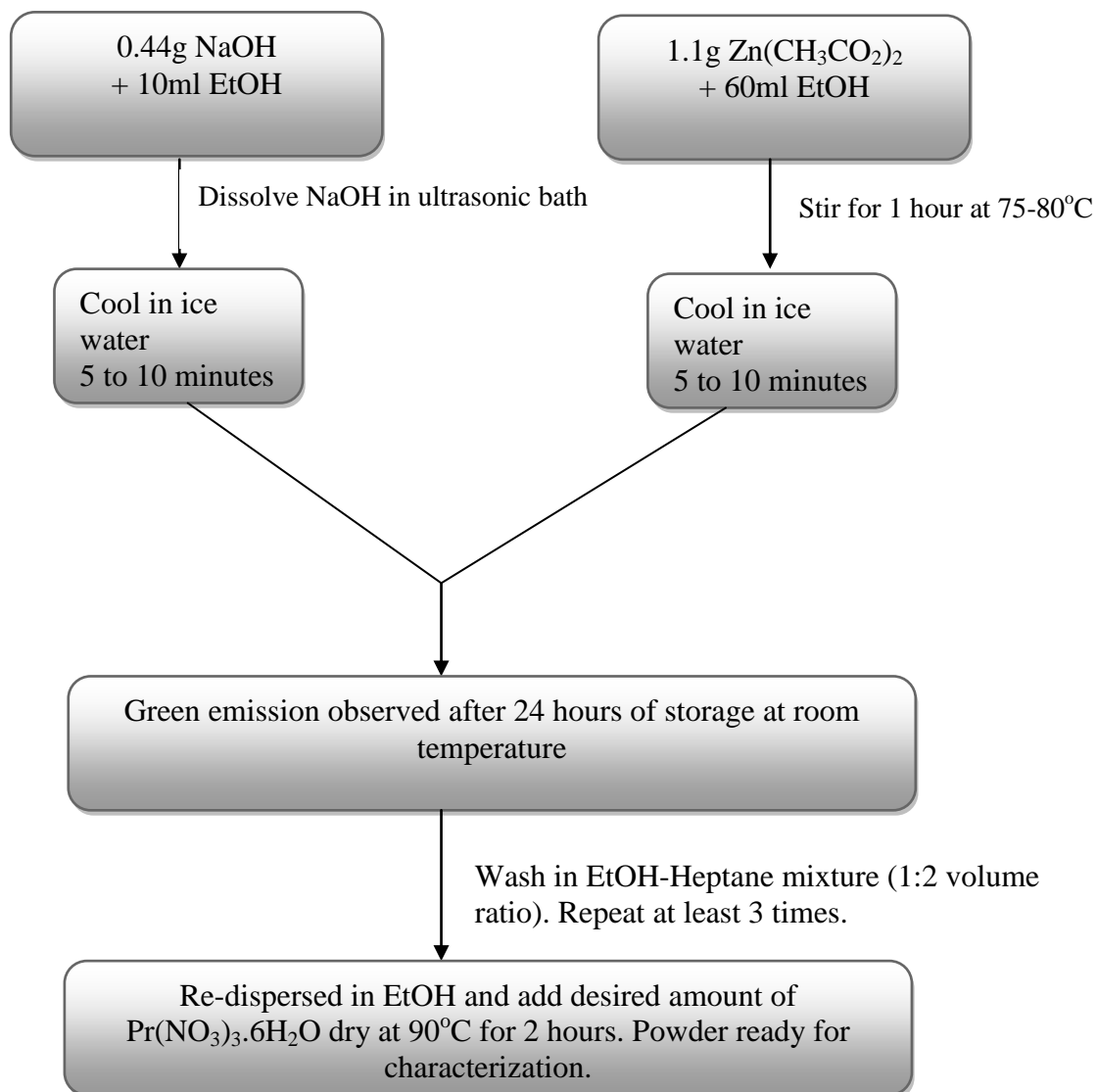$$Zn(CH_3COO)_2 + Na_2S \rightarrow ZnS + 2CH3COO^- + 2Na^+ \tag{4.3}$$


```
┌─────────────────────────┐          ┌─────────────────────────┐
│ 0.91g Na₂S dissolved in │          │    2g Zn(CH₃CO₂)₂       │
│   1:1 volume EtOH and   │          │      + 60ml EtOH        │
│     deionized H₂O       │          │                         │
└─────────────────────────┘          └─────────────────────────┘
```

Dissolve in ultrasonic bath   Stir for 1 hour at 75-80°C

Add Na$_2$S solution dropwise to ZnAc solution while vigorously stirring. White precipitate forms.

Wash in EtOH-Heptane mixture (1:2 volume ratio). Repeat at least 3 times

Re-disperse in EtOH and add desired amount of Pr(NO$_3$)$_3$.6H$_2$O. dry at 90°C for 2 hours. Powder ready for characterization.

Figure 4.8: Flow chart diagram of ZnS:Pr3$^+$ powder phosphor synthesis

4.6 Preparation of ZnO:Pr³⁺ phosphor

ZnO:Pr^{3+} nanoparticle phosphor was prepared by dissolving 2 g of zinc acetate (Zn (CH$_3$COO)$_2$.2H$_2$O) in 60 ml of ethanol using vigorous stirring at 75-80°C for 1 hour. The resulting transparent solution was cooled in ice water. Then 0.44 g of NaOH was dissolved in 10 ml of EtOH in an ultrasonic bath and was also cooled in ice water. This solution was slowly added to the transparent Zn-solution using vigorous stirring in ice water. The unwanted CH3COO$^-$ and Na$^+$ ions were removed by washing the precipitate repeatedly in a mixture of ethanol and heptane (volume ratio 1:2). The ZnO nanoparticles where dispersed in ethanol and desired amount of Pr(NO$_3$)$_3$.6H$_2$O was added. Different molar concentrations of Pr^{3+}were used. The precipitates were dried at 90°C for 2 hours and then annealed in air at 600°C for 2 hours. Figure 4.9 shows the flow chart diagram for the preparation and the equation for the formation of ZnO is shown in Equation 4.4:

$$Zn(CH_3COO)_2 \; + \; 2NaOH \; \rightarrow \; ZnO \; + \; 2CH3COO^- \; + \; 2Na^+ \; + \; H_2O(\uparrow) \qquad (4.4)$$

```
┌─────────────────────┐                    ┌─────────────────────────┐
│  0.44g NaOH         │                    │  1.1g Zn(CH₃CO₂)₂       │
│  + 10ml EtOH        │                    │  + 60ml EtOH            │
└─────────────────────┘                    └─────────────────────────┘
```

0.44g NaOH + 10ml EtOH

1.1g $Zn(CH_3CO_2)_2$ + 60ml EtOH

Dissolve NaOH in ultrasonic bath

Stir for 1 hour at 75-80°C

Cool in ice water 5 to 10 minutes

Cool in ice water 5 to 10 minutes

Green emission observed after 24 hours of storage at room temperature

Wash in EtOH-Heptane mixture (1:2 volume ratio). Repeat at least 3 times.

Re-dispersed in EtOH and add desired amount of $Pr(NO_3)_3.6H_2O$ dry at 90°C for 2 hours. Powder ready for characterization.

Figure 4.9: Flow chart diagram of ZnO:Pr3$^+$ powder phosphor synthesis.

References

[1] L.Sun, C.Qian, C.Liao, X. Wang,C. Yan, *Solid State Communications*,**119** (2001)

[2] L.L. Beecroft,C.K. Ober,*Journal of Material Chemistry*.,**9(6)** (1997)1312

[3] R. Tamaki, Y. Chujo, *Applied Organometallic Chemistry*.,**12** (1998)755

[4] Y. Zhang, J.M. Kim, D. Wu,Y.Sun, D.Zhao,S.Peng,*J.Non-Crystalline Solids* **351** (2005)777

[5] L.L Hench, J.K West, *Chemical Reviews*.,**90** (1990) 33.

[6] L.C Klein, *Annual Review of Materials Science*,**15** (1985)227

[7] P. Aragon-Santamaria, M.J. Santos-Delgado, A. Maceira-Vidan, L.M. Polo-Diez, *Journal of Materials Chemistry*.,**1(3)** (1991) 409

[8] A.C. Pierre, *Introduction to Sol-Gel processing*, Kluwer Academic Publishers, Boston,1998

[9] S. Criston, L. Armelao, E. Tondello,P. Traldi, *Journal of Mass Spectrometry* **34**(1999)1380.

[10] N. Yamanda, I. Yoshinaga, S. Katayama, *Journal of Sol-Gel Science and Technology*, **13** (1998) 445

[11] M.J Fernee, E. Thomsen, P. Jensen, H. Rubinsztein-Dunlop, *Nanotechnology*, **17** (2006)956

[12] K. Maurtz, Sol-gel chemistry, http://www.psrc.usm.edu/maurtz/sol-gel.html [23 October 2009]

Chapter 5

Properties of praseodymium (Pr^{3+}) doped zirconium oxide (ZrO_2)

5.1 Introduction

In recent years, considerable research has been done on the synthesis of advanced ceramic materials such as zirconium oxide (ZrO_2) using the sol-gel technique. Zirconium oxide ZrO_2 has beneficial ceramic properties such as chemical resistance, thermal stability, high mechanical toughness and high-temperature ionic conductivity [1,2]. In r2ecent studies, it is commonly used as host matrix for rare-earth ions to prepare phosphor materials for use in different light emitting devices. This work reports on the structure, morphology, chemical composition and the photoluminescence characteristics of Pr^{3+}-doped ZrO_2 prepared by the sol-gel method. The influence of the annealing temperature on the structure and the effects of doping on the photoluminescence intensity were investigated.

5.2 Experimental

The preparation of ZrO_2 and ZrO_2:Pr^{3+} nanophosphors was discussed in Chapter 4, Section 4.4. The XRD, SEM and EDS were used, respectively, to analyze the structure, morphology and chemical composition; and a UV-Vis spectrophotometer with a 325nm He-Cd laser were used to determine the luminescence properties of the samples in air at room temperature.

5.3 Results and Discussion

Figures 5.1 and 5.2 show the XRD patterns of ZrO_2 powders annealed at 280^oC and 600^oC respectively. The two figures show the effect of the annealing temperature on the structure and emission wavelengths of $ZrO_2:Pr^{3+}$ (Figure 5.1), the XRD patterns of the powders annealed at 280^oC were amorphous with two broad peaks at 2θ ~30 and 50 degree. When the powders were annealed at 600^oC, Figure 5.2, these broad peaks became sharper, demonstrating the evolution of a crystalline phase, similar to the tetragonal form of zirconia, Z(t). Aguilar *et al* [1] demonstrated that continued heating at high temperature transformed Z(t) to pure monoclinic Z(m).
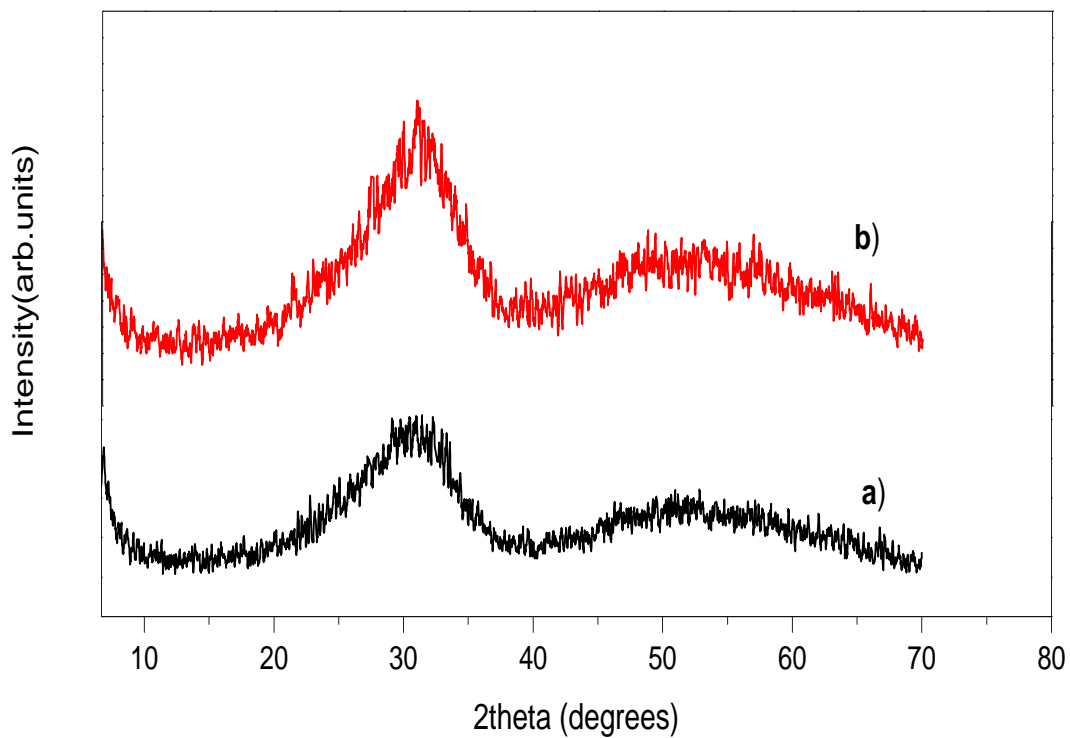
Figure 5.1: XRD Patterns of (a) Pure ZrO_2 , (b) $ZrO_2:Pr^{3+}$ nanophosphors ($T_a = 280^oC$)
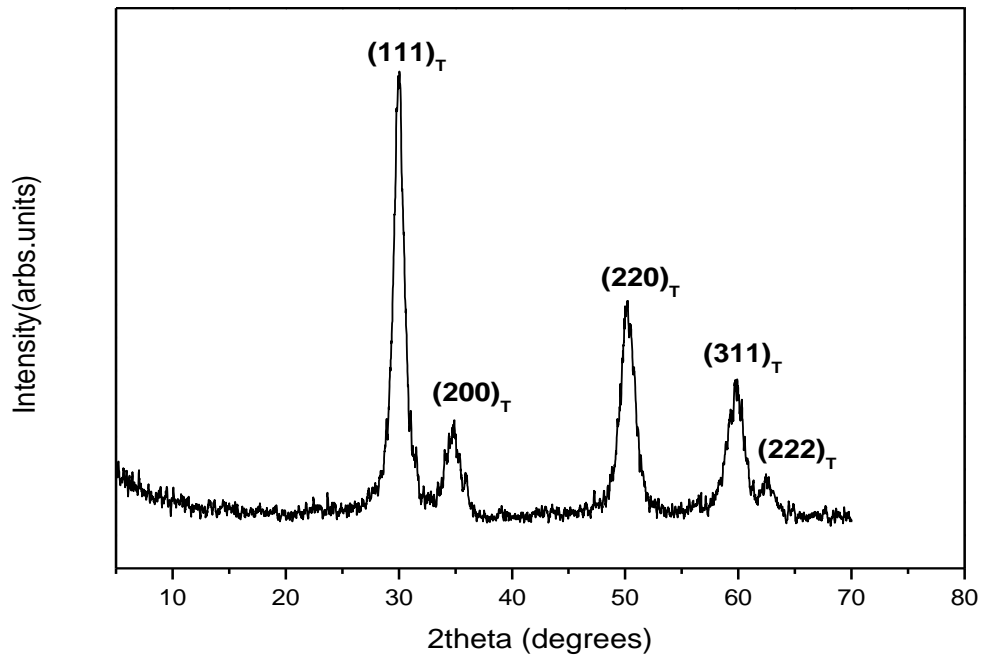
Figure 5.2: XRD Patterns of $ZrO_2:Pr^{3+}$ nanophosphor ($T_a=600^oC$)

Five diffraction peaks identified as (111), (200), (220), (311) and (222) which correspond to the tetragonal phase of zirconia were observed in the XRD patterns of Figure 5.2. The tetragonal phase can stabilize within the nanodomains of different sizes depending on the processing conditions. The particle sizes were estimated using the Debye-Scherrer equation [3]:

$$d = \frac{0.9\,\lambda}{\beta\cos\theta},$$
(5.1)

where d is the mean particle size, λ is the wavelength of the x-rays (0.154nm), β is the full width at half maximum and θ is the angle in degrees of the corresponding diffraction peak. The width of the diffraction peak at (111) was used to estimate the particle size and the average particle sizes of the samples were estimated to be ~8 nm. Figure 5.3 shows the (a) low (35, 000 x) and (b) high (150, 000x) images of pure ZrO_2 powders. At low magnification, it appears as if the powders consist of spherical nano-sized particles. However, as confirmed at high magnification, the powders were made up of agglomerations of non-uniform nanoparticles with irregular shape. The particle morphology of Pr- doped ZrO_2 was similar to that of pure ZrO_2. Major elements present in this material were detected by EDS as shown in figure 5.4. The carbon (C) was due to the tape used for sample preparation.
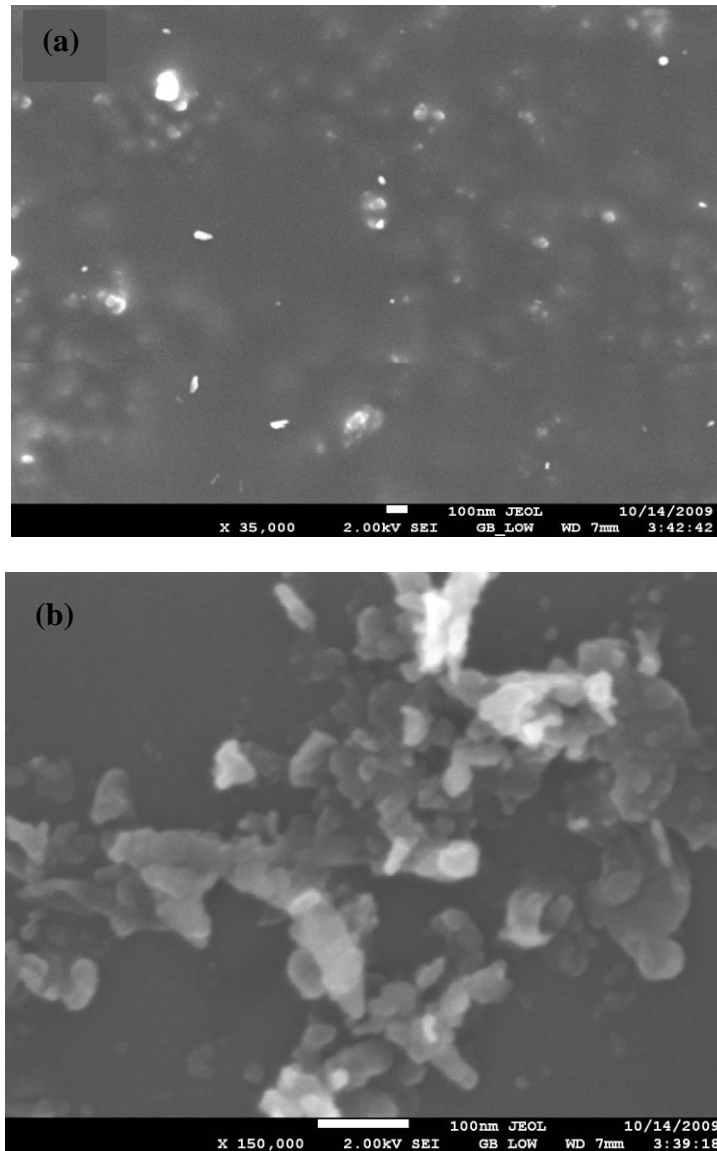
Figure 5.3: SEM images of ZrO_2 (a) 35,000x and (b) 150,000x magnification.(T_a=280°C)

The UV-Vis absorption spectra of (1) ZrO_2 and (2) ZrO_2:Pr^{3+} is shown in Figure 5.5. The spectrum for pure ZrO_2 shows a shoulder at 272 nm (4.5eV) corresponding to the band gap absorption of ZrO_2 nanoparticles which can arise due to direct recombination of conduction band electrons with the valence band holes. W.Z Li *et al* [4] reported a sharp and prominent absorption peak at around 292 nm (4.25eV). However, the absorption peak at 4.5 eV is at lower energy compared to literature value for bulk ZrO_2 (5.2 eV) [4]. The spectrum for ZrO_2:Pr^{3+} (2) shows that the 272 nm (4.57eV) absorption peak shifted to 326 nm (3.81 eV)

and additional peak was detected at 235 nm (5.29eV). Yang *et al* [5], reported a strong absorption peak at wavelength of about 197 nm and a relatively weaker peak at 275 nm for yttria-doped ZrO_2 nanoparticles. This indicates that there is contribution from the extrinsic states such as surface trap states or impurities. The shifting can be attributed to the changes in the quantum confinement of electrons [6]. The optical direct band gap energy, E_g, was determined from the plot of $(\alpha h\nu)^2$ vs photon energy $h\nu$ (Figure 5.5), where α is an absorption coefficient.
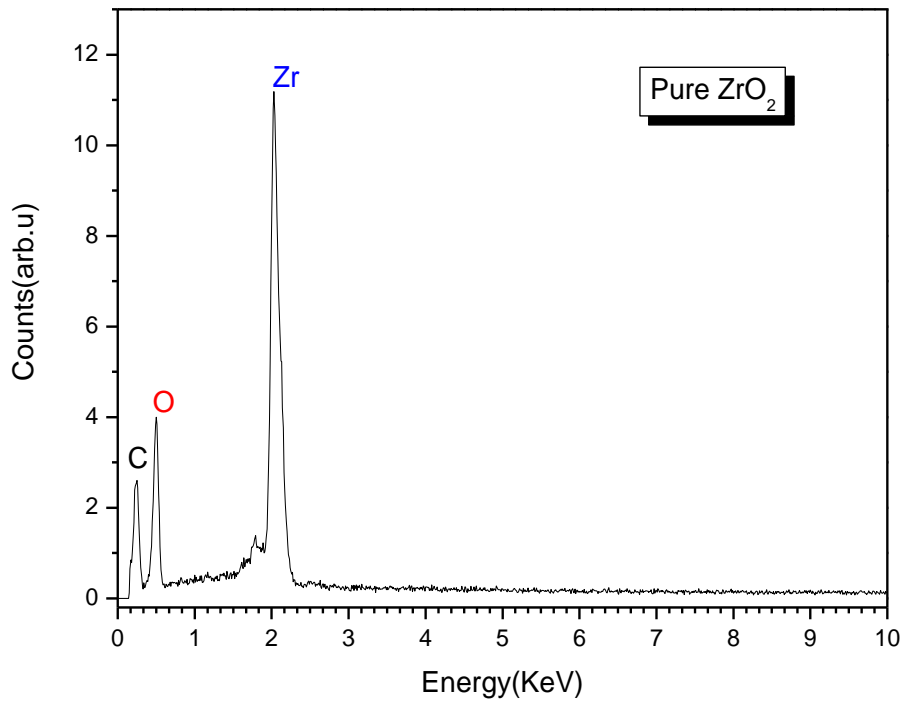
Figure 5.4: EDS spectrum of ZrO_2 nanophosphor (T_a=280°C).
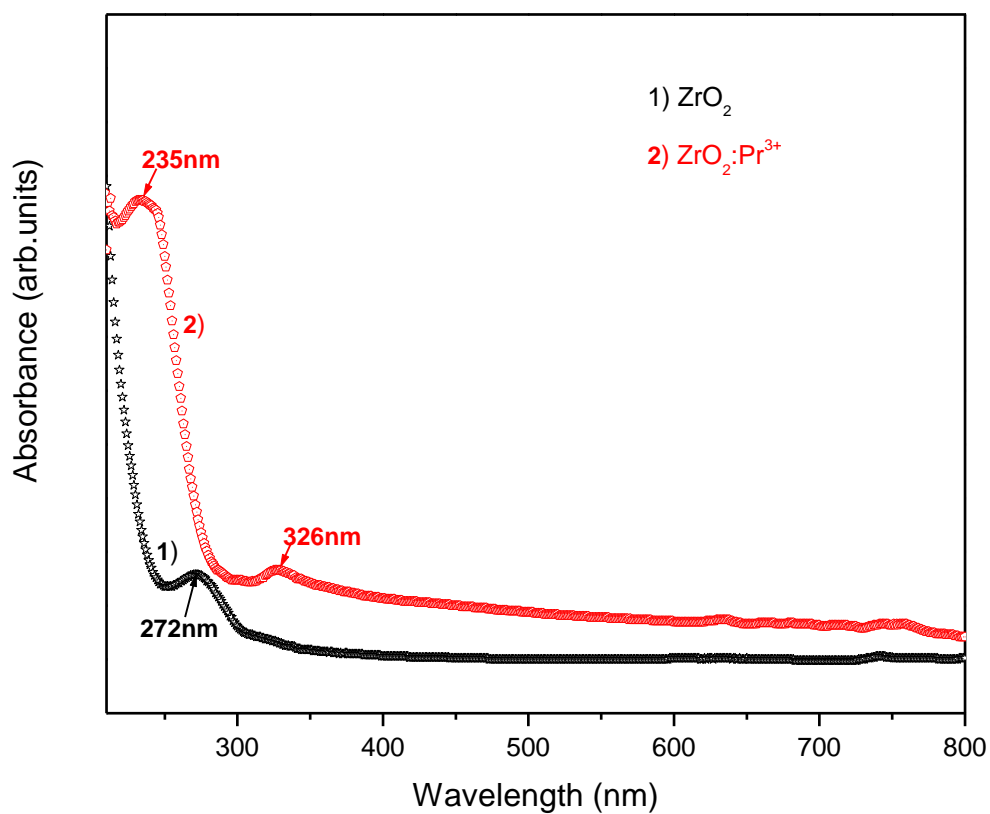
Figure 5.5: Optical absorption spectra of (1) ZrO_2 and (2) ZrO_2:Pr^{3+} nanophosphor ($T_a=280^oC$).
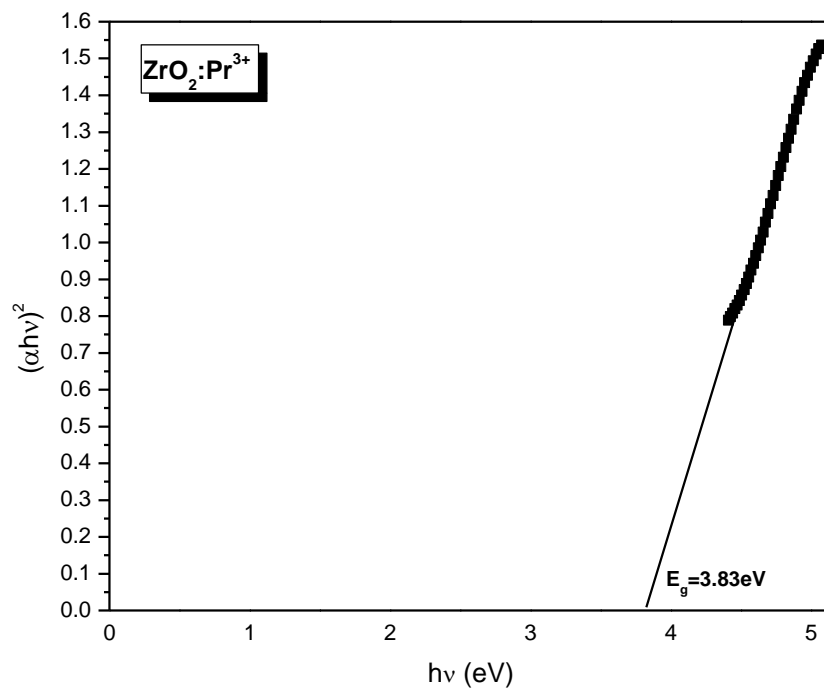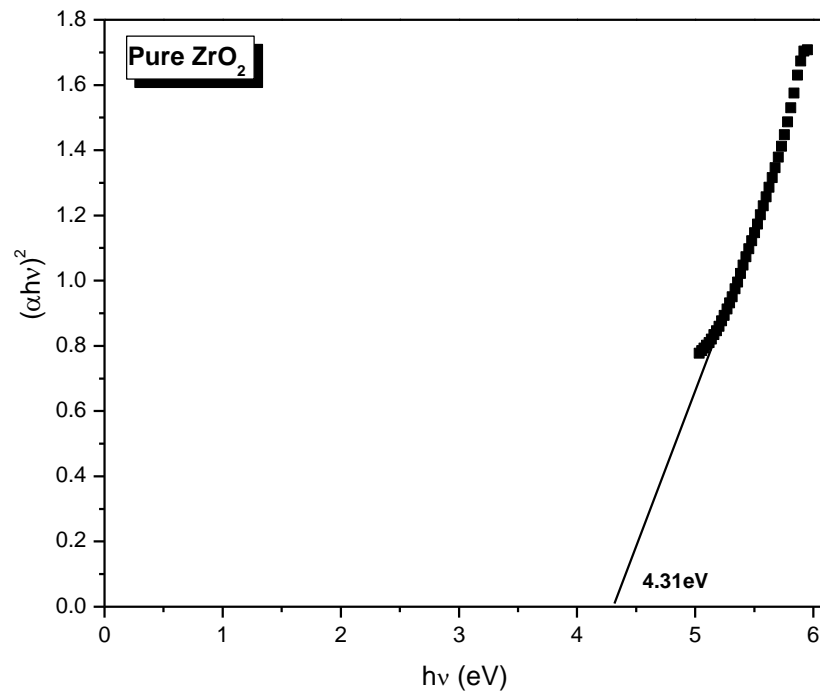
Figure 5.6: $(\alpha h\nu)^2$ vs photon energy ($h\nu$) plot of ZrO_2 and ZrO_2:Pr^{3+} nanoparticles (dried at $90^{o}C$).

The photoluminescence emission spectra of ZrO_2 and ZrO_2:Pr^{3+} amorphous nanopowders annealed at 280^oC are shown in Figure 5.7. The powders were excited using the 325 nm He-Cd laser in air at room temperature. The PL spectra of pure ZrO_2 and Pr^{3+}-doped ZrO_2 are the same with two emission peaks centered around 459 nm and 554 nm. The emissions at 459 and 554 nm can be attributed to near band-edge transitions and mid-gap trap states of ZrO_2, respectively [7]. The emission at 459 nm was quenched when Pr^{3+} was introduced with a subsequent slight red shift and broadening of the 554 nm peak. The broadening of the 554 nm peak is due to the increasing of the particle size of the nanophosphors [9]. Luminescence quenching is also observed as the concentration of the dopant was increased and can also be associated with the Pr^{3+}-O bond distance, the shorter the bond length, the higher the luminescence intensity [8]. The was no emission observed for ZrO_2:Pr^{3+} annealed at 600^oC.
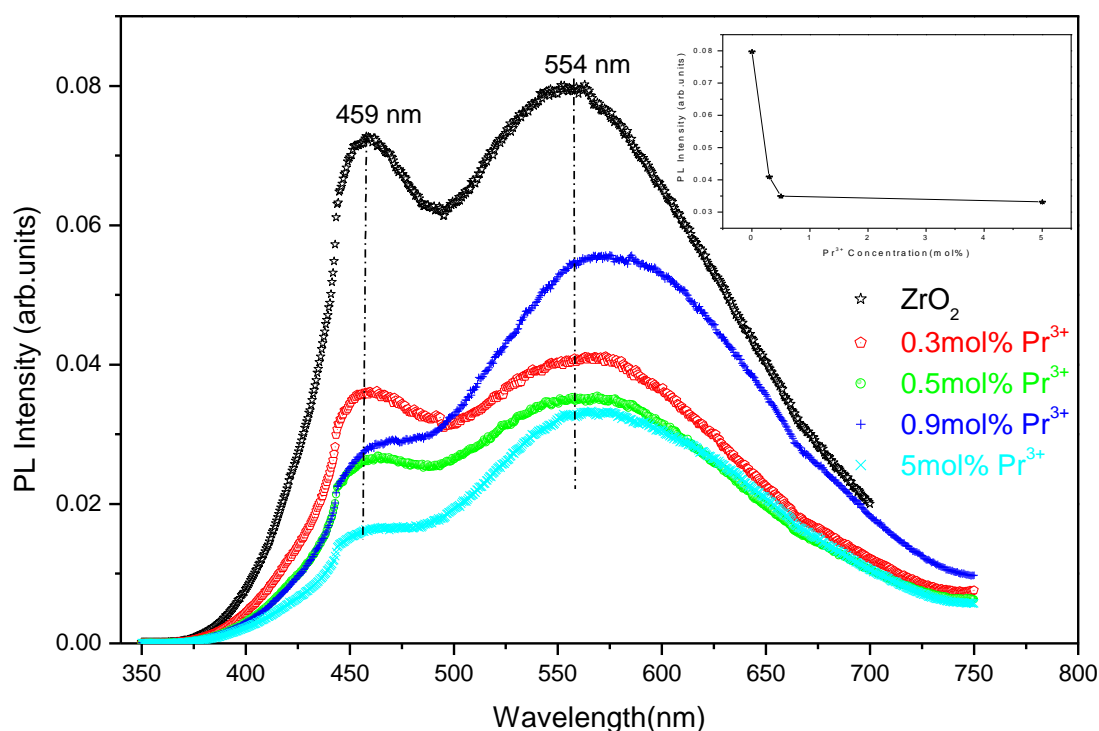
Figure 5.7: PL emission spectra of ZrO_2 and $ZrO2$:Pr^{3+} ($T_a = 280^oC$) excited at 325 nm.

The maximum PL intensity of the 554 nm peak as a function of Pr^{3+} concentration is shown in the insert of Figure 5.7. The emission intensity as a function of a relative doping concentration shows a decreasing curve indicating a luminescence quenching. This may be due the formation of impurity clusters which can act as killers of the luminescence.

5.4 Conclusion

ZrO_2 and ZrO_2:Pr^{3+} nanophosphors were successfully synthesized by the sol-gel method. The XRD data showed that ZrO_2 annealed at $280^{o}C$ was amorphous and it crystallized when the annealing temperature was increased to $600^{o}C$. SEM images showed agglomerated particles with irregular shapes and the elements were detected by EDS. The PL emission showed two emission peaks centered around 459 nm and 554 nm suggesting that emitted light came from the host matrix (ZrO_2). Luminescence quenching was observed with an increase of the dopant concentration and this may be due to increased killer centers.

References

[1] D.H. Aguilar, L.C. Torres-Gonzalez and L.M Torres-Martinez, *Journal of Solid State Chemistry*, **158** (2000) 349-357

[2] F. Ramos-Brito, M Garcia-Hipolito, C Alejo-Armenta, O. Alvarez-Fragoso and C Falcony, *Journal of Physics D:Applied Physics.* **40** (2007) 6718-6724

[3] K.S Rathore, D Patidar, Y. Janu, N.S Saxena, K. Sharma and T.P Sharma, *Chalcogenide Letters* **5** (2008) 105-110

[4] W.Z. Li, L. Kumari, G.H Du, R.S Vennila, S.K Saxena and D.Z Wang, *Ceramics international* **35** (2009) 2401-2408

[5] H. Yang, J. Ouyang, X. Zhang, N.Wang and C. Du, *Journal of Alloys and Compounds* **458** (2008) 474-478

[6] O.M Ntwaeaborwa, R.E Kroon, V. Kumar, T. Dubroca, J.P Ahn, J.K Park and H.C Swart, *Journal of physics and chemistry of solids* **70** (2009) 1438-1442

[7] Y. Li, J. Liang, X. Jiang, G. Liu, Z. Deng, J. Zhuang and F. Li, *Materials Research Bulletin* **38** (2003) 161-168

[8] Y. Li, L. Chen and Y. Liu, *Journal of Alloys and Compounds* **381** (2004) 266-271

[9] M.S Dhlamini, PhD Dissertation, University of the Free State, 2008.

Chapter 6

Properties of praseodymium (Pr^{3+}) doped silicon dioxide (SiO$_2$)

6.1 Introduction

Sol-gel derived silicon dioxide (SiO$_2$) doped with rare-earth ions is an important optical material in applications such as solid-state lasers and optical waveguides [1]. An attractive feature of sol-gel derived SiO$_2$ is that it can hold a higher concentration of dopants than traditional melt glasses without losing its amorphous character [2]. Studies of the optical behaviour of such materials provide information about the interactions between the dopant and the surrounding matrix and energy transfer [2]. This chapter reports on the structure, morphology, chemical composition, photoluminescence and cathodoluminescence properties of praseodymium-doped SiO$_2$ prepared by the sol-gel method.

6.2 Experimental

The preparation of SiO$_2$ and SiO$_2$:Pr^{3+} nanophosphors was discussed in Chapter 4, Section 4.3. The XRD, SEM and EDS were used, to analyze the structure, morphology and chemical composition, respectively. UV-visible spectrophotometer, with a 325 nm He-Cd laser and CL spectroscopy were used to determine the luminescence properties of the samples at room temperature.

6.3 Results and Discussion

The XRD patterns of SiO_2 and $SiO_2:Pr^{3+}$ annealed at 600^oC for two hours, are shown in Figure 6.1. The broad amorphous band from SiO_2 was observed at $2\Theta\sim22.8$ degrees. Pr^{3+} activator ions did not contribute to any diffraction peaks suggesting that the ions were well dispersed in the silica matrix and this was also because of their relatively low concentration.
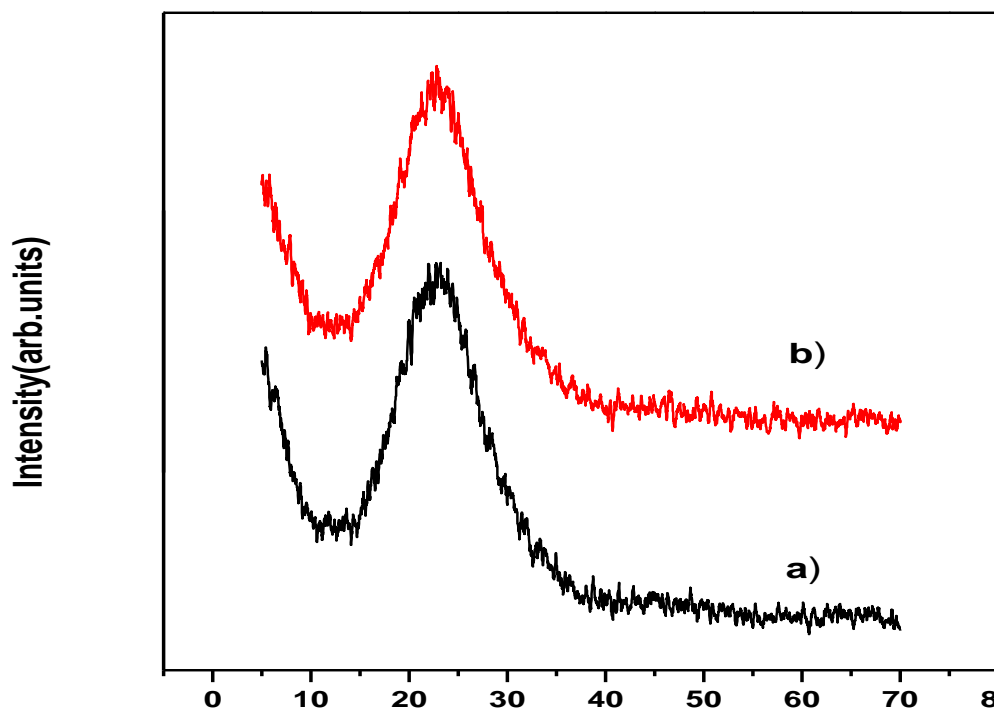

Figure 6.1: XRD patterns of (a) Pure SiO_2 and (b) SiO2:Pr^{3+} nanophosphors ($T_a=600^oC$)

Figure 6.2 shows the SEM images and Figure 6.3 shows EDS spectrum of $SiO_2:Pr^{3+}$. The low and high magnification SEM images of annealed $SiO_2:Pr^{3+}$ powders are shown in the Figures 6.2 (a) and (b) respectively. It can be inferred from both images that the powders consists of an agglomeration of spherically shaped nanoparticles with an estimated average particle size of 20 nm in diameter. The major chemical elements, Si and O, were confirmed by the EDS spectrum shown in Figure 6.3. Pr^{3+} ions were not detected probably due to their relatively low concentration.
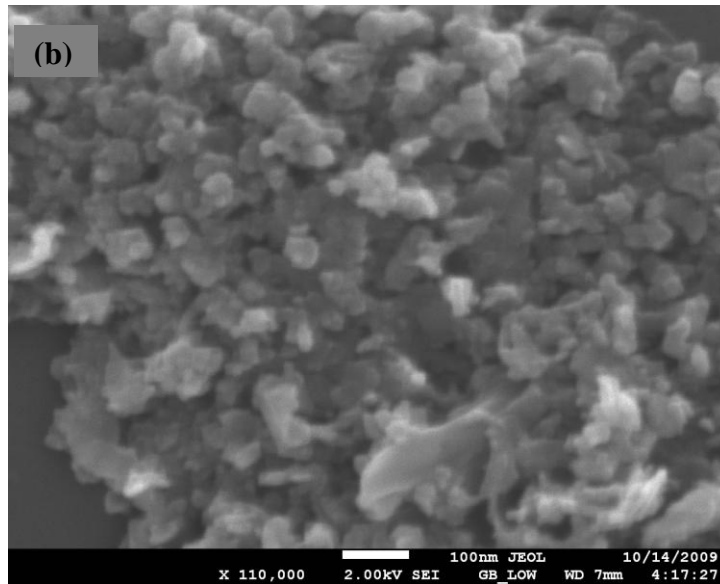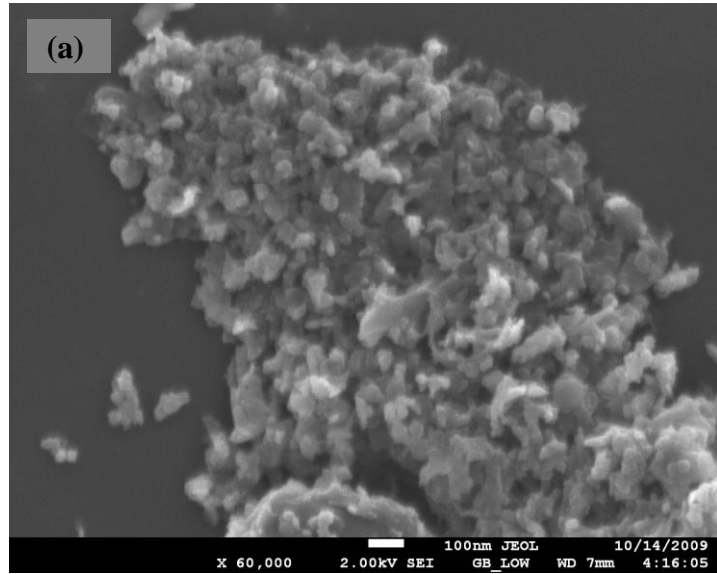
Figure 6.2: SEM images of SiO_2 :Pr^{3+}(a) 60, 000x and (b) 110, 000x magnification $(T_a=600^oC)$.
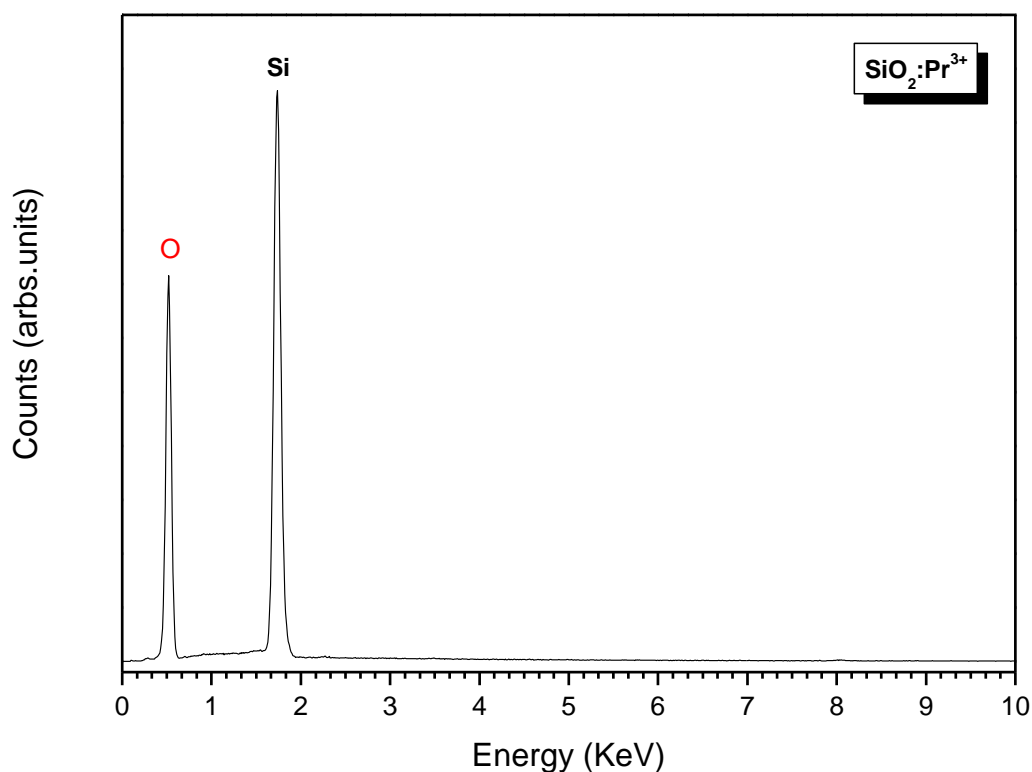
Figure 6.3: EDS spectrum of SiO_2 nanophosphor (T_a=600°C).

Figure 6.4 shows the absorption spectra of pure and Pr-doped silica in the visible region. There was no absorption band observed for pure and Pr-doped SiO_2 due to the reason that the bandgap energy of SiO_2 (9 eV) is too large for the energy source of Uv-Vis spectrophotometer used in this study which has the radiation source of Tungsten filament (300-2500 nm) and Deuterium arc lamp (190-400 nm).
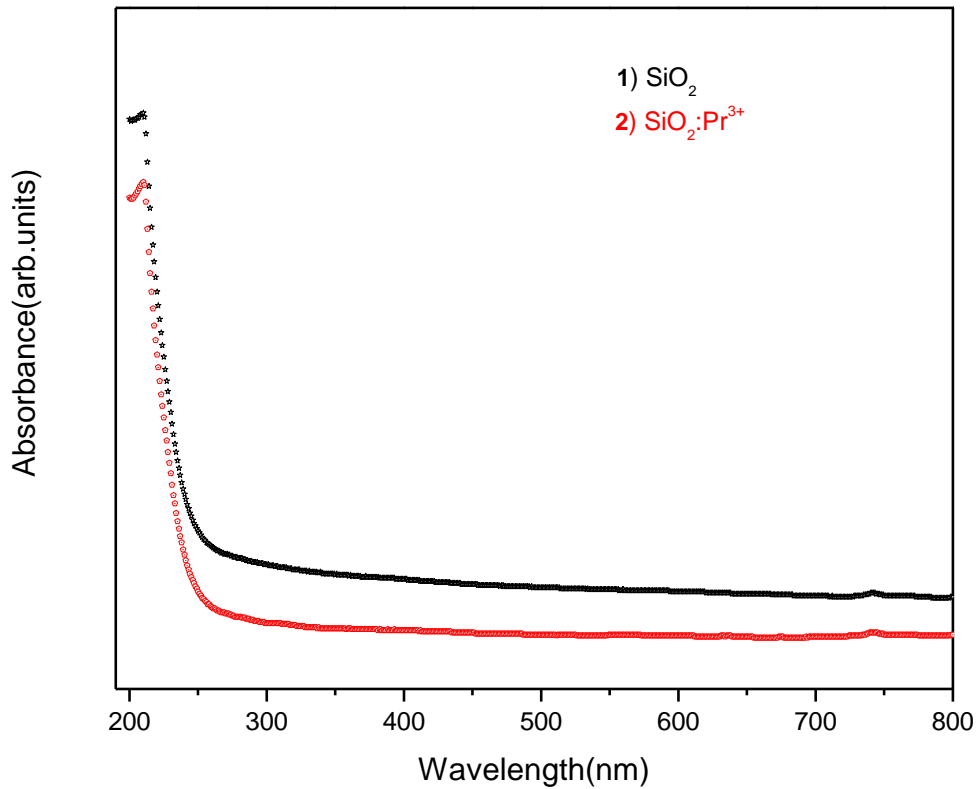
Figure 6.4: Optical absorption spectra of (1) SiO_2 and (2) $SiO_2:Pr^{3+}$ nanophosphors.($T_a = 600^oC$) .

PL emission spectra of SiO_2 and $SiO_2:Pr^{3+}$ nanophosphors are shown in Figure 6.5. A broad emission peak, with a maximum at 498 nm and a shoulder at 416 nm were observed from the pure SiO_2 spectrum. Visible emission from sol-gel derived SiO_2 with major emission peaks located at ~425 nm and a minor emission peak at ~520 nm was reported previously [4]. The origin of the luminescence in sol-gel derived silica has not been well established yet [5]. Three possible mechanisms, i.e. defect, charge transfer and carbon impurity mechanism have been proposed to explain the luminescent phenomena in silica and these mechanisms were briefly explained by J. Lin *et al* [5]. The widely accepted luminescence mechanism is by structural defects in the SiO_2 network or charge transfer between O and Si atoms [4].
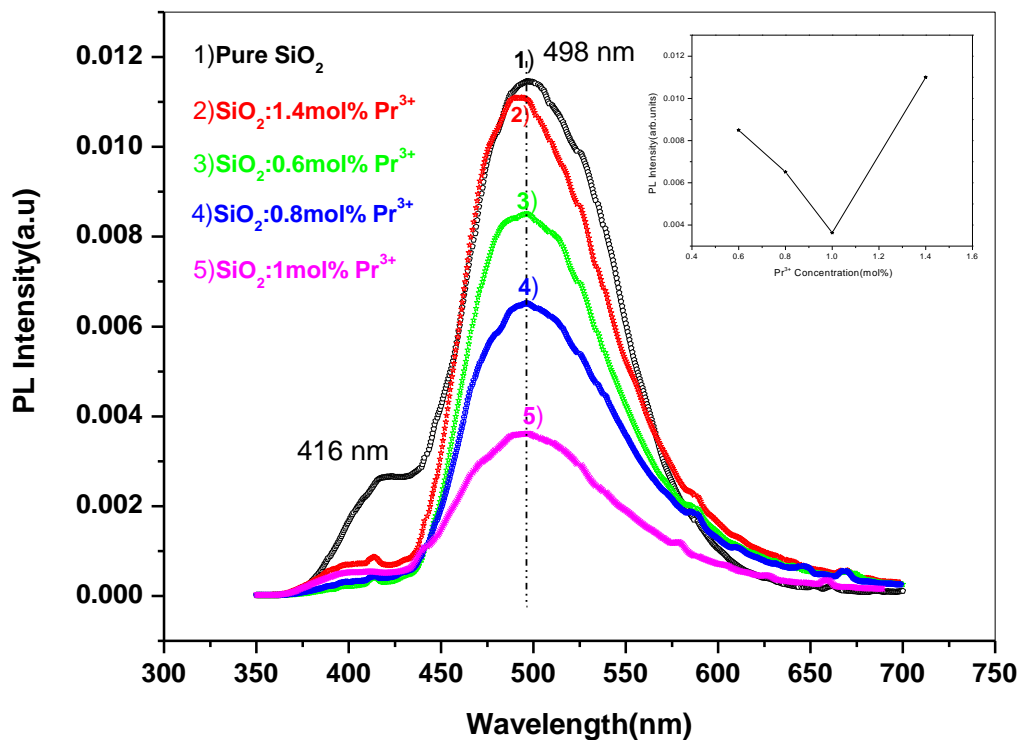
Figure 6.5: PL emission spectra of SiO_2 and $SiO_2:Pr^{3+}$ ($T_a=600^oC$) excited at 325 nm.

When different molar concentrations of Pr^{3+} ions were incorporated the PL intensity decreased successively for 0.6-1 mol% of Pr^{3+}doping and it increased when the concentration was increased to 1.4 mol%. The decrease or quenching of luminescence can be explained by the residual hydroxyl groups in the glass network. Because of the presence of water in the starting sol and water generated during condensation reaction there is an abundance of OH^- in the material [6]. An OH^- group can associate with a rare-earth ion, providing a non-radiative de-excitation channel for the excited ion that lowers the luminescence yield [6]. The insert shows the behavior of emission intensity as a function of Pr^{3+} concentration.

Figure 6.6 shows the CL emission spectra of SiO_2 and $SiO_2:Pr^{3+}$ irradiated with a 2 keV electron beam in a vacuum chamber maintained at the base pressure of $1x10^{-9}$ torr. SiO_2 showed emission peak with a maximum intensity at 451 nm which was consistent with the 416 nm peak (in figure 6.5) and a shoulder at 478 nm. The peak at 498 nm was not detected in CL spectra possibly due to difference in photon and electron excitation energy and/or penetration depth [7]. The difference in emission between photo-excitation and electro-

excitation may also be attributed to the nature of the excitation source. That is, the main paths for recombination are also different for different excitation mechanism [7]. $SiO_2:Pr^{3+}$ showed a multiple peak emission located at 510 nm, 614 nm, 730 nm, 780 nm and 970 nm which can be associated with $^3P_0\rightarrow^3H_4$, $^1D_2\rightarrow^3H_4$, $^1D_2\rightarrow^3H_5$, $^3P_0\rightarrow^3F_{3,4}$ and $^1G_4\rightarrow^3H_4$ transitions in the Pr^{3+} ion, respectively [8,9,10,11]. The maximum emission intensity was detected at 614 nm, which was not observed from the photon excitation data. Again, this may be attributed to difference in the photon versus electron excitation energy and possibly penetration depth. The fact that defects emission from SiO_2 was completely quenched suggests that at higher excitation energy (2 keV electrons versus 3.8 eV (325 nm) photons) SiO_2 acts to harvest energy and transfer to Pr^{3+} resulting in red cathodoluminescence emission maximized at 614 nm. It is also possible that this emission was due to direct excitation of Pr^{3+} and energy transfer to the neighboring Pr^{3+} ions as illustrated schematically in Figure 6.7.
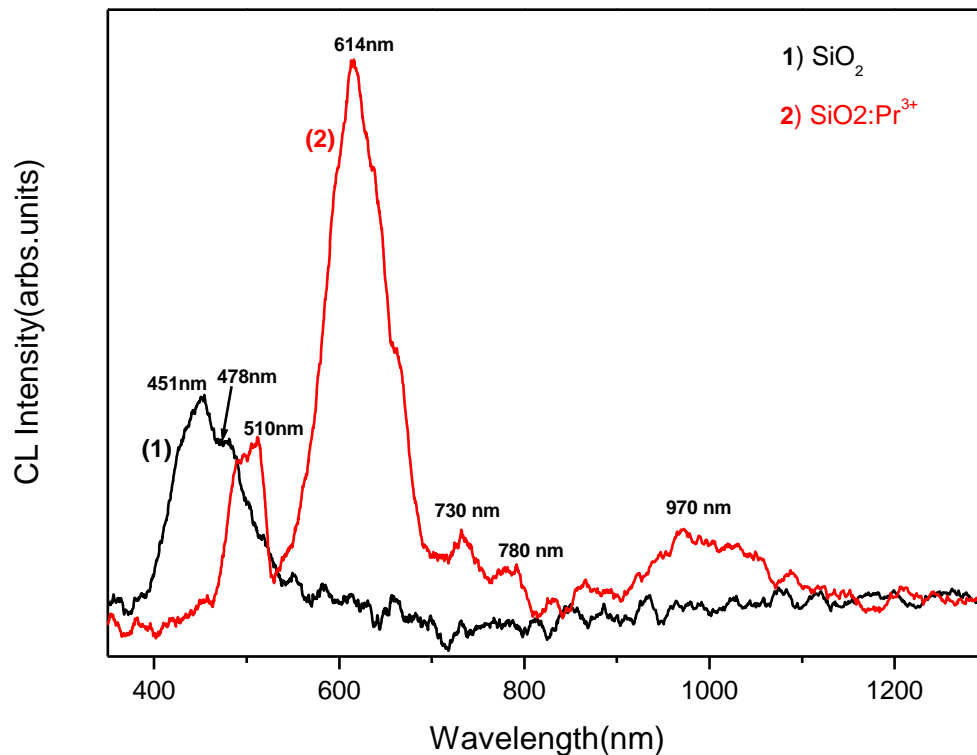

Figure 6.6: CL emission spectra of (1) SiO_2 and (2) $SiO_2:Pr^{3+}$ powder phosphor ($T_a=600^oC$) irradiated with 2 keV electron beam.
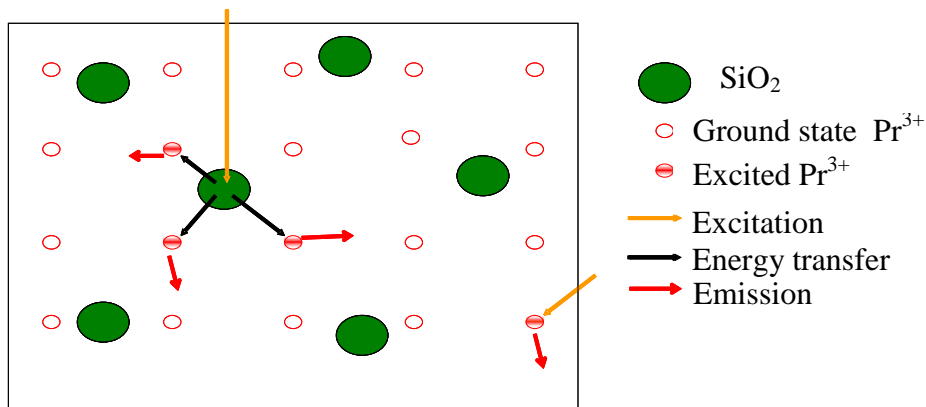
Figure 6.7: Excitation of SiO_2 or Pr^{3+} ion and energy transfer to neighboring Pr^{3+} ions resulting in red emission [12].

6.4 Conclusion

Sol-gel derived SiO_2 and SiO_2:Pr^{3+} nanopowders were successfully synthesized and were shown to be amorphous even after annealing at 600^oC for two hours. The major chemical elements were confirmed by EDS. A broad PL emission peak centered around 498 nm was observed from both pure and Pr^{3+} - doped SiO_2. The effect of the concentration of the Pr^{3+} ions on the PL intensity was demonstrated. CL showed a multiple peak emission resulting from the transitions in the Pr^{3+} ion with major emission at 614 nm.

References

[1] H. Bi, W. Cai and L. Zhang, *Materials Research Bulletin* **35** (2000) 1495-1501

[2] A.J. Silversmith, D.M. Boye, K.S. Brewer, C.E. Gillespie, Y. Lu and D.L. Campbell, *Journal of Luminescence* **121** (2006) 14-20

[3] O.M Ntwaeaborwa, R.E Kroon, V. Kumar, T. Dubroca, J.P Ahn, J.K Park and H.C Swart, *Journal of Physics and Chemistry of Solids* **70** (2009) 1438-1442

[4] O.M Ntwaeaborwa, PhD Dissertation, University of the Free State, 2006.

[5] J. Lin, Y. Han and H. Zhang, *Materials Letters* **54** (2002) 389-396

[6] A.J. Silversmith, D.M. Boye, K.S. Brewer, C.E. Gillespie, Y. Lu and D.L. Campbell, *Journal of Luminescence* 121 (2006) 14-20

[7] H.K. Yueh and B.Cox, *Journal of Nuclear Materials* **323** (2003) 57-67

[8] W. Strek, J. Legendziewicz, E. Lukowiak, K. Maruszewski, J. Sokolnicki, A.A Boiko and M. Borzechowska , *Spectrochimica Acta Part A* **54** (1998) 2215-2221

[9] C. DE Mello Donega, A. Meijerink and G. Blasse, *Journal of Physics and Chemistry of Solids* **0022-3697**(1995) 00183-9

[10] P. Boutinaud, E. Pinel, M. Dubois, A.P Vink and R. Mahiou, *Journal of Luminescence* **111**(2005) 69-80

[11] P.N Zhmurin, N.V Znamenskii, T.G. Yukina and Yu.V. Malyukin, *Physica Status Solidi* **224** (2007) 3325-3332

[12] Bang J.; Yang Y.; Holloway P.H. *Journal of Chemical Physics* **123** (2005) 123, 1-5.

Chapter 7

Cathodoluminescence degradation of SiO$_2$:Pr^{3+} powder phosphor

7.1 Introduction

This chapter presents cathodoluminescence degradation (CL) data from SiO$_2$:Pr^{3+} powder phosphor prepared by a sol-gel process. The powder was degraded in ultra high vacuum chamber and the CL intensity as a function of electron dose and the surface chemical changes were recorded. The surface reactions and degraded luminescence intensity resulting from the electron bombardment were monitored using Auger electron spectroscopy (AES) and CL spectroscopy. This phosphor was evaluated for possible application in flat panel information displays such as field emission and flat panel plasma displays.

7.2 Experimental

The AES and CL measurements were carried out in an ultra high vacuum (UHV) chamber at the base pressure of 1x10^{-9} torr with a PHI model 549 system. The powder was irradiated with a beam of electrons with energy of 2 keV and a beam current density of 23.4 µA in UHV chamber. AES and CL spectroscopy were used to monitor the degradation of the surface and the decrease of CL intensity. The AES and CL spectroscopy data were collected simultaneously. Residual Gas Analysis (RGA) was performed using the anavac-2 mass analyzer to determine the volatile gas species during electron bombardment.

7.3 Results and Discussions

The AES spectra of SiO$_2$:Pr^{3+} powder phosphor before and after degradation with characteristic Auger peaks of Si and O at 79 eV and 504 eV, respectively, are shown in figure 7.1(a). Compared to the normal peak from elemental Si at ~92 eV, the Si Auger peak from SiO$_2$ is known to be at ~70-80 eV [1]. The shift from high energy (~92 eV) in Si element to

low energy (~70-80 eV) in the compound SiO_2 has been attributed to the change in the density of states in the valence band and relaxation effects [2,3]. The absence of C peak (usually at 273 eV) suggests that there was less contamination from hydrocarbons in the UHV chamber. With continuous electron bombardment of $SiO_2:Pr^{3+}$ surface AES spectrum after degradation showed the development of extra peaks at 106 and 123 eV as shown in Figure 7.1(b). These peaks can be attributed to the elemental Pr according to the standard Auger spectra of the elements. This result suggests that Pr^{3+} ions were enclosed by SiO_2 and the ions were exposed as a result of prolonged exposure to 2 keV electrons. Also it has been reported that prolonged electron beam exposure reduces the peak intensity of Si in SiO_2 due to the development of the new peaks [4,5,6,7], instead, in this study the reduction of Si peak intensity was not observed but only development of extra peaks which can be attributed to Si in SiO_2.

Figure 7.2 shows the CL emission spectra of $SiO_2:Pr^{3+}$ (i) before and (ii) after degradation. The main emission peak due to $^1D_2 \rightarrow ^3H_4$ transition of Pr^{3+} ion was only 50% of the initial intensity after degradation, showing that an exposure to 2keV electrons significantly reduces the CL intensity. The change in intensity and Auger electron peak-to-peak heights (APPHs) from O (oxygen), Si (silicon), adventitious C (carbon) and the relative CL intensity as a function of electron dose are shown in Figure 7.3. There was a slight increase of Si concentration during the entire degradation duration while C and O concentration was stable for the entire electron beam exposure. The CL intensity was shown to decrease with continuous exposure to 2 keV electrons.
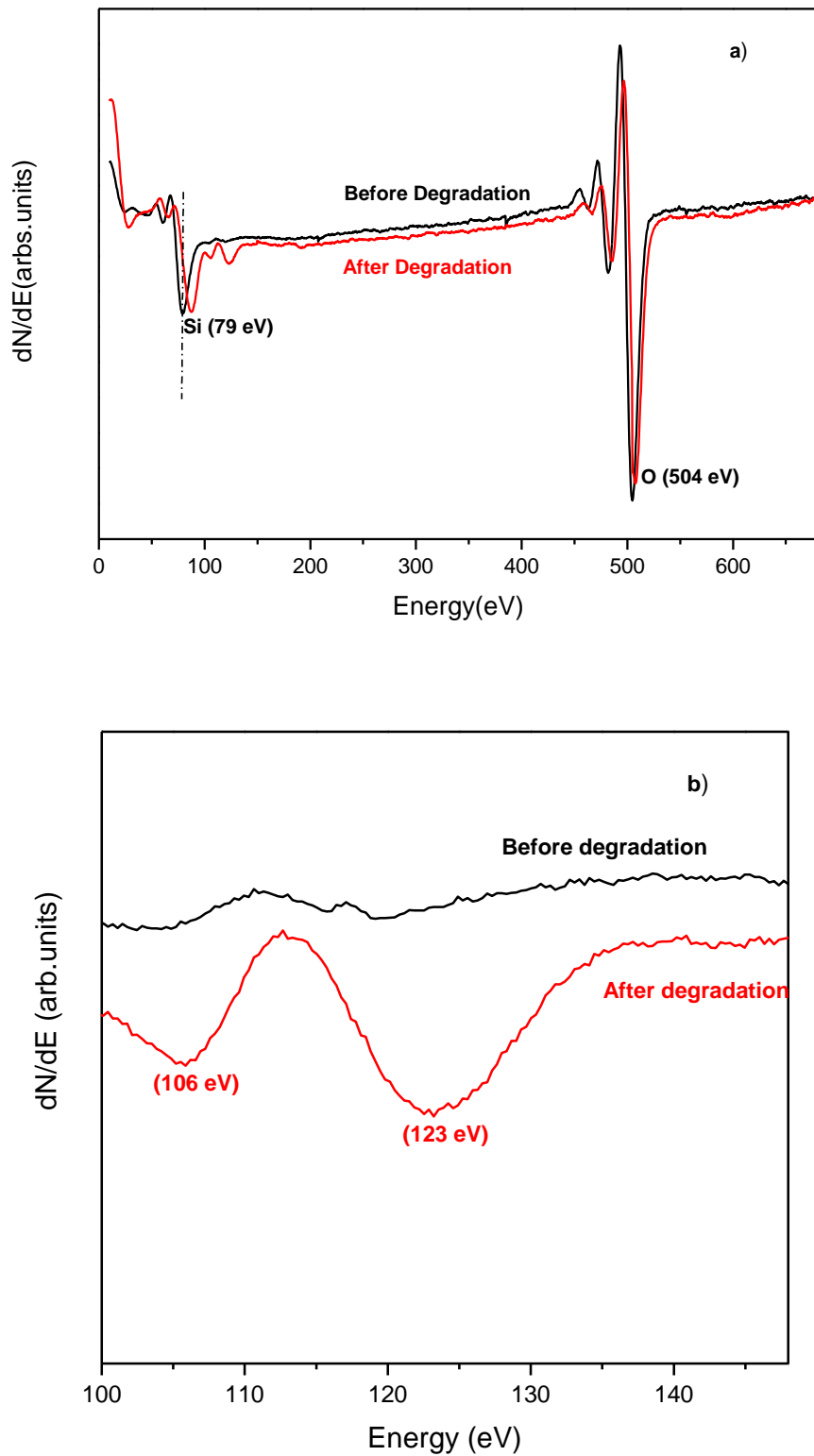
Figure 7.1: (a) AES spectra of $SiO_2:Pr^{3+}$ powder phosphor before and after degradation at a base pressure of 1×10^{-9} torr (b) Magnified AES spectrum in the 100-140 eV energy range showing development of extra peaks at 106 and 123 eV after degradation.

The increase in Si peak can be explained in terms of possible formation of Si compounds such as SiH_4, SiOH and SiC as result of chemical reactions between volatile H^+, OH^- and C species, respectively, and Si^{2+} ions. Although not confirmed in this study, the formation of these layers could contribute to the decrease of the CL intensity as widely explained by the electron stimulated surface chemical reaction (ESSCR) mechanism [1,8,9]. According to this mechanism, a non-luminescent layer can form on the surface as a result of a chemical reaction between volatile atomic species in the UHV chamber.
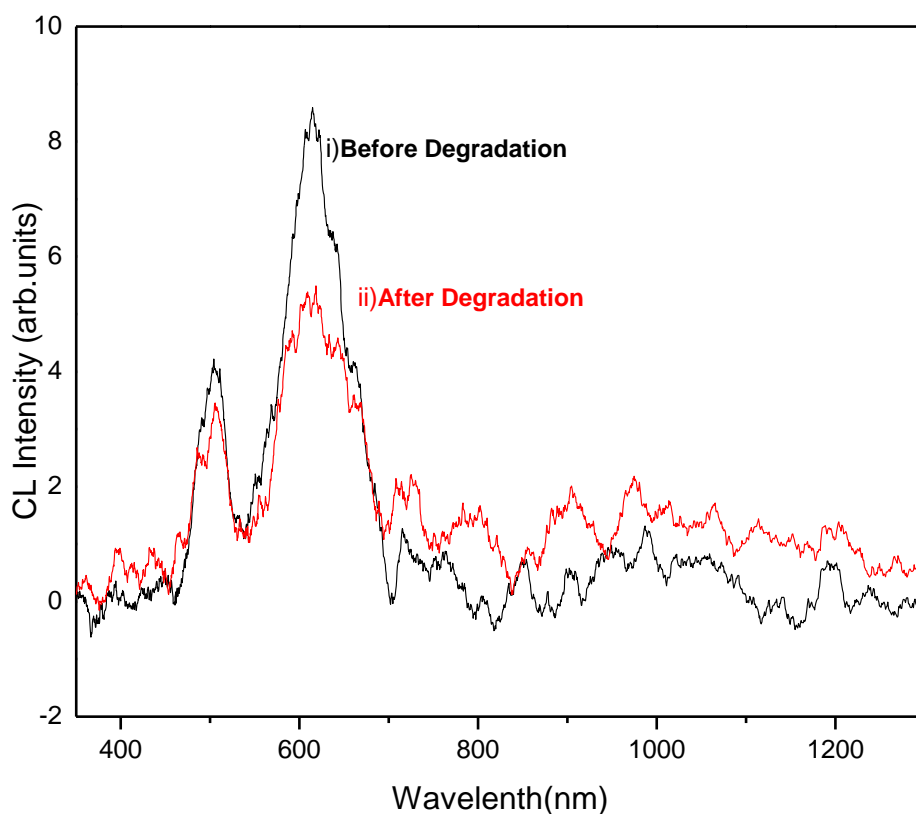

Figure 7.2: CL emission spectra of SiO_2:Pr^{3+} powder phosphor (i) before and (ii) after electron exposure at base a pressure of 1×10^{-9} torr.
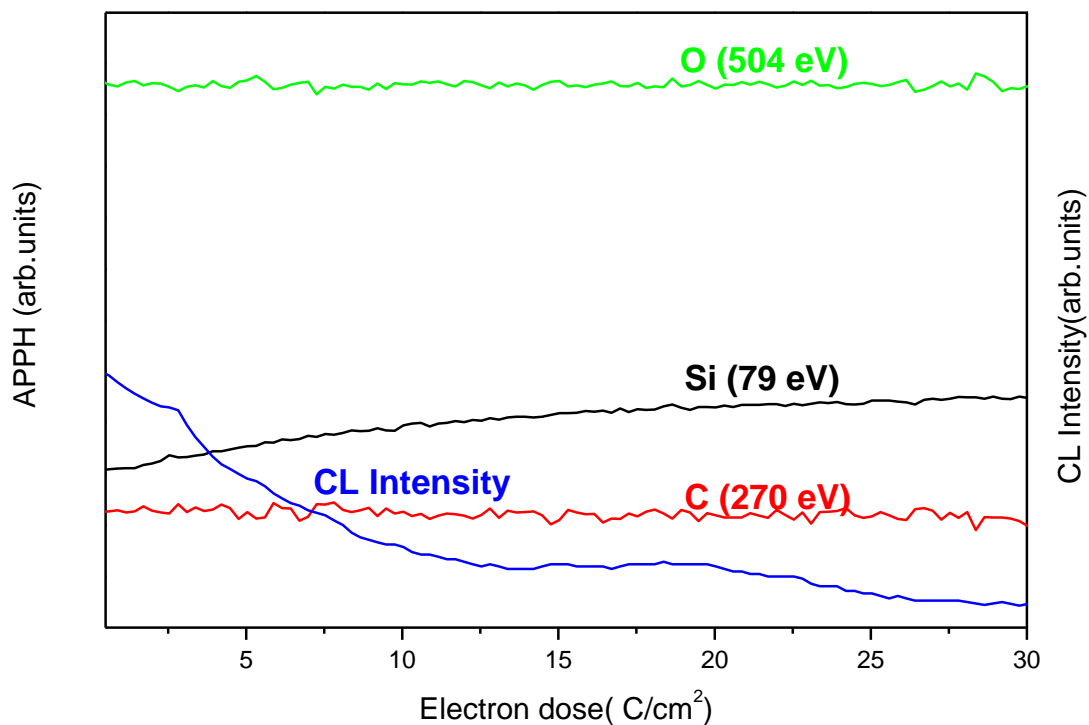
Figure 7.3: Auger peak-to-peak heights of O, Si and C versus 2keV electron dose at 1×10^{-9} torr.

Residual Gas mass Analysis (RGA) was performed in this study to determine the different kind of gas species present in the environment during AES and CL spectroscopy. The molecules of the gas being analyzed are turned into ions by an ionizer through electron impact ionization, i.e., an electron beam is used to strike the gas atoms to ionize them. This ionizing electron beam is generated by an emission filament and extracted by means of an electric field [10].

The RGA spectra, Figure 7.4(a) and (b), shows the difference in residual vacuum gases before and after degradation of $SiO_2:Pr^{3+}$ powder phosphor, with beam on or off at room temperature. There was a dominance of water vapor in both spectra. The H_2O molecule can be cracked by the electron beam into $2H^+$ and O^- thereby creating a high concentration of active atomic species at the surface of a phosphor [11]. These species are known to accelerate the degradation of the CL intensity of phosphors [11,12].
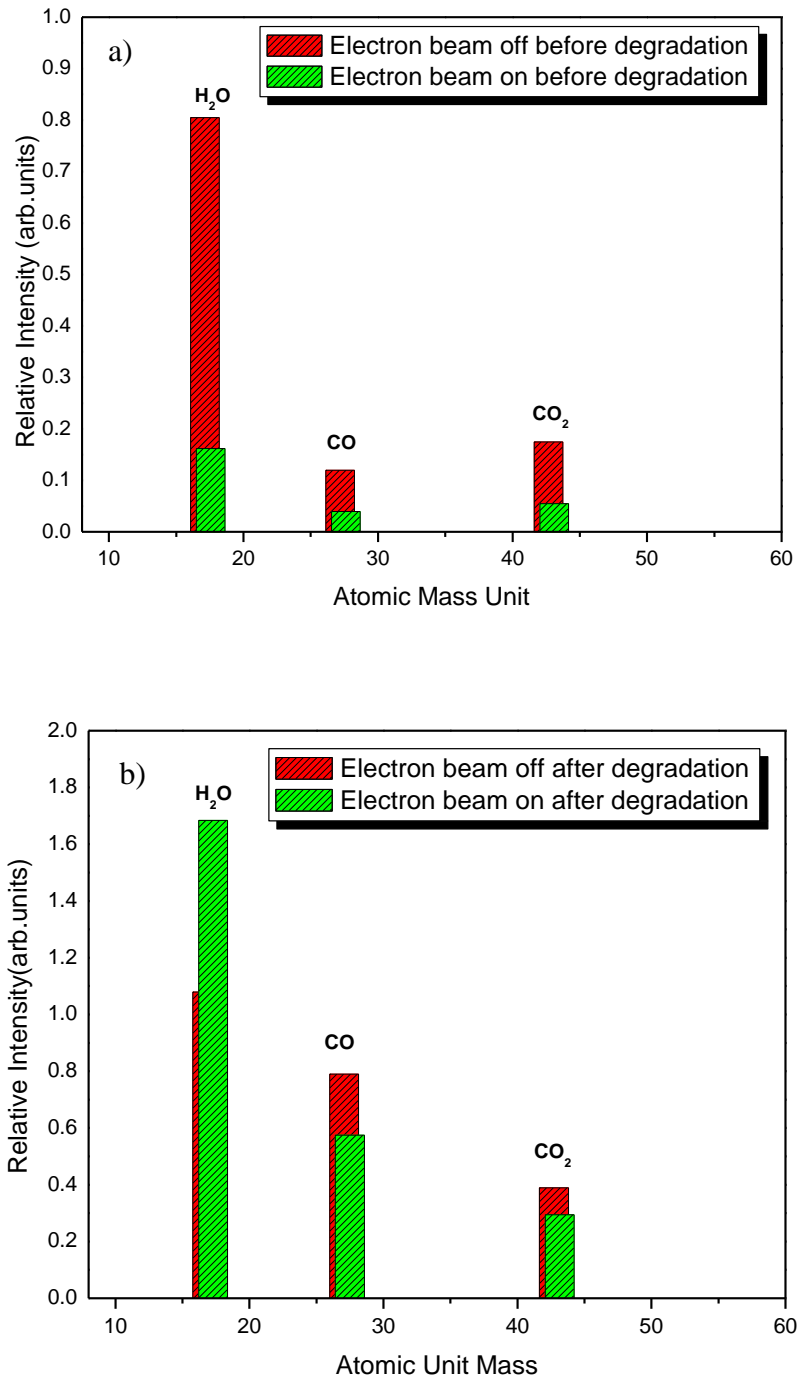
Figure 7.4: RGA results for electron beam on and off (a) before and (b) after degradation.

7.4 Conclusion

The degradation of the $SiO_2:Pr^{3+}$ powder phosphor was investigated by using AES and CL spectroscopy. AES spectra showed a shift of Si element from high energy (normally $\sim$92 eV) to a low energy (79 eV) in the SiO_2 compound and development of new peaks were observed. The Pr^{3+} Auger peaks were detected on the AES spectrum after degradation. RGA analysis showed the dominance of water vapor before and after degradation in a vacuum system which might have contributed to the CL intensity degradation. The decrease in the CL intensity was explained in terms of the ESSCR mechanism.

References

[1] S.H Chen, A.P Greeff and H.C Swart, *Journal of Luminescence* **109** (2004) 93-102

[2] M.S Dhlamini PhD Dissertation, University of the Free state, South Africa, 2008

[3] O.M Ntwaeaborwa, H.C Swart, R.E Kroon, P.H Holloway and J.R Botha, *Journal of Physics and Chemistry of Solids* **67** (2006) 1749-1753

[4] B. Carriere and B. Lang., *Surface Science* **64** (1977) 209

[5] S. Thomas., *Journal of Applied Physics* **45** (1) (1974) 161

[6] B.J Joyce and J.H Neave., *Surface Science* **27** (1971) 499

[7] F. Constantino and R.A.B Devine., *Physical Review Letters* **52**(23) (1984) 2081

[8] B.L Abrams, W.D Roos, P.H Holloway and H.C Swart, *Surface Science* **451** (2000) 174-181

[9] K.T Hillie, S.S Basson and H.C Swart, *Applied Surface Science* **187** (2002) 137-144

[10] E. Coetsee, M.Sc dissertation, University of the Free State, South Africa, 2006

[11] O. M. Ntwaeaborwa, K. T. Hillie, and H. C. Swart, *phys. stat. sol.* **1**(2004) 2366–2371

[12] K.T Hillie and H.C Swart, *Applied Surface Science* **193** (2002) 77-82

Chapter 8

Properties of praseodymium (Pr^{3+}) doped zinc oxide (ZnO)

8.1 Introduction

Zinc oxide (ZnO) is one of the most widely studied wide band-gap ($\sim$3.37 eV at room temperature) semiconductor material at the nano-scale due to its promising applications in, among other things, optoelectronic light emitting diode (LED), laser diodes and sensors [1,2,3]. When excited with the photon energy above the band-gap, high quality ZnO exhibits a richly structured PL at low temperatures [4]. Its luminescent properties are principally related to the electronic and crystalline structure and therefore, strongly influenced by both preparation method and the dopant [5]. This chapter reports on the structure, morphology, chemical composition and the photoluminescence characteristics of praseodymium (Pr^{3+})-doped ZnO prepared by the sol gel method. The influence of the annealing temperature on the crystal structure and the behavior of Pr^{3+} ion concentration are also reported.

8.2 Experimental

The preparation of ZnO and ZnO:Pr^{3+} nanophosphors was discussed in Chapter 4, Section 4.6. The XRD, SEM, TEM and EDS were used to analyze the structure, morphology and chemical composition, respectively. A UV-visible spectrophotometer and a 325nm He-Cd laser were used to determine the luminescence properties of the samples in air at room temperature.

8.3 Results and discussion

Figure 8.1(a) shows the XRD spectra of the ZnO:Pr^{3+} nanophosphor dried at 90°C, which is consistent with the ZnO hexagonal wurtzite structure corresponding to (100), (002), (101), (102), (110), (110), (103), (200), (112) and (201) diffraction peaks [2,3]. These diffraction peaks, are much broader than those in Figure 8.1(b) measured after annealing at 600°C. The narrowing of the diffraction peaks after annealing at 600°C is due to the increase in the particles size. The peak broadening may be due to four factors: microstrains (deformation of the lattice), faulting (extended defects) and crystalline domain size [3]. If we assume that the analyzed Zn O:Pr^{3+} nanophosphors are free of strains and faulting, the peak broadening is only due to the crystalline domain size [2,3]. The average particle size for the samples were estimated to be ~2 nm for ZnO:Pr^{3+} samples dried at 90°C and ~20 nm for the samples annealed at 600°C. The particle sizes were estimated using the Debye-Scherrer equation (Equation 5.1, Chapter 5). The width of the diffraction peak at (102) was used to estimate the particle size.
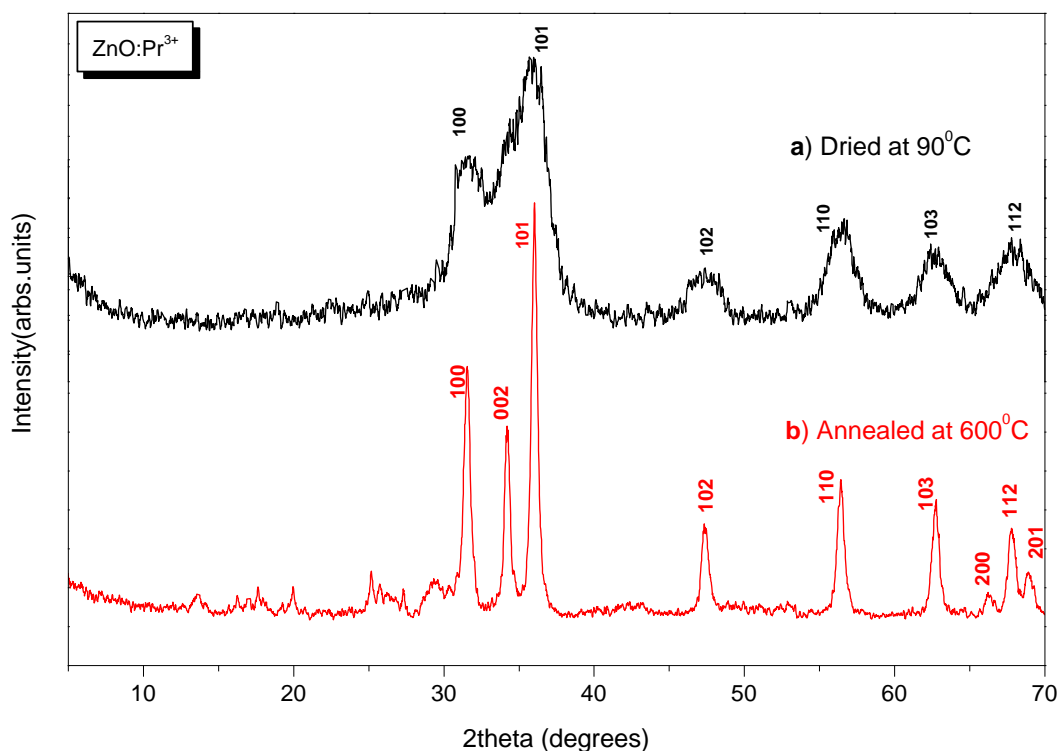

Figure 8.1: XRD Patterns of a) ZnO: Pr^{3+} (dried at 90°C) nanophosphor and b) ZnO: Pr^{3+} obtained by annealing in air at 600°C.

Figure 8.2 shows (a) the SEM and (b) TEM images of ZnO: Pr^{3+} nanophosphor dried at $90^{o}C$. The SEM image clearly shows an agglomeration of spherical nano-sized particles while the TEM image shows some evidence of individual particles on the carbon grids. The estimated average particles size from the TEM image was in the range of 2-10 nm in diameter, consistent with the XRD results. EDS spectrum is shown in Figure 8.3, and all elements except praseodymium were detected. The Pr^{3+} ion was expected to be detected around 5 keV in the energy scale of Figure 8.3. The carbon element detected is probably due to the carbon tape used for the preparation of measurements.
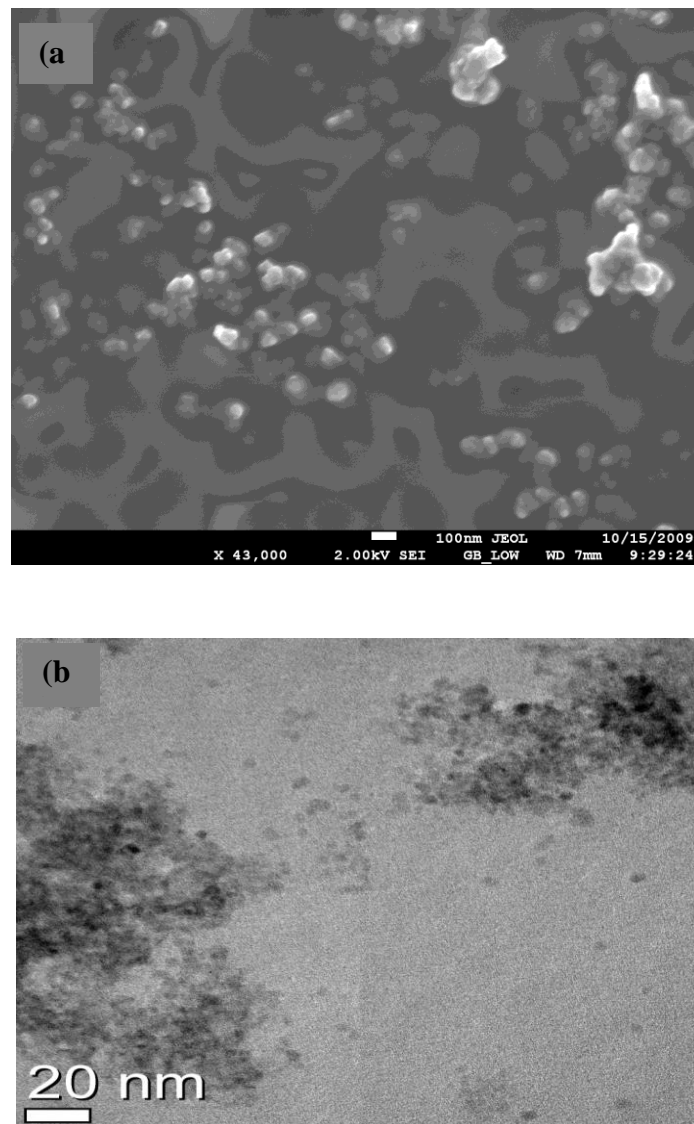

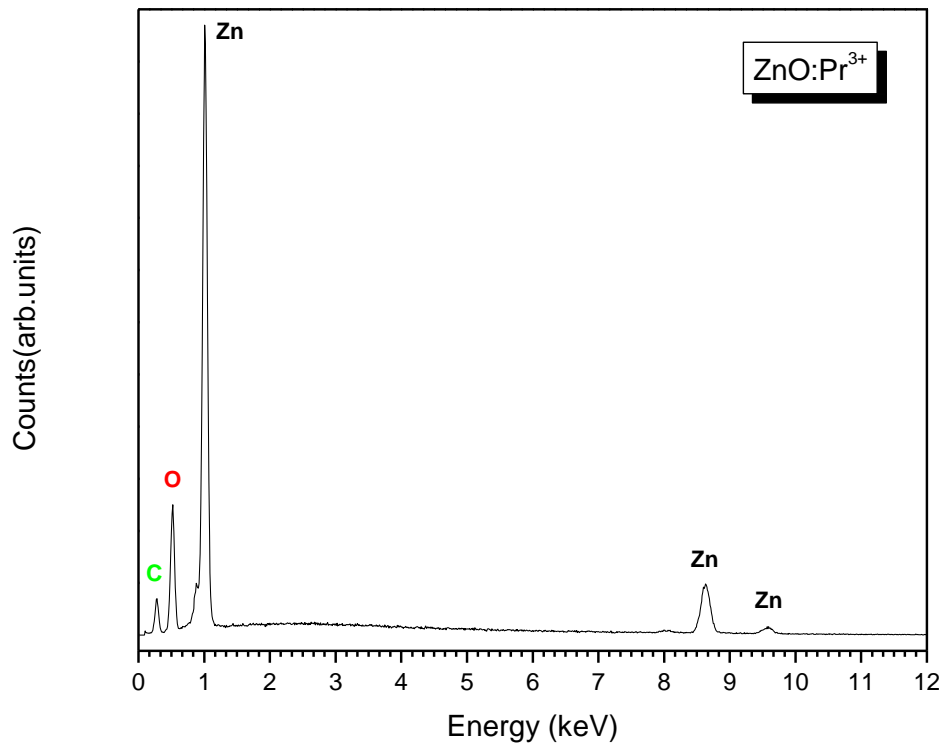**Figure 8.2:** (a) SEM and (b) TEM images of ZnO:Pr^{3+} nanophosphor.

Figure 8.3: EDS spectrum of ZnO:Pr^{3+} nanophosphor (dried 90°C)

The UV-Vis absorption spectra of dried ZnO and ZnO:Pr^{3+} nanophosphors in the 200-800 nm range are shown in Figure 8.4. The optical absorption decreases smoothly from UV to the near-IR for both undoped and Pr-doped sample with absorption band edge observed around 208 nm (5.9 eV). The absorption band is blue shifted compared to the bulk ZnO band reported in the literature (3.37 eV) [1].
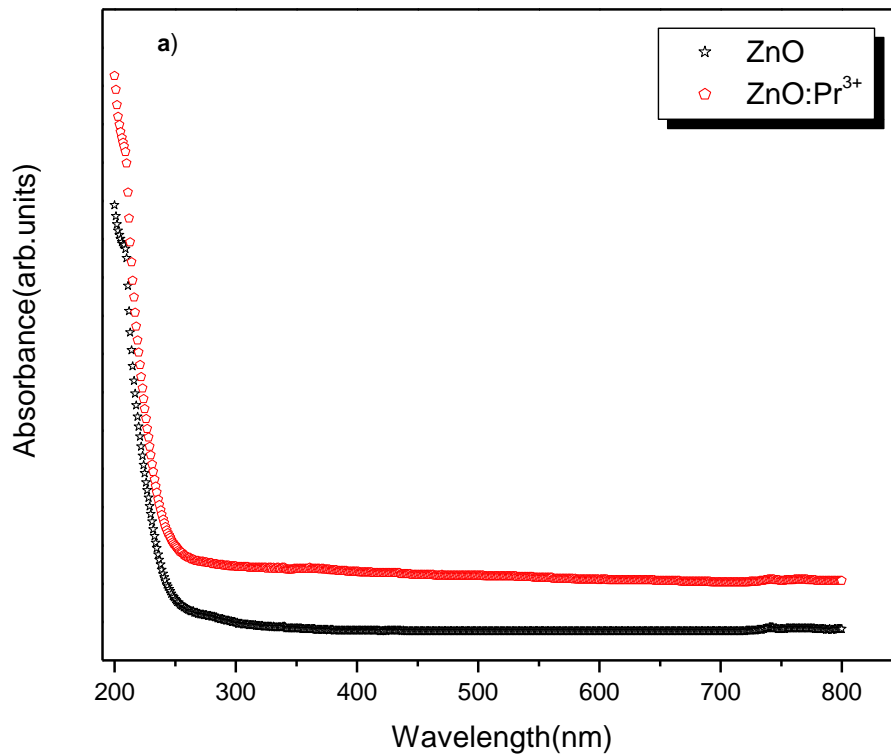
Figure 8.4: Optical absorption spectra of (1) ZnO and (2) ZnO:Pr^{3+} nanophosphors (dried 90°C).

Figure 8.5 (a) shows the PL emission spectrum of pure ZnO powder (dried at 90°C). A broad green emission peak was observed at 567 nm, this broad peak is presumably due to the vacancies or defects that are intrinsic to most synthesis methods [6]. It has also been suggested that the green emission corresponds to the singly ionized oxygen vacancy in ZnO and results from the recombination of a photogenerated hole with the single ionized charge state of the defect [7]. The presence of oxygen vacancies (V$_o$), zinc vacancies (V$_{zn}$) and interstitial zinc (Zn$_i$) have been attributed to correspond to the green emission of ZnO [6]. Also shown in Figure 8.5(a) are two Gaussian profiles fitted to the PL data. The fitting yielded two broad peaks at 557 nm and 616 nm. The fitting parameters are listed in Table 8.1. The existence of two peaks at two different positions can be attributed to emission resulting from recombination at different defect sites [10]. It is therefore most likely that both the zinc and oxygen vacancies contributed to light emission from ZnO. These could not however be differentiated in this study. In Figure 8.5(b), the center of deep level emission band located around 607 nm, which corresponds to the orange luminescence from ZnO:Pr^{3+} (dried at 90°C)

is observed. This band is enhanced when the Pr^{3+} ions are incorporated in ZnO matrix. This orange band is due to the oxygen interstitials, suggesting excess oxygen in the ZnO nanoparticles [7]. There was no significant shift of emission peaks observed when Pr^{3+} ions concentrations was increased, which possibly indicates that this emission may originate from a donor-acceptor transition [9]. Figure 8.6 shows the PL emission of ZnO:Pr^{3+} annealed in air at 600^oC. The spectra show a green emission band at 533 nm and a red emission shoulder at 624 nm. The PL emission suggests that when annealing the ZnO nanophosphors, the particle sizes increases and the peak observed at 624 nm is red shifted from that of 607 nm. The red shifting is attributed to the band tail effects associated with incidental impurities or defects in the material [8]. There was no emission from Pr^{3+} activator ions. The insert in Figure 8.5, shows the 567 nm PL intensity as a function of Pr^{3+} ion concentration. The increase of intensity is observed as the Praseodymium concentration is increased in the ZnO matrix. Table 8.1 shows the Gaussian fitting parameters of PL emission spectra for dried and annealed ZnO nanopowders.

Table 8.1: Fitting parameters of PL emission spectrum ZnO

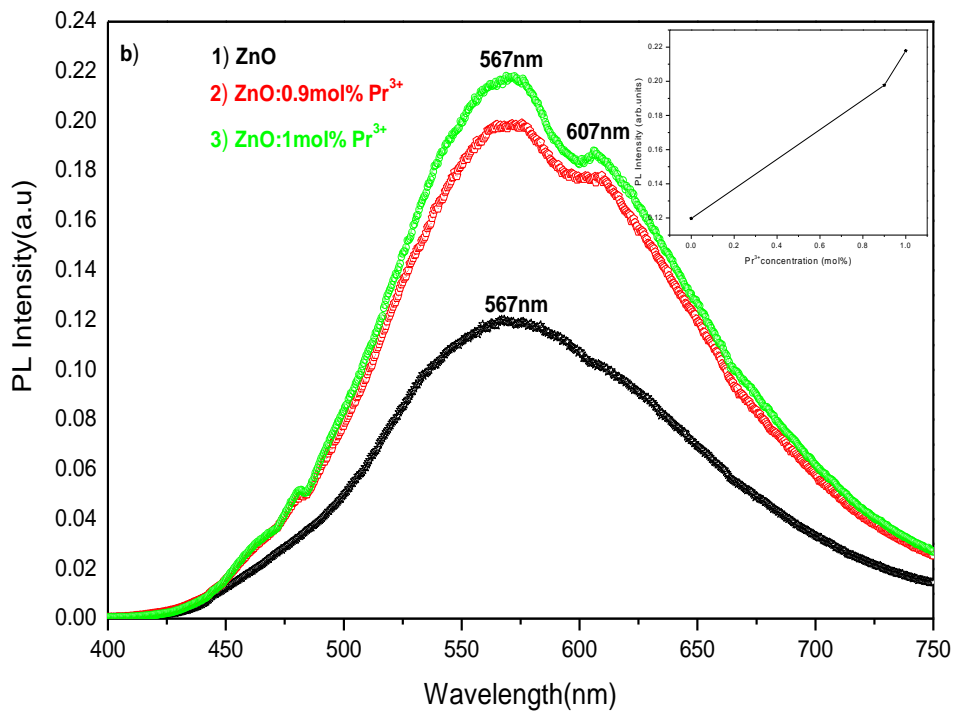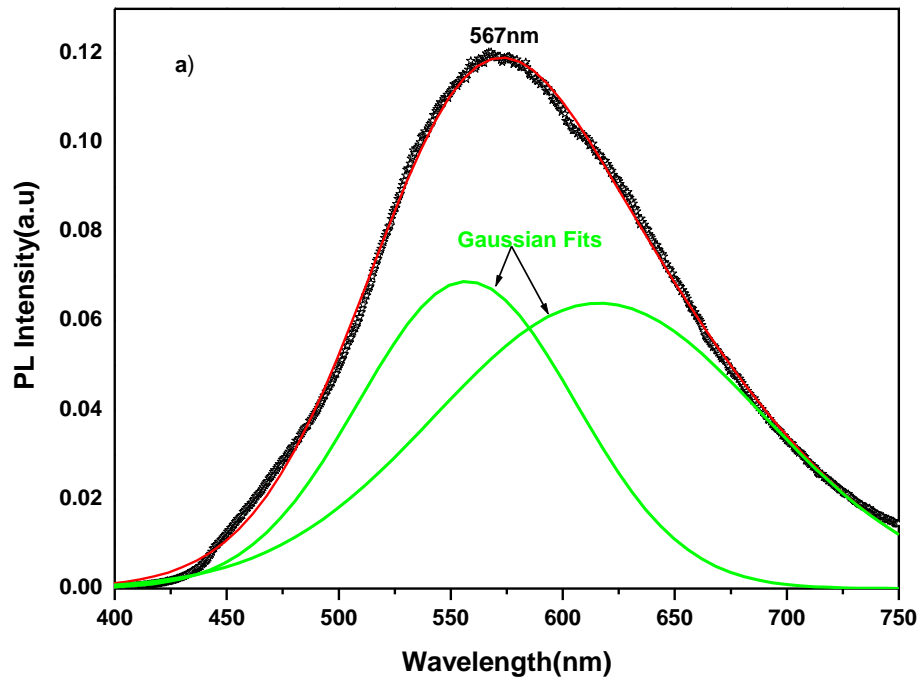| ZnO:Pr^{3+} Dried at 90^oC		
Peak	**1**	**2**
Position (nm)	557	616
Half width (nm)	97.48	146.49
Area (%)	84.81	116.44
Height (a.u)	0.069	0.066
ZnO:Pr^{3+} Annealed at 600^oC		
Position (nm)	531	626
Half width (nm)	94.14	151.9
Area (%)	8.14	6.73
Height (a.u)	0.0069	0.0035

Figure 8.5: (a) Gaussian peak fitting for PL spectra and (b) PL emission spectra of ZnO and ZnO:Pr^{3+} (dried at 90°C) excited at 325 nm.
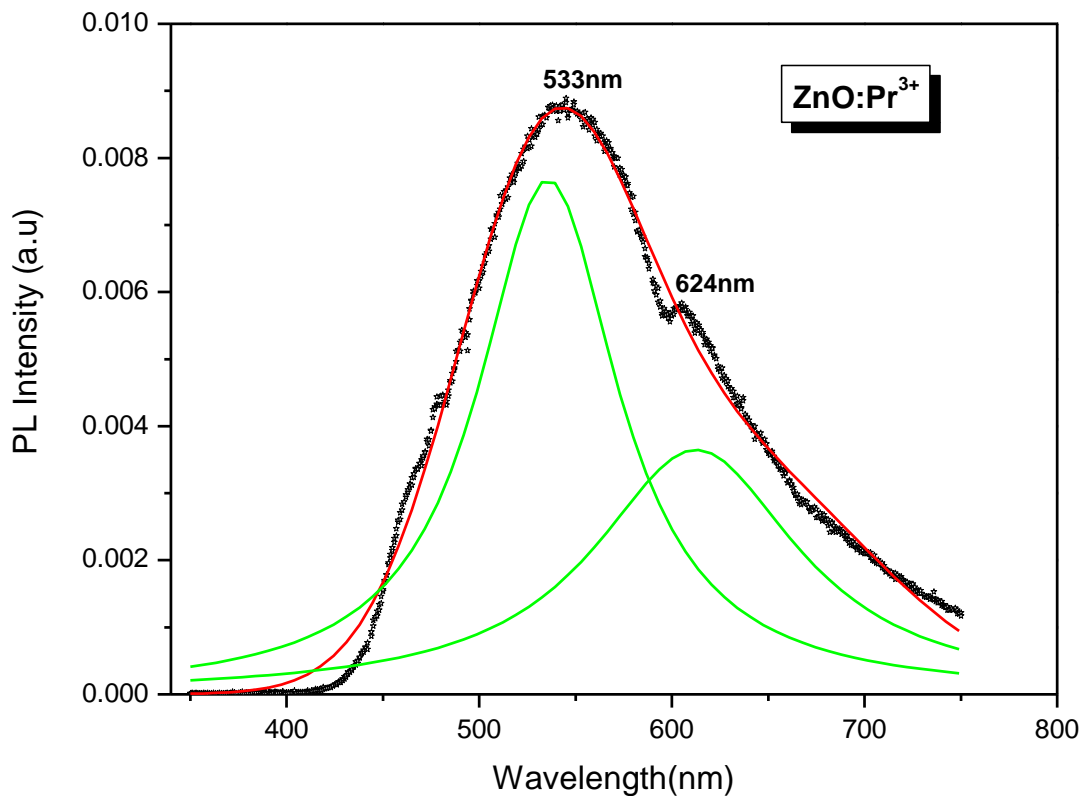
Figure 8.6: Gaussian peak fitting for PL spectra and PL emission spectra of annealed (600°C) ZnO:Pr^{3+} excited at 325 nm.

8.4. Conclusion

Hexagonal wurtzite ZnO nanoparticles were successfully synthesized by the sol-gel method. The broadened XRD peaks became narrow and sharper after annealing the samples at 600°C. The narrowing was attributed to the increase in particle size as a result of annealing. As confirmed by the SEM and TEM images, the particles were spherical and were agglomerated. The absorption band edge was observed around 208 nm and it was blue shifted from band edge of the bulk ZnO due to smaller particle sizes. Dried ZnO and ZnO:Pr^{3+} nanophosphors exhibited the strong visible emission at 567 nm and with a minor emission at 602 nm. Annealed ZnO:Pr^{3+} powder phosphor showed a green emission around 533 nm. The PL emission intensity of 567 nm, increased with an increase of the dopant concentration.

References

[1] D. Bera, L. Qian, S. Sabui, S. Santra and P.H Holloway, *Optical Materials*, **30** (2008) 1233-1239

[2] Ming-Gu Ma, Ying-Jie Zhu, Guo-Feng Cheng, Yue-Hong Huang, *Materials Letters* **62** (2008) 507–510

[3] J. Jang, L. Jang, X. Liu, Y. Zhang, Y. Wang, H. Fan, D. Wang and J. Lang, *Journal of Alloys and Compounds* **436** (2008) 92-95

[4] T. Montero, A.J Neves, M.C Carmo, M.J Soares, M. Peres, E. Alves, E. Rita and U. Wahl, *Superlattices and Microstructural* **39** (2006) 202-210

[5] Y.X. Li, Y.Y. Li, Y.L. Wu and W.L. Sun, *Journal of Luminescence* **126** (2007) 177-181

[6] J.B Wang, D, Shuang, X.L Zhong and H.L Yan, *Materials Science in Semiconductor Processing* **10** (2007) 97-102

[7] F. Li, Y. Jiang, L. Hu, L. Liu, Z. Li and X. Huang, *Journal of Alloys and Compounds* **474** (2009) 531-535

[8] H. Z Wu, D.J Qiu, Y.J Cai, X.L Xu and N.B Chen, *Journal of Crystal Growth* **245** (2002) 51

[9] A.B Djurisic, Y.H Leung, K.H Tam, Y.F Hsu, L.Ding, W.K Ge. Y.C Zhong, K.S Wong, W.K Chan, H.L Tam, K.W Cheah, W.M Kwok and D.L Phillips, *Nanotechnology* **18** (2007) 095702

[10] E. Coetsee, J.J Terblans, O.M Ntwaeaborwa and H.C Swart, *Physica B* **404** (2009) 4426-4430

Chapter 9

Properties of praseodymium (Pr^{3+}) doped zinc sulphide (ZnS)

9.1 Introduction

Zinc sulphide (ZnS), a semiconductor with band-gap energy of 3.66 eV (bulk), has received a lot of attention due to its excellent properties, such as large band-gap energy, direct recombination and resistance to high electric field [1]. The incorporation of activator ions creates novel luminescent centers in the bandgap of ZnS nanocrystals [2]. This chapter reports on the structure, morphology, chemical composition and the photoluminescence characteristics of praseodymium-doped ZnS prepared by precipitation method. The influence of the annealing temperature on the crystal structure and the behavior of the activator ion concentration are also reported.

9.2 Experimental

The preparation of ZnS and ZnS: Pr^{3+} nanophosphors was discussed in Chapter 4, Section 4.5. The XRD, SEM, TEM and EDS were used to analyze the structure, morphology and chemical composition, respectively and UV-visible spectrophotometer with a 325 nm He-Cd laser were used to determine the luminescence properties of the samples in air at room temperature.

9.3 Results and discussion

Shown in Figure 9.1(a) are the XRD peaks from dried (90°C) ZnS: Pr^{3+} nanoparticles that correspond to the lattice planes (111), (220) and (311), characteristic diffractions of a cubic phase [3]. The peak broadening at lower angle is more meaningful for the calculation of particle sizes, therefore broadening of the diffraction peak (111) was used to estimate the average particle size of the samples using the Debye-Scherrer equation (Equation 5.1,Chapter 5) [4]. The particles were estimated to be ~2 nm. ZnS: Pr^{3+} was annealed in air at 600°C, Figure 9.1(b), the transformation of cubic phase ZnS to hexagonal ZnO and a very weak peak associated with cubic ZnS were observed. The results indicate that most of the zinc sulphide was transformed to ZnO. The diffraction peaks of Figure 9.1(b) are narrow and shaper than those of Figure 9.1(a) suggesting that there was an increase in particle sizes due to annealing. The average particle size of the annealed sample was calculated to be ~17-20 nm in diameter.

TEM image of ZnS: Pr^{3+} nanoparticles suspended in ethanol and then allowed to dry on carbon coated copper grids are shown in Figure 9.2. (b) The image shows the cluster of agglomerated particles in the nano-scale sizes. SEM image also shows an agglomeration of nanoparticle, figure 9.2(a). Figure 9.3 shows the EDS spectrum, major elements were detected except for the dopant element and this may be due to its low concentration in the ZnS matrix.
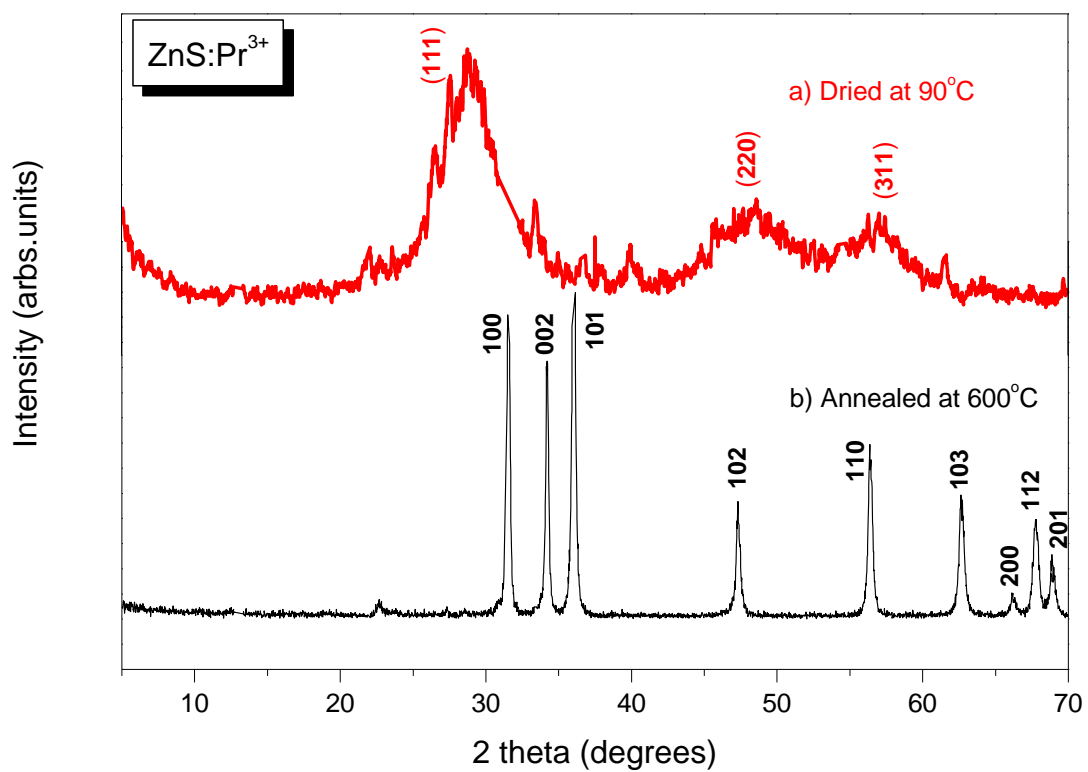
Figure 9.1: XRD Patterns of   a) ZnS: Pr^{3+} (dried at 90°C) nanophosphor and b) ZnO: Pr^{3+} obtained by annealing ZnS at T$_a$=600°C.
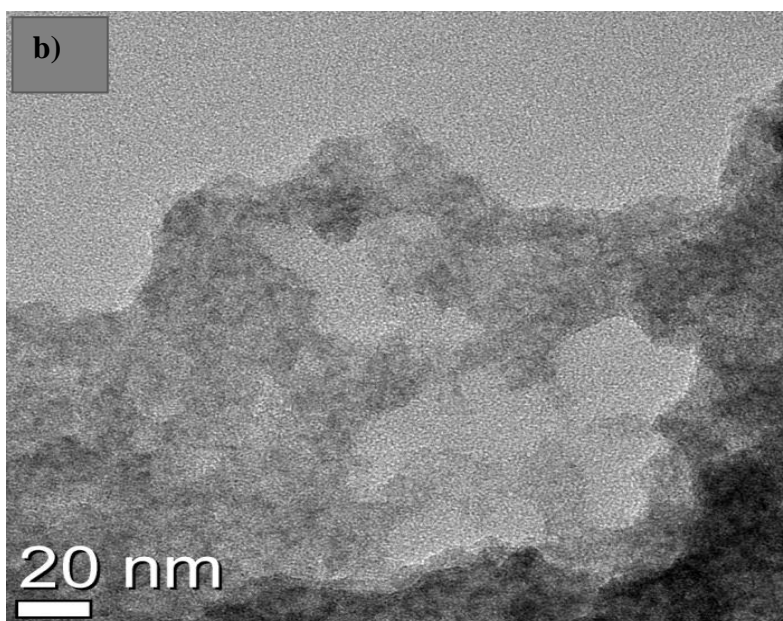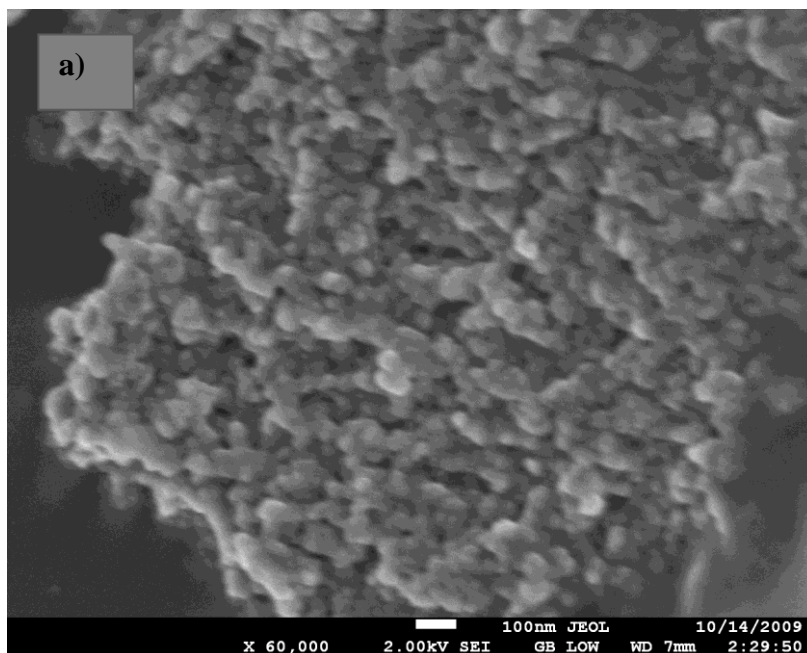
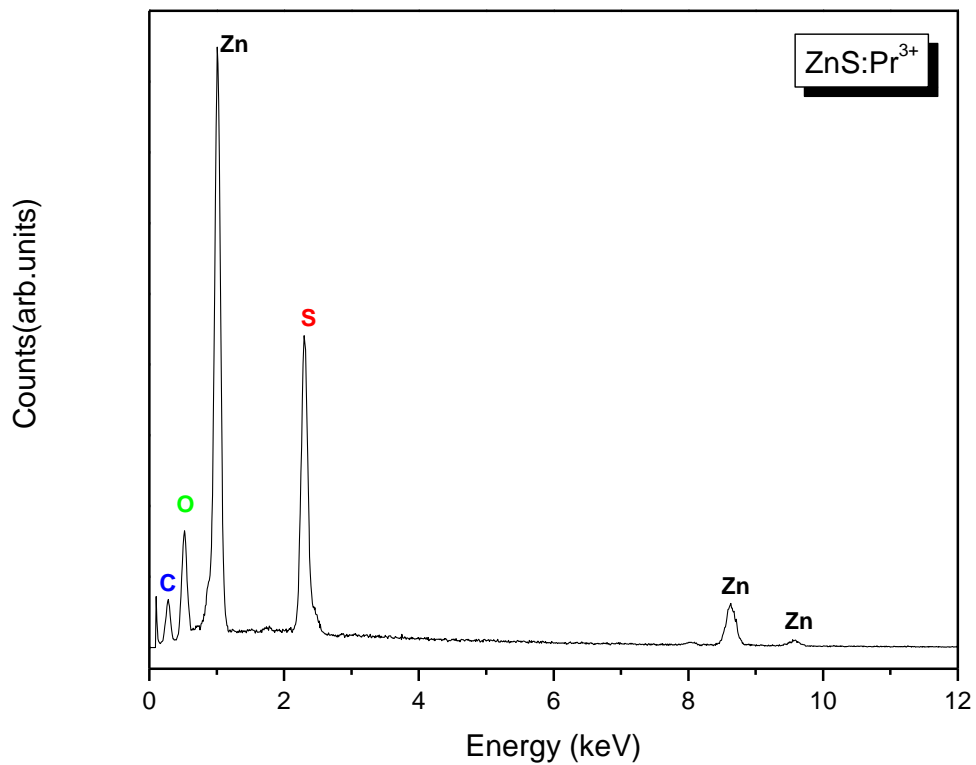**Figure 9.2:** (a) SEM and (b) TEM image of ZnS nanophosphor (dried at 90°C).

Figure 9.3: EDS spectrum of ZnS:Pr^{3+} nanophosphor (dried at 90°C).

Figure 9.4 shows the UV-Vis absorption spectra of ZnS and ZnS: Pr^{3+} nanoparticles. The spectra show a band at 307 nm (4.05 eV) corresponding to the band-gap absorption of ZnS nanoparticles, and it is blue shifted from the band-gap absorption of bulk ZnS at 340 nm (3.66 eV) [5]. The band-gap of ZnS nanoparticles is enlarged probably due to quantum confinement effects [5,6,7].
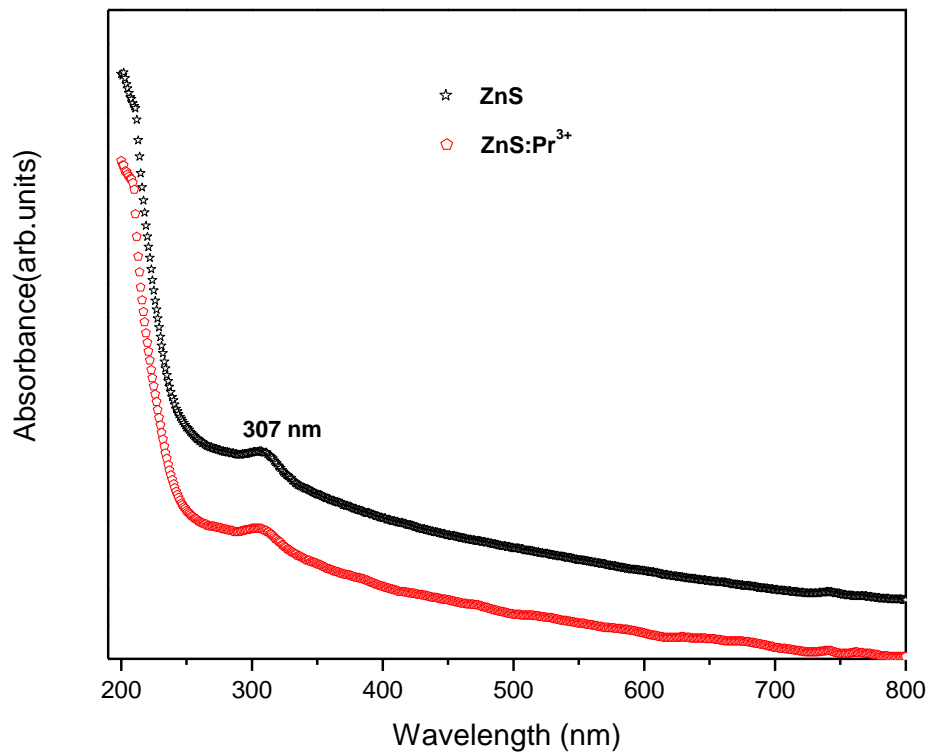
Figure 9.4: Optical absorption spectra of ZnS and ZnS:Pr^{3+} nanophosphors (dried at 90°C).

Figure 9.5 (a) shows the PL emission spectra of ZnS and ZnS: Pr^{3+} (dried at 90°C) nanophosphor. Blue emission band centered at 445 nm is observed, which arises from excitonic recombination in ZnS [5]. As the concentration of Pr^{3+} ion was increased the PL intensity also increased. The emission wavelength also shifted to the 451 nm as observed in Figure 9.5 (a). The shifting may be due to incorporation of Pr^{3+}. Figure 9.5(b) shows the well-known green emission of ZnO nanophosphor from the ZnS powders annealed at 600°C. This result confirms that ZnS was transformed to ZnO as observed from the XRD data. Due to structure conversion, the vacancies and defects increase which cause the peak broadening [1]. The insert in Figure 9.5(a), shows the PL emission intensity behavior as a function of Pr^{3+} concentration in ZnS matrix. It was observed that the PL intensity increased with Pr^{3+} concentration and reached the maximum at 0.9 mol% doping level.
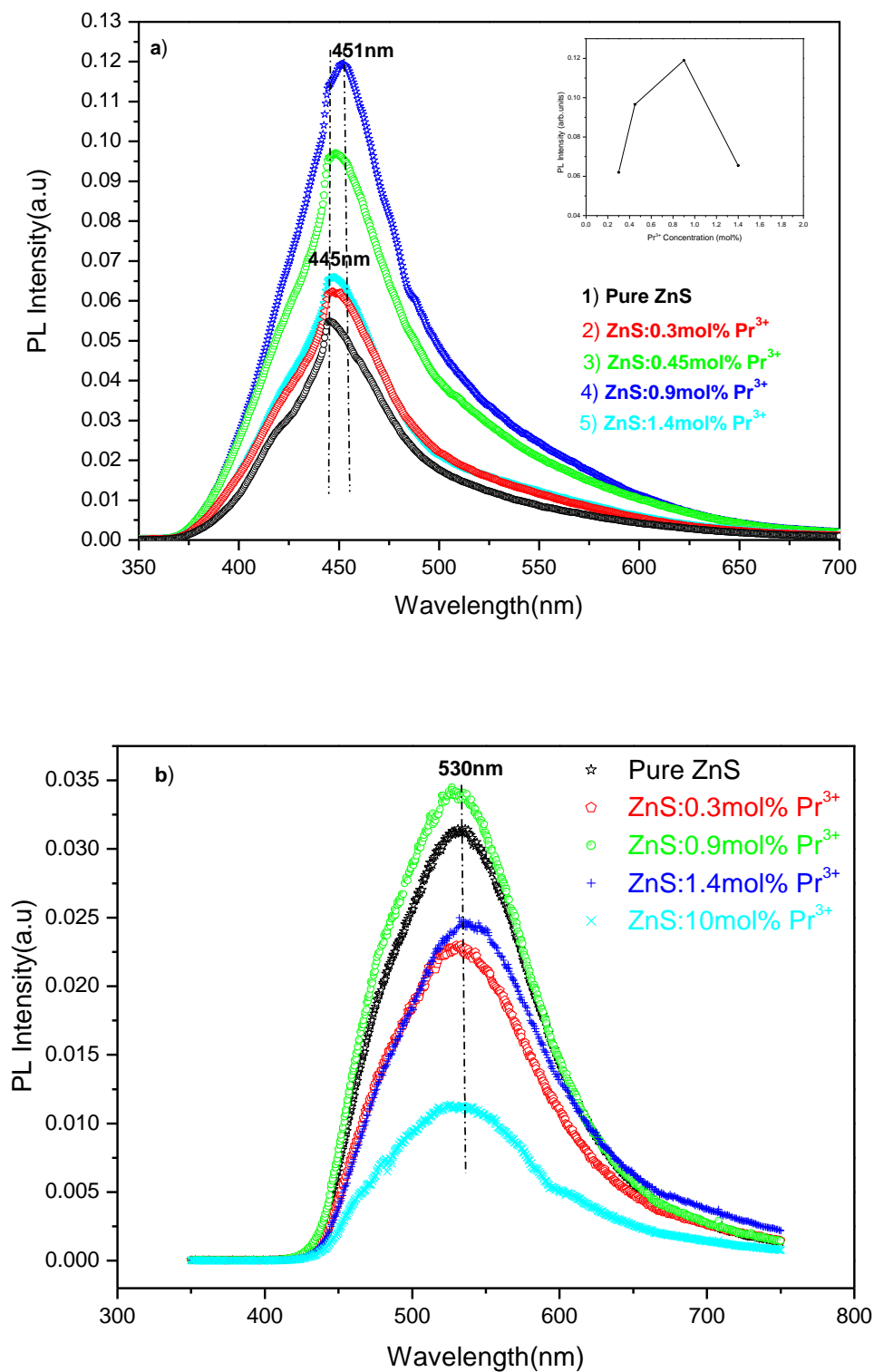
Figure 9.5: PL emission spectra of (a) ZnS and ZnS:Pr^{3+} dried at 90°C (b) ZnO emission obtained by annealing ZnS at 600°C, excited at 325 nm.

9.4. Conclusion

Pr-doped ZnS nanophosphors were synthesized successfully by the sol-gel method. XRD confirmed the ZnS cubic phase and average particle sizes of ~2-4 nm in diameter. The transformation of a cubic ZnS phase to hexagonal phase of ZnO was observed after annealing at 600^0C. PL emission showed a blue band emission as a result of excitonic recombination in ZnS. Annealed ZnS gives emission at 530 nm which was attributed to defects in ZnO. This result showed that ZnS was transformed to ZnO by annealing at 600^oC. The PL intensity increased with an increase of Pr^{3+} concentration up to 0.9mol%, then concentration quenching was observed at higher doping levels.

References

[1] S.Y Chu and H.Y Lu, *Journal of Crystal Growth* **265** (2004) 476-481

[2] M. Lu, P. Yang, D. Xu, D. Yuan and C. Song, *Journal of Physics and Chemistry of Solids* **64** (2003) 155-158

[3] Hua-Feng Shao, Xue-Feng Qian and Zi-Kang Zhu, *Journal of Solid State Chemistry* **178** (2005) 3522-3528

[4] K.S Rathore, D Patidar, Y. Janu, N.S Saxena, K. Sharma and T.P Sharma, *Chalcogenide Letters* **5** (2008) 105-110

[5] M.M. Biggs, O.M.Ntwaeaborwa,J.J.Terblans and H.C.Swart., *Physica B* **404**(2009) 4470-4475

[6] B. Bhattacharjee, D. Ganguli, S. Chaudhuri and A.K Pal, *Thin solid films* **422**(2002) 98-103

[7] O.M Ntwaeaborwa, R.E Kroon, V. Kumar, T. Dubroca, J.P Ahn, J.K Park and H.C Swart, *Journal of Physics and Chemistry of Solids* **70** (2009) 1438-1442

[8] V. Kumar, H.C Swart, O.M Ntwaeaborwa, R. Kumar, S.P Lochab, V. Mashra and N. Singh, *Optical Materials* (2009), doi:10.1016/j.optmat.2009.06.018

Chapter 10

Summary and Conclusion

Luminescent properties, structure and particle morphology of $SiO_2:Pr^{3+}$, $ZrO_2:Pr^{3+}$, $ZnO:Pr^{3+}$ and $ZnS:Pr^{3+}$ powder phosphors with different concentrations of Pr^{3+} were investigated. Photoluminescence and cathodoluminescence data were collected when the phosphors were excited by the 325 nm He-Cd laser or monochromatic xenon lamp and 2 keV electrons respectively. These phosphors were successfully prepared by the sol-gel method. $SiO_2:Pr^{3+}$ powder phosphor showed an amorphous structure even after annealing at $600^{o}C$. Equally, there were no diffraction peaks associated with Pr^{3+} ions suggesting that the ions were well dispersed in the silica matrix and also because of the fact that their concentration was relatively low. Photoluminescence from $SiO_2:Pr^{3+}$ was associated with structural defects in SiO_2. There were no photoluminescence peaks from Pr^{3+}. The defect emission was shown to decrease when the concentration of Pr^{3+} was increased from $0.6 - 1$ mol%. The decrease was attributed to possible formation of nonradiative centers as a result of incorporation of Pr^{3+}. Cathodoluminescence maxima emission was detected at ~614 nm and was associated with radiative transitions in Pr^{3+}. This CL intensity of this emission was shown to degrade as a result of prolonged exposure of the phosphor to 2 keV electrons. The degradation was attributed to the formation of non-luminescent layer formed according to the electron stimulated surface chemical.

$ZrO_2:Pr^{3+}$ powder phosphor exhibited an amorphous structure at lower annealing temperature ($280^{o}C$) and the temperature was increased to $600^{o}C$ (8 ± 0.1 nm), after which a tetragonal phase was observed with broadened diffraction peaks suggesting that the particles were within the nano domain. Photoluminescence from the pure and Pr^{3+}-doped ZrO_2 powders annealed at $280^{o}C$ consisted of two emission peaks at 459 nm and 554 nm. These emissions were attributed to structural defects in ZrO_2. No emission was detected from the powders annealed at $600^{o}C$.

ZnS:Pr^{3+} dried at 90°C showed cubic phase structure and the nanoparticles were estimated to be ~2 ±0.2 nm. Upon annealing of ZnS:Pr^{3+} nanophosphor, the transformation from the cubic phase to the hexagonal phase was observed suggesting ZnO was formed as a result of annealing. The diffraction peaks of the annealed ZnS of the cubic phase were sharper suggesting that there was an increase of particle sizes and the size was estimated to be ~17-20 ±0.2 nm. Photoluminescence from ZnS:Pr^{3+} was attributed to excitonic recombination in ZnS bandgap. No cathodoluminescence was detected from this material due to charging.

ZnO:Pr^{3+} dried at 90°C exhibited an hexagonal wurtzite structure and particle sizes were estimated to be ~2 ±0.2 nm, after annealing at 600°C the diffraction peaks also became sharper and particle size was increased to ~20±0.2 nm. Photoluminescence from ZnO:Pr^{3+} was attributed to defects in ZnO. Also, no cathodoluminescence was detected from this material due to charging. As confirmed by the SEM and TEM, all the powders consisted of an agglomeration of spherically-irregularly shaped particles. Photoluminescence in the near-infrared was not observed for all the powder samples and cathodoluminescence degradation was performed only on SiO$_2$:Pr^{3+}. ZrO$_2$:Pr^{3+}, ZnO:Pr^{3+} and ZnS:Pr^{3+} did not emit light under electron bombardment.

Future Work

Among various rare-earth luminescent centers, Pr^{3+} is a unique optical activator which provides the possibility of simultaneous blue, green and red emissions depending on the host matrice in which it is incorporated. By choosing an appropriate host matrix there are chances of producing white phosphor for white LEDs. This can therefore be investigated in future studies. Temperature effects, as experimental results can reveal that the luminescence and structure can be affected by annealing temperature is also an important factor that needs to be further investigated. Furthermore it will be interesting to investigate Pr-doped host matrices prepared by other methods such as combustion method. It is also important to investigate the different excitation sources to excite Pr^{3+} ion and compare its luminescence.